Limits of High Harmonic Generation Conversion Efficiency

by

Vasileios-Marios Gkortsas

Diploma, Electrical and Computer Engineering,
National Technical University of Athens, Greece (2006)

S.M., Applied Physics, Harvard University (2008)

Submitted to the Department of Electrical Engineering and Computer Science
in partial fulfillment of the requirements for the degree of

Doctor of Philosophy in Electrical Engineering and Computer Science

at the

MASSACHUSETTS INSTITUTE OF TECHNOLOGY

September 2013

Author .....
Department of Electrical Engineering and Computer Science
July 9, 2013

Certified by ...
Franz X. Kärtner
Adjunct Professor of Electrical Engineering
Thesis Supervisor

Accepted by .....
Leslie A. Kolodziejski
Chair, Department Committee on Graduate Students

Limits of High Harmonic Generation Conversion Efficiency

by

Vasileios-Marios Gkortsas

Submitted to the Department of Electrical Engineering and Computer Science
on July 9, 2013, in partial fulfillment of the
requirements for the degree of
Doctor of Philosophy in Electrical Engineering and Computer Science

Abstract

High Harmonic Generation (HHG) is a fascinating phenomenon from both fundamental and technological point of view. It enables the generation of attosecond pulses and can have applications in EUV lithography and bio-microscopy. HHG can be described by the Three Step Model (TSM), due to the three stages of the process: ionization, propagation and recombination.

However, HHG suffers from low efficiencies and a study, which shows the efficiency scaling with laser and material parameters is essential. For a long time experimentalists were using only 800 nm driver pulses from Ti:sapphire lasers. With the advent of new light sources like optical parametric amplifiers, different driving wavelengths became available and thus the scaling of the single atom response versus drive wavelength has attracted a lot of attention. A detailed analysis shows that the efficiency scales with ω_0^5 at the cutoff and ω_0^6 at the plateau region for a fixed EUV frequency, where ω_0 is the carrier frequency of the driver pulse.

To understand the limitations of such a light source, we have developed a semi-analytic model for the computation of the conversion efficiency into a single harmonic for the plateau and cutoff regions. This model is one-dimensional, uses the TSM for the calculation of the single atom response and takes laser, material parameters and macroscopic effects into account. Closed form expressions for the plateau and cutoff regions are derived and used to calculate efficiencies for 400 and 800 nm driver pulses. The results are compared with experimental ones showing very good agreement.

In order to investigate long-wavelength driven HHG efficiency, the 1-D model is extended to three dimensions taking into account spatiotemporal propagation effects, such as plasma defocusing and losses due to electron-neutral inverse bremsstrahlung. These phenomena change the phase matching along propagation, resulting in non-coherent harmonic generation and consequently poor efficiencies. We further study ways to mitigate the effect of plasma defocusing like the use of Supergaussian pulses and the use of Gaussian pulses with larger beam waists.

The work presented can help us develop tools for an optimization study of HHG efficiency, in order to make useful EUV sources.

Thesis Supervisor: Franz X. Kärtner
Title: Adjunct Professor of Electrical Engineering

In the memory of my mother and aunt Angeliki

Acknowledgements

First of all, I would like to thank my research advisor, Professor Franz X. Kärtner, who gave me the opportunity, while being S.M. student at Harvard University, to perform research at the Massachusetts Institute of Technology and then enrolling as a full time student to the Ph.D. program of the Department of Electrical Engineering and Computer Science at MIT. I feel very privileged to have him as my advisor for my Ph.D. studies. Franz has been a great source of help, advice, and kind encouragement. Perhaps equally important is his unlimited positive energy and enthusiasm, which motivates people around him. When I was pessimistic about the research results, Franz was always encouraging and guiding me.

I would also like to thank the members of my thesis committee, Professor Erich Ippen and Professor Mike Watts, who provided me with valuable comments and advice. Professor Ippen was always available to advise me regarding my next professional steps and also provided me with detailed comments on my thesis. Professor Federico Capasso, my S.M. advisor at Harvard University, has also been a great of source of help and motivation.

I am grateful to my colleagues at the Optics and Quantum Electronics group. Ariel Gordon introduced me to the concepts of High Harmonic Generation and Quantum Cascade Lasers and was willing and available to help me even when he left the group. We had meetings over Skype and he was happy to guide me in spite of the time difference between US and Israel. A large percent of the things I know, I learned them from him. In the last two years I collaborated closely with Jeff Moses. Jeff is a great scientist, but an even greater person. He helped to clarify difficult concepts and tackle a challenging project. Most importantly he was next to me as a real friend when I had to deal with a very important family issue. I am thankful to Edilson L. Falcão-Filho for the overnight discussions (some times till 5 am) and the very good work we did. I would also like to thank Chien-Jen Lai for the discussions and his help. I was happy to work with Kyung-Han Hong, whose experience in HHG was valuable.

I would like to separately mention my friends and officemates Anatoly Khilo and Siddharth Bhardwaj. We shared the same office for more than six years and starting from a

typical professional collaboration, we developed a strong friendship. We had many interesting conversations about research as well as things way beyond it. I will never forget that when one time Franz wanted to move Siddharth and myself to another office, Siddharth and Anatoly requested that the three of us stay at the same office. The amazing thing was that I was in Greece for vacations and they took the initiative to request that we stay at the same office without asking me. They knew that I would agree. This event showed how close we were. I will also never forget Siddharth's help in Hamburg, Germany when I had to move out from my apartment at 11 pm and asked him for his help. I can give many more examples and even write a whole book for my time with Siddharth and Anatoly.

I would like to thank my friend since primary school, Themos Arkoumanis who was always close to me and interested in my progress although we were thousands miles apart. I want to thank my fiends Nikos Kontopoulos for the countless nights and few days we spent, while trying to rule Boston's nightlife, Evangelos Sfakianakis for the infinite discussions about politics, education and gossip for the Greek community, Dimos Mantopoulos for the countless discussions and for being a loyal friend, Apostolos Fertis who welcomed me to the Greek community at MIT and was always helpful and supportive, Eva Ieronymaki for being supportive and a wise source of advice, Spyros Zoumpoulis who apart from a good friend was always available for help when I was exploring research topics outside of my comfort zone, and Sasha Stolyarov who apart from the many funny moments we had, he was a reliable source of advice when I was looking for research group. I would like to thank my friend Siamak Kia whom I know for only one year, but I feel that we are friends since kids and his wife Samira Ghanadyan, who helped me find my new apartment. I am also thankful to Lida Kim Bell who attended my PhD thesis with her 1-year old son, Michalis Markakis, Yola Katsargyri, Dimitris Chatzigeorgiou, Stefania Radopoulou, Andriani Ferti, Kleio Palaska and Angeliki Asimaki. Also special thanks to my friends from my undergraduate studies Ioannis Doudalis and Pavlos Ginatzis that have not seen them for years, but we chat over Facebook a lot.

I am grateful to Keiko Hiromi. I cannot express how thankful I am to her with one

paragraph. She was always encouraging and caring. Without her it would be impossible to complete my Ph.D. studies. I will never forget that when I was looking for alternative paths for my future career she was always telling me how cool it is to do science and engineering and was encouraging to continue with my research. A huge part of this accomplishment belongs to her.

My family was always next to me. I want to thank my father Georgios and my brother Stathis for all their support since I was kid. My father taught me to be a diligent and organized student and he transferred to me the love for science and academia. Most importantly he taught me moral values and how to be a useful person for the society. My brother is my best friend and the person I trust the most. We are thousands miles apart since 2006, but simultaneously we are so close. It is hard to express in words my gratitude. They invested in me so much and I hope I am a good son and brother. I also want to mention my uncle Nikos and my cousins Lila and Maria and thank them for their love.

I want to finish this section by mentioning two very important people who are not with us any more, since the summer of 2012. My mother Niki and my aunt Angeliki. Unfortunately they are not with us to experience the completion of my studies, but I am sure they are happy together and proud to see that the goal was fulfilled. Although my mother did not want me to leave Greece for United States, she was supportive of my decision and very proud for me. I hope that at the place they are now they can see and share my happiness. I think of them every single day and I would like to devote this thesis in their memory.

Contents

Chapter 1

Introduction

The electromagnetic spectrum ranges between radio frequencies (3 kHz to 300 GHz) and Gamma radiation (frequencies $> 10^{19}$ Hz) and covers wavelengths between thousands of kilometers down to a fraction of the size of the atom (Figure 1-1). Most of the part of the electromagnetic spectrum is used for scientific applications. In this thesis we cover two regions of the spectrum, the mid- to far- infrared (3.5-20 μm) through the Quantum Cascade Laser project and the Extreme UltraViolet to soft X-ray range (120 nm up to 0.8 nm or 10 eV-1.5 keV) through the High Harmonic Generation project. The goal of the Quantum Cascade Laser project is to generate isolated short pulses via active mode locking and to study the impact of spatial hole burning on pulse shape and stability. The goal of the High Harmonic Generation project is to study the limits of the efficiency and do a theoretical efficiency optimization study. The High Harmonic Generation project covers 80% of the thesis and the Quantum Cascade Laser project, described in Appendix A, 20%.

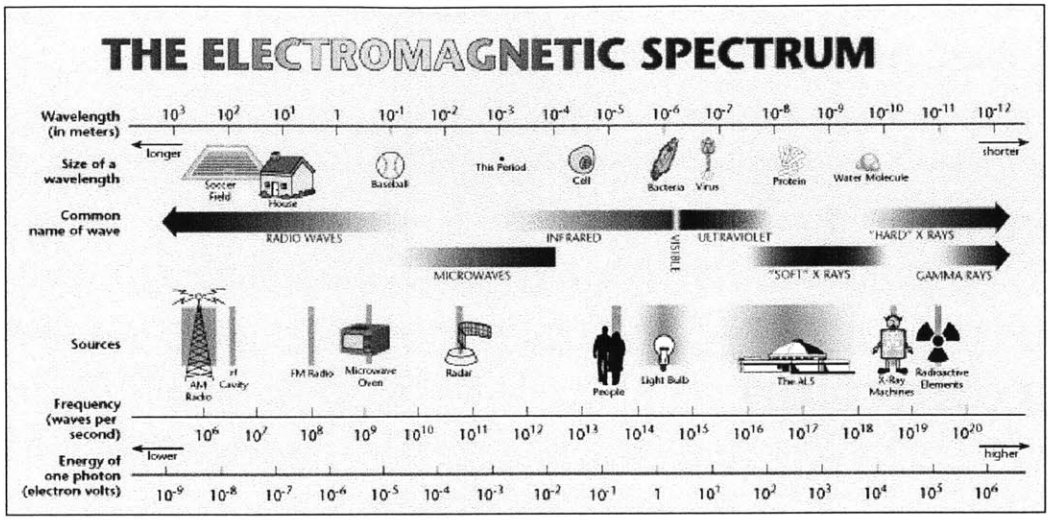

Figure 1-1: The electromagnetic spectrum. Figure taken from [1].

1.1 High Harmonic Generation

In High Harmonic Generation (HHG) an atom irradiated by a strong laser field, can generate a wide spectrum of harmonics into the EUV and soft X-ray region of the spectrum, that emerge as a coherent, low divergence beam. An intense fsec pulse in the visible range focuses into a gas generating a broad spectrum of harmonics of the drive frequency down to really short wavelengths (hundred times lower wavelengths than the driving wavelength). Starting in 1990's, people discovered how this process works. A strong electric field suppresses the potential barrier felt by a valence electron of the atom, the electron becomes free and is accelerated in this laser field, first away and then back towards the atom and when it recollides it can emit an EUV or X-ray photon (Figure 1-2) [2, 3].

In the harmonic spectrum, we see that there is a long "plateau" of constant amplitude over a large spectral range, followed by a sudden drop of the harmonic emission which is the cutoff. The cutoff corresponds to the maximum emitted photon energy. Due to the periodic repetition of the process (ionization, propagation and recombination), the resulting dipole emission spectrum is discrete and because of the half cycle symmetry of the dipole moment, only odd harmonics separated by twice the laser frequency ω_0 survive (Figure 1-3).

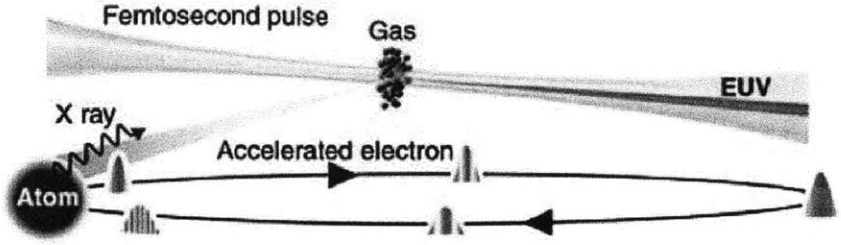

Figure 1-2: High Harmonic Generation. Figure taken from [4].

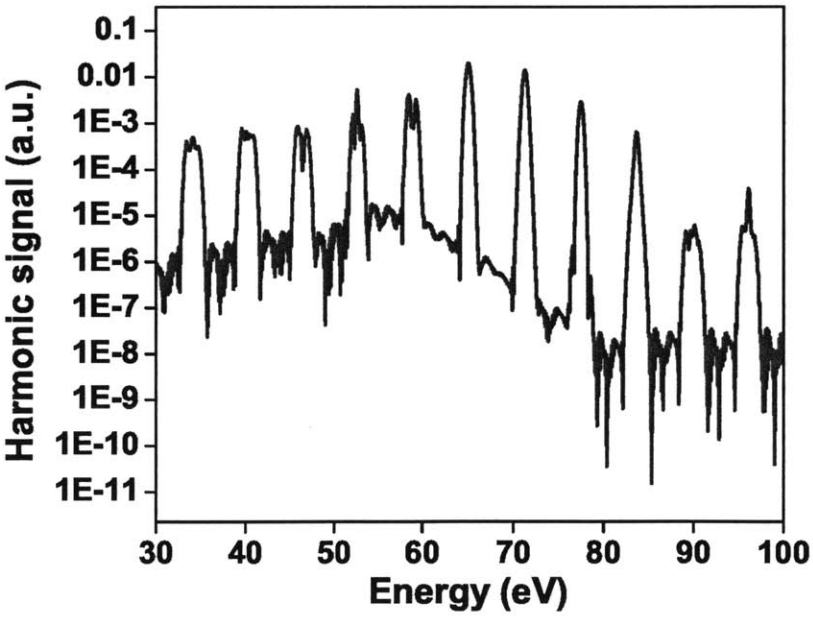

Figure 1-3: High Harmonic Generation spectrum.

1.2 Applications

HHG can be used to develop and utilize compact and powerful soft X-ray sources that will be of modest size and cost and will enable imaging and spectroscopy applications that in the past have been only possible at large scale synchrotron and X-ray free electron lasers (X-FELs) (Figure 1-4). In addition, the radiation from the compact source would offer properties such as spatial coherence, femtosecond and eventually attosecond time resolution. These properties are not possible at synchrotrons and hard to implement in X-FELs. For imaging applications in the water window region, an estimated coherent X-ray flux radiation in the 2-5 nm wavelength range producing 10^{10} photons/sec in 1% bandwidth is required. Such flux levels are currently only possible at third generation synchrotrons and with femtosecond pulses only at X-ray FELs, like SLAC or FLASH.

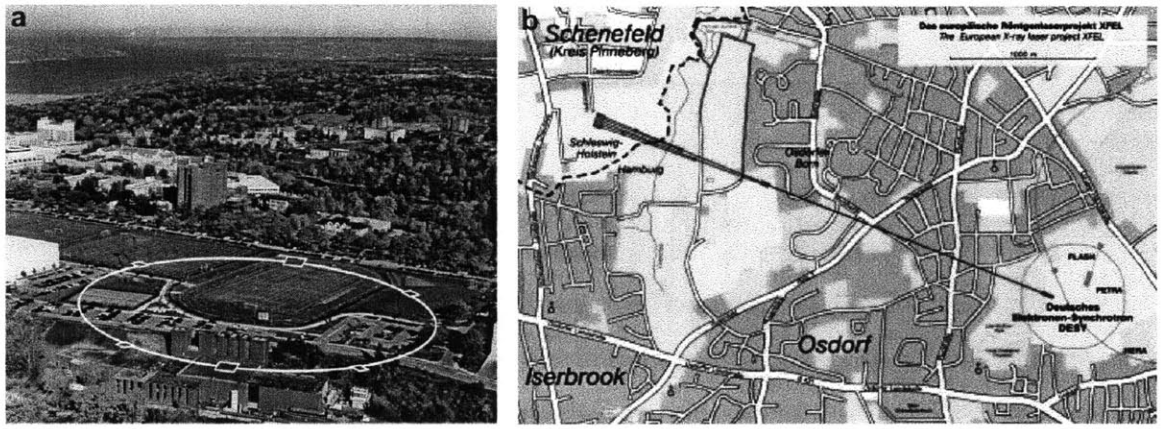

Figure 1-4: a) Cornell High Energy Synchrotron Source (CHESS) at Cornell, Ithaca, NY, b) X-ray Free Electron Laser at DESY, Hamburg, Germany.

Some of the applications of HHG are the following:

1.2.1 Angle Resolved Photoemission Spectroscopy

Angle resolved photoemission spectroscopy (ARPES) has the unique ability to resolve the electronic band structure of materials in momentum space. Photons of energy higher than

the work function are used to eject electrons and by measuring the energy and momentum of these photo-ejected electrons, one can obtain the energy-momentum dispersion relation inside the material (Figure 1-5). ARPES has helped scientists understand the physics of materials such as graphene and strongly correlated materials. Traditionally, these experiments are performed at synchrotrons which can provide tunable high energy photons. With the advent of the femtosecond lasers, it has recently become possible to perform ARPES by using harmonics of lasers. Initially, scientists used fourth harmonics of Ti:sapphire lasers at 6 eV as the light source. The advantage of using lasers as the light source compared to synchrotrons is that lasers provide higher energy and momentum resolutions, yielding in much sharper spectra. Laser-based ARPES experiments [5] can provide 3D dispersion (energy and two components of momentum) as opposed to 2D dispersion that can be obtained at synchrotrons. Laser-based ARPES has also made it possible to add time resolution to these experiments by using pump-probe method to record a femtosecond movie of electronic band structure after photo-excitation by another laser pulse. However, initial laser-based ARPES experiments were limited to 6 eV. This seriously restricts the range of accessible momentum values in k-space. For some problems, the dynamics of interest are near the edge of the Brillouin zone and are inaccessible to this method. In addition, in order to obtain the dispersion in the direction normal to the sample surface, one needs to vary the energy of the light source. For all these reasons there has been a great need in the ARPES community for HHG-based light sources that can reach to high energies up to 500 eV.

1.2.2 Coherent Water Window X-ray Generation for Applications in Bio-imaging

The implementation of a powerful coherent X-ray source has been a main goal for researchers. X-ray microscopy, with a resolution of a few tens of nm, is an emerging technique that has the capability of bridging the gap between optical (submicron resolution) and electronic microscopy (few nm resolution) [7]. The spectral range of 284-543 eV (between the Carbon

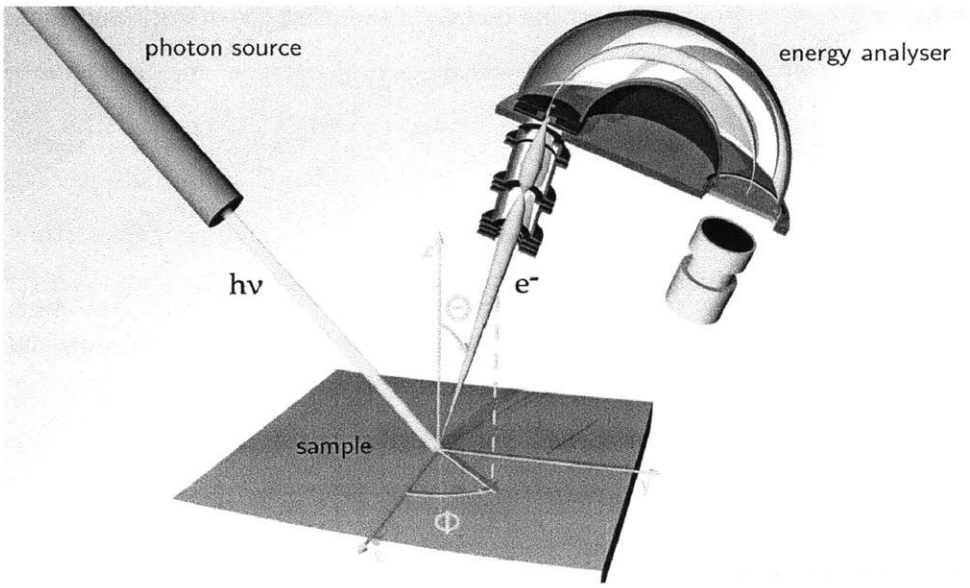

Figure 1-5: Experimental setup for Angle resolved photoemission spectroscopy (Figure taken from [6]).

and the Oxygen K-absorption edges), which is called water window region, is attractive for high-contrast biological imaging.

Between the K edges of Carbon (284 eV, 4.37 nm) and Oxygen (543 eV, 2.28 nm), the natural contrast between water and Carbon-rich tissues, like proteins and lipids, is quite strong, as shown in Figure 1-6, which shows the difference in transmission when 100 nm of water is replaced with 100 nm of carbonaceous compounds [8]. The decrease in transmission compared to the surrounding water is 5%-10% at 500 eV and 10%-20% at 350 eV.

An intense water window X-ray pulse would allow scientists to capture images of live cells by instantaneously halting their motion, without the cumbersome staining and slicing preparation needed by electron microscopy. Also the sample's preparation process for electron microscopy has a high risk of alteration of the structural information.

So far, X-ray microscopy has been possible through synchrotron facilities. Several beam lines have performed X-ray microscopy in the water window. However, images of live cells cannot be captured without freezing the sample. In addition, the necessity of long term planning, and of transfering the samples from the biology laboratory to the beam line are a

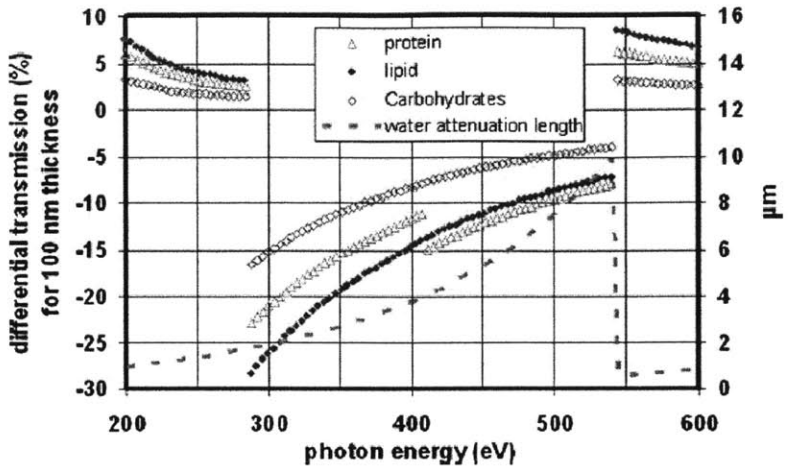

Figure 1-6: Differential transmission of a 100 nm layer of proteins (34% C, 50% H, 8% O, 8% N), lipids (32% C, 64% H, 4% O), carbohydrates (25% C, 50% H, 25% O), replacing the same thickness of water. At 400 eV a 100 nm thick lipid transmits 15% less than the water it replaces (Figure taken from [7]).

strong drawback for the use of synchrotrons.

HHG using a tabletop laser system is an alternative approach for generating coherent water window X-rays. However, the output photon flux at 300 eV is still low and the conversion efficiency around 10^{-9}.

1.2.3 Lithography at EUV Wavelengths

The electronics community has always aimed to the miniaturization of integrated circuits (ICs). The technique which is currently used to produce ICs is photolithography, or optical lithography, which consists in shining a photo resist, a material sensitive to light, with an optical beam. The photo resist substrate is the circuit board, and the materials used to produce circuits are chemically deposited on the pattern drawn by light on the photo resist. Current techniques are capable of producing sub-100-nm features by using UV light at 193 nm from excimer lasers, but for further miniaturization it is necessary to use shorter wavelengths.

Extreme UV (EUV) lithography is one of the most promising techniques within Next Generation Lithography (NGL) [9]. EUV lithography uses light at 13.5 nm (92 eV), which is the wavelength at which Mo/Si mirrors have a relatively high 72% reflectivity [10]. The present sources of such light are either discharge or laser produced, and suffer from low efficiency, incoherence and non-directionality.

HHG-based sources using short wavelength drive lasers and femtosecond enhancement cavities with Helium as the HHG medium may result in highly efficient EUV sources. The advantage of HHG sources is the fact that they offer the possibility of a spatially coherent source, when compared to plasma sources and also would not produce debris that may destroy downstream imaging optics.

1.2.4 Attosecond Pulse Generation

HHG is currently the only experimentally proven method for generating attosecond pulses [11, 12]. Attosecond science has opened the door to real-time observation and time-domain control of atomic-scale electron dynamics. The time structure of harmonic emission forms the basis of the generation of attosecond pulses. In order to achieve emission in the fraction of a femtosecond, we need to filter a limited band of photon energies near their maximum (cutoff).

For many applications, single attosecond pulses (one burst per laser pulse) are preferred. For a few-cycle pulse, the highest harmonic radiation is emitted only during the single laser cycle where the highest electron recollision energies are reached. In this case, the harmonic spectrum has a smooth and unmodulated cutoff. In the time domain, the smooth spectrum at the cutoff corresponds to an isolated attosecond burst of radiation.

In the case of multi-cycle laser pulses the release and recollision process is repeated periodically and the discrete structure of the harmonic spectrum is pronounced (i.e. pronounced peaks at odd multiples of the fundamental frequency). As a result not a single pulse, but a train of harmonic pulses is generated. The smoothness of the cutoff and emission of single pulse depend on the carrier-envelope phase .When the laser field is cosine-shaped (ϕ_{CE}=0)

and consists of few oscillation cycles (few cycle pulse), only one electron (the most energetic one) with the maximum recollision energy has enough energy to contribute to the filtered high-energy emission. Correspondingly, only a single high frequency attosecond burst of radiation is emitted (Figure 1-7).

By appropriately changing the carrier-envelope phase, the cosine waveform of the driving laser field turns to a sinusoidally shaped one ($\phi_{CE} = \pi/2$) and as a result the attosecond photon emission changes remarkably. Instead of a single pulse, two identical bursts are transmitted to the EUV bandpass filter (Figure 1-7). The reason is that in this case there are two electrons which have equally high maximum recollision energy. So, two attosecond pulses are generated that are separated by half the laser optical period, because the two electrons that recollide with the maximum harmonic energy have birth and as a consequence arrival times separated by half cycle. In the harmonic frequency spectrum the additional time structure appears as a modulation close to the cutoff.

The shortest duration of a single attosecond pulse is limited by the bandwidth within which only the most energetic recollision contributes to the emission. In a 5 fsec, 750 nm laser pulse this bandwidth is about 10% [13]. For photon energies of $\sim$ 100 eV this corresponds to a bandwidth of $\sim$ 10 eV, so pulses of about 250 attoseconds are generated. For a photon energy of 1 keV, a driver laser field with the above properties will lead to a single pulse emission over a bandwidth of around 100 eV, which corresponds to 25 attoseconds [14]. Taking into account that the atomic unit of time is 24.189 attoseconds, we can say that it is possible to push the frontiers of attosecond technology near the atomic unit of time.

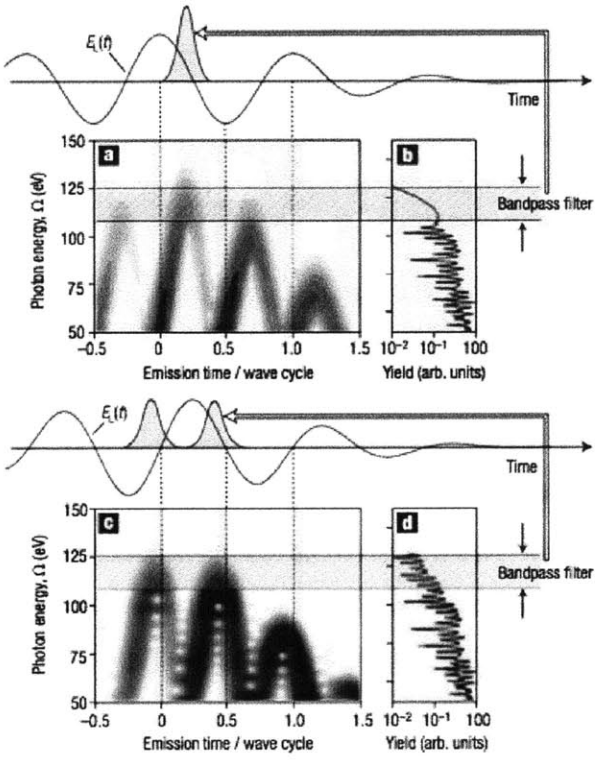

Figure 1-7: Generation of single and twin attosecond pulses. The driving wavelength is 750 nm and the laser pulse is 5 fsec. a and c show the emitted photon energy at each recombination event for each half cycle of the driving field. b and d show the spectra of the emitted EUV photons. By filtering a limited band of photon energies near the cutoff, we get a single attosecond pulse in the case of a cosine-shaped driving field (a and b) and twin attosecond pulses for a sine-shaped driving field (c and d). Figure is taken from [13].

1.3 Motivation

HHG suffers from low efficiencies (Figure 1-8). Efficiencies of few times 10^{-4} at 20 eV have been achieved in Xenon [15] and efficiencies in the range of 10^{-4} have been reported in Helium using 400 nm driver [16], while for 800 nm driver the efficiency is 2-3 orders of magnitude lower [15, 16]. Using a two-color laser field (400 and 800 nm) improves the efficiency in Helium [16, 17] up to few times 10^{-4}, but the efficiency still remains low.

Thus, a detailed analysis of how the efficiency scales with laser and material parameters is of great importance. Due to the computational complexity of the problem, which includes not only the microscopic response of the medium but also propagation effects, computed HHG spectra are often given in arbitrary units, unless parameter fitting is employed to match the experiments. Accurate quantitative simulation of the HHG efficiency can be extremely time-consuming and considering the number of variables involved in the HHG process, a systematic study with several quantities varying simultaneously is prohibitive. No complete expression for the HHG efficiency and its scaling as a function of various parameters was presented. The scaling of conversion efficiency was analyzed only in terms of laser wavelengths and pressure.

In addition, in the HHG process there are complicated spatiotemporal propagation effects, such as plasma defocusing which distorts the pulse and losses due to electron-neutral inverse bremsstrahlung. These phenomena change the phase matching along propagation, resulting in non coherent harmonic generation and consequently poor efficiencies. It is crucial to analyze the influence of those phenomena and find ways to mitigate them.

Thus, by investigating the factors which limit the HHG process and finding ways to increase the HHG efficiency, we can develop table-top HHG-based EUV/X-ray sources (Figure 1-9).

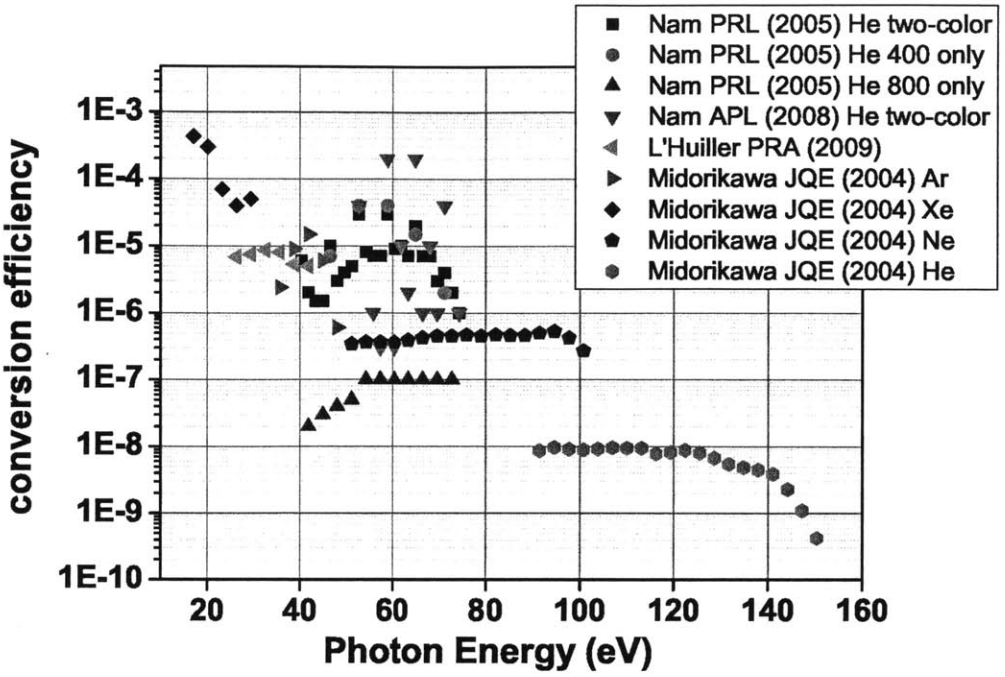

Figure 1-8: Efficiencies of HHG experiments.

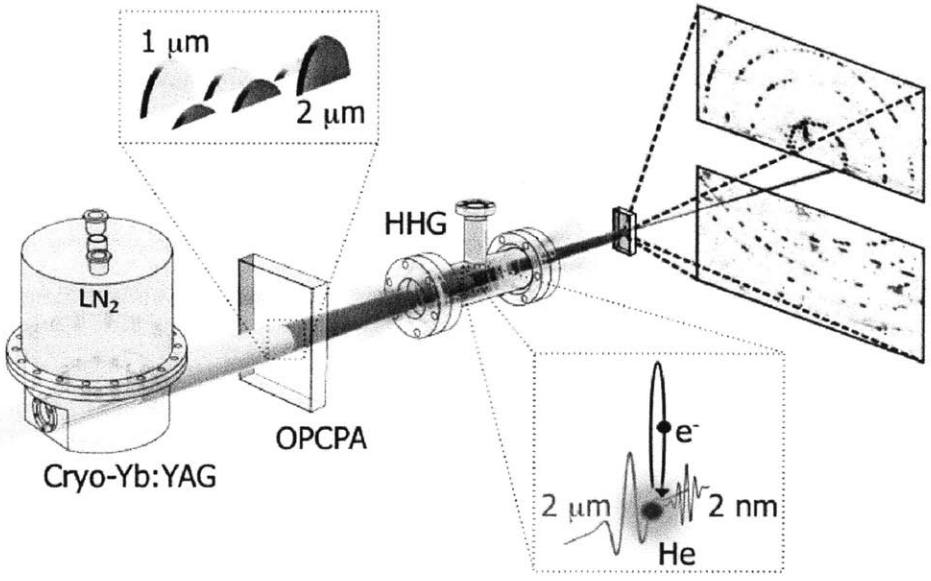

Figure 1-9: Table-top HHG-based EUV/X-ray source.

1.4 Preview of Thesis

The goal of this thesis is to achieve theoretical optimization of HHG efficiency. In this direction, we derived a semi-analytical formula for efficiency in 1-D and we performed numerical modeling of the problem in 3-D. In Chapters 2-4 we give the context of the work and we describe the basic modeling of HHG and in Chapters 5-7 we describe our contribution to the field.

In Chapter 2 we describe the microscopic phenomena of the HHG process and we discuss in detail one of the most successful models for describing HHG, the Three Step Model. In this model, HHG is split in three steps, ionization, propagation and recombination.

In Chapter 3 we deal with the macroscopic phenomena. Starting from the wave equation, we study the propagation of the driving field, initially in 1-D and then in 3-D. We first assume that the driving field is a plane wave, which is valid if the the pulse is loosely focused, and we form the harmonic field in such a way that can be used later for the derivation of the efficiency formula. We then move to 3-D and we describe the four terms of phase mismatch and the effects of plasma defocusing and electron-neutral inverse bremsstrahlung. One important result of this Chapter is the dependence of plasma defocusing and inverse bremsstrahlung on pressure.

In Chapter 4 for completeness and to be self-contained, we give a detailed derivation of the single atom response in the single active electron approximation of the Three Step Model.

In Chapter 5 we derive an analytical expression for the calculation of the efficiency at a given odd harmonic in the plateau and cutoff region. The efficiency formula is based in the 1-D model and takes the laser and material parameters and macroscopic effects into account. The main result of this Chapter is that the efficiency per given harmonic scales with ω_0^6 in the plateau and with ω_0^5 in the cutoff region of the spectrum, where ω_0 is the driving frequency.

In Chapter 6 we compare the results of the efficiency formula with experimental results from the literature for 400 and 800 nm drivers and we show very good agreement. The main

result is that the efficiency for 400 nm is 1-2 orders of magnitude higher than the one at 800 nm. We also study the effects that interference of long and short trajectories have on the spectra. In addition, we investigate two different ionization models, the ADK and the Yudin-Ivanov and we show that the Yudin-Ivanov model, which includes both tunneling and multiphoton ionization, gives more accurate results especially for short drive wavelengths.

In Chapter 7, we extend the 1-D model to 3-D and we study the generation of radiation in the water window region of the spectrum by using driver pulses with 2 μm drive wavelength. We show that within the range of pressures one might choose for performing the experiment, at low pressures diffraction enhanced by plasma defocusing is the dominant limitation, at high pressures loss due to electron-neutral inverse bremsstrahlung is the main limitation and there is an intermediate regime of medium pressures, where both diffraction effects and loss due to electron-neutral inverse bremsstrahlung have an effect. These two effects do not allow phase matching to be maintained for long distance resulting in low efficiencies. Finally, we explore ways to mitigate the effect of plasma defocusing by using Supergaussian pulses and Gaussian pulses with large beam waists.

In Chapter 8 we give future directions for the research in this topic.

In Appendix A we describe our work in active mode-locking of QCLs. After describing the challenges of generating short pulses in QCLs, we study the impact of upper state lifetime and pumping level on pulse formation and then we move to the role of spatial hole burning in pulse shape and stability. The main result is that spatial hole burning reduces significantly the pulse duration, but leads to pulse instabilities and non stationary pulse generation from the laser.

Chapter 2

Microscopic Phenomena - Three Step Model

The dynamics of an atom according to the Three Step Model (TSM) are described in Figure 2-1. In step (a) the electric field (yellow line) alters the shape of the Coulomb potential, allowing the electron to tunnel through the barrier. In steps (b) and (c) the electron travels classically in the continuum (neglecting the influence of the Coulomb potential) and returns back to the atom when the electric field reverses direction. In step (d) the returning electron collides with the atom and may be scattered or recombined to the core. In the case of the latter, a high energy photon is released with total energy equal to the difference between the kinetic energy the electron gained in the laser field and the ionization potential -I_p. However, there is a chance that the laser field will remove the electron from the ion once for all.

2.1 Ionization

Ionization is the transition from inside to outside of the atom. It is assumed that only a single electron of the atom is ionized, while the rest of the electrons are frozen in the orbitals. This is often referred to as the Single Active Electron Approximation (SAEA) [18].

A rough distinction between the various regimes of atomic ionization can be made by con-

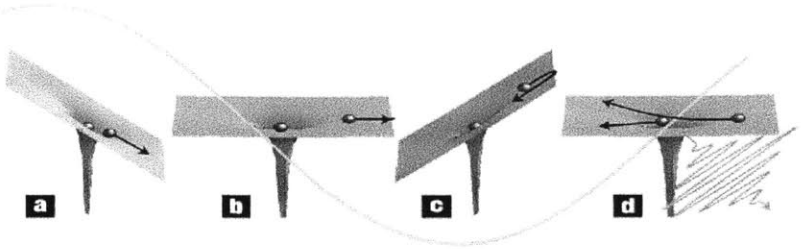

Figure 2-1: The three steps in the High Harmonic Generation Process. Figure taken from [13].

sidering the value of an adiabaticity parameter called the Keldysh parameter $\gamma = \sqrt{I_p/(2U_p)}$, where $U_p = E_0^2/(4\omega_0^2)$ is the time-averaged kinetic energy or ponderomotive energy, E_0 is the field amplitude, ω_0 is the driving frequency and I_p is the ionization potential. The Keldysh parameter is a measure of how adiabatic the process is and tells us how fast the barrier moves, while the electron tunnels [19].

For $\gamma \gg 1$ multiphoton ionization takes place [20]. It is dominant for small fields and as a consequence many photons are needed in order to achieve ionization. Note that we consider fields of frequency ω_0, such that $\hbar\omega_0 < I_p$ and therefore photoionization by a single photon is impossible.

For $\gamma \ll 1$ we are in the tunneling regime. In this regime the electric field is high and the frequency of the laser field is small. The electron ionizes by tunneling under the Coulomb barrier. This regime is called the quasistatic regime because the variation of the laser field is so slow that the instantaneous ionization rate coincides with a static one [21]. If $w(E)$ is the static (Stark) ionization rate as function of the electric field, we have

$$|a(t)|^2 = \exp\left(-\int_0^t w(E(t'))dt'\right) \tag{2.1}$$

where $a(t)$ is the probability amplitude of finding the atom in the ground state. In fact even for $\gamma \leq 2/3$ the approximation is satisfactory [22].

Tunnel ionization depends on the electric field strength in a strongly nonlinear way. The static ionization rate $w(E)$ is well described in the tunnel ionization regime by the Ammosov-Delone-Krainov (ADK) formula [21]. The ADK formula is

$$w(E) = \frac{4^{n^*}}{n^*\Gamma(2n^*)} I_p(2l+1) \left(\frac{2(2I_p)^{3/2}}{|E|} \right)^{2n^*-1} \exp\left(-\frac{2(2I_p)^{3/2}}{3E} \right) \tag{2.2}$$

where $n^* = 1/\sqrt{2I_p}$ and l is the total angular momentum quantum number of the valence orbital, which is 1 for all noble gases apart from Helium (for which it is 0). Γ is the gamma function. We should mention that the magnetic quantum number m is equal to 0 in the above formula. The ADK formula has also been extended to molecules [23]. The formula shows the characteristic exponential dependence of the ionization rate on the inverse of the field strength and due to this nonlinearity, in the case of tunneling field strengths, most electrons are released at times when the field reaches its peak.

2.2 Propagation

The electron appears in the continuum with zero velocity and is accelerated by the sinusoidal laser field. We assume that the field is so strong that we can neglect the influence of the Coulomb potential. This is called the Strong Field Approximation. We then treat the motion of the electron in the laser field classically. In Figure 2-2 we show the position of the electron as a function of time for different birth times. The blue color is the electric field. Depending on the phase of the laser field when the electron appears in the continuum, it may return back either at the first return to the nucleus or at another return. Also it may not return back at all.

As the electron propagates it acquires kinetic energy, due to the electric field and when it recombines a photon with energy $\hbar\omega_{EUV} = I_p + 0.5m\dot{x}^2$ is emitted. For each value of energy there is a pair of trajectories, which return back to the nucleus with the same velocity and as a result the emitted photons have the same energy. The trajectory with the earlier birth time and as a result the later arrival time is called long trajectory, while the trajectory with

the later birth time and as a result the earlier arrival time is called short trajectory. In Figure 2-2, with red color we show a pair of short and long trajectories. Another pair is shown with green color. The cyan line represents the trajectory which returns back with the maximum kinetic energy. This corresponds to the highest harmonic also known as the cut-off [3].

$$\hbar\omega_{max} = I_p + 3.17\frac{E_0^2}{4\omega_0^2} \tag{2.3}$$

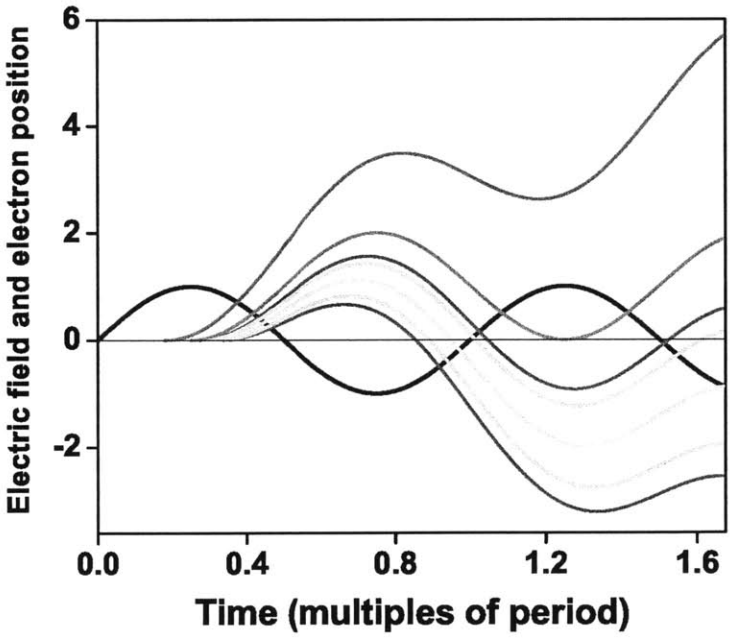

Figure 2-2: Electron trajectories under the influence of a driving field.

2.3 Recombination

The returning electron can recombine with the parent ion. During the propagation, the electron wavepacket undergoes quantum diffusion and by the time it returns back to the atom, it can become several hundred times larger than the atom itself. For 800 nm laser

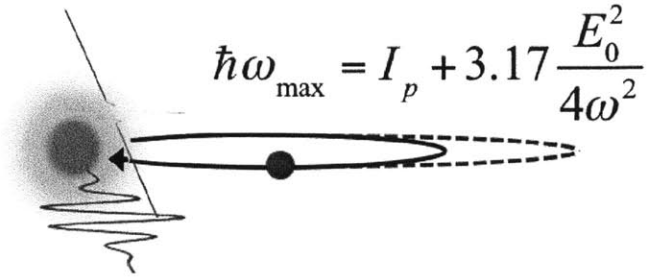

Figure 2-3: Electron trajecotry (solid line) and emission of EUV photon (purple). The trajectory of the electron which returns back with the maximum kinetic energy is shown with dashed line.

fields, the electron wave packet has a typical transverse 1/e width of 9 Angstroms by the time of recollision, much larger than the size of small molecules (typically $\sim$ 1 Angstrom) [24]. Therefore the wavepacket can be treated like a plane wave. The recombination amplitude is then the dipole moment between the plane wave and the ground state.

$$a_{rec} = \langle g|x|k\rangle \tag{2.4}$$

In Figure 2-4 are shown the recombination amplitudes of the noble gases in the length gauge.

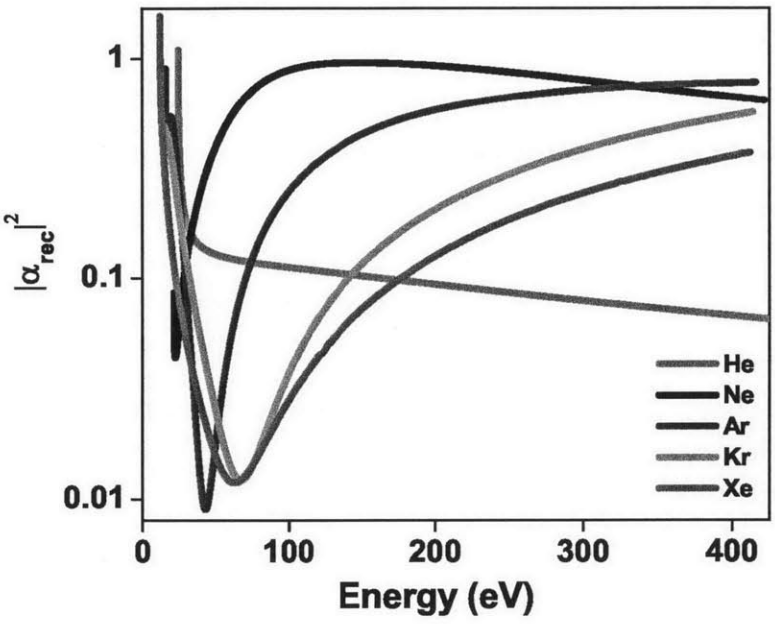

Figure 2-4: Recombination amplitudes for noble gases. Figure taken from [25].

Chapter 3

Macroscopic Phenomena

In this Chapter we describe the driving field propagation. We start with an 1-D model, assuming that the driving field is a plane wave propagating without distortion. Then we move to 3-D, considering the driving field to be a Gaussian pulse in time and space, taking into account the effects of plasma defocusing and electron-neutral inverse bremsstrahlung.

3.1 General Wave Equation

The general wave equation [26] describing the propagation of an electromagnetic field $E(r,z,t)$ in an isotropic dielectric medium characterized by an electronic polarization $P(r,z,t)$ is

$$\nabla^2 E(r,z,t) - \frac{1}{c^2}\frac{\partial^2 E(r,z,t)}{\partial t^2} = \frac{1}{\epsilon_0 c^2}\frac{\partial^2 P(r,z,t)}{\partial t^2} \tag{3.1}$$

where z is the propagation coordinate, r is the transverse coordinate, c is the speed of light and ϵ_0 is the electric permittivity of free space. We split the polarization P generated by the gas into its linear and nonlinear parts $P^{(1)}$ and P^{NL} and similarly, we can decompose the displacement D into a linear and nonlinear part.

$$D = \epsilon_0 E + P^{(1)} + P^{NL} = D^{(1)} + P^{NL} \tag{3.2}$$

Substituting D into the wave equation (Eq. 3.1), we rewrite the wave equation in a form that isolates the nonlinear polarization as the source for waves generated at new frequencies

$$\nabla^2 E(r,z,t) - \frac{1}{\epsilon_0 c^2}\frac{\partial^2 D^{(1)}(r,z,t)}{\partial t^2} = \frac{1}{\epsilon_0 c^2}\frac{\partial^2 P^{NL}(r,z,t)}{\partial t^2} \tag{3.3}$$

For the case of an isotropic material $D^{(1)} = \epsilon^{(1)}E$, where $\epsilon^{(1)}$ is a scalar quantity and using the refractive index of the medium, which we assume for the moment to be independent of frequency and position, $n = \sqrt{\epsilon^{(1)}/\epsilon_0}$ we obtain

$$\nabla^2 E(r,z,t) - \frac{n^2}{c^2}\frac{\partial^2 E(r,z,t)}{\partial t^2} = \frac{1}{\epsilon_0 c^2}\frac{\partial^2 P^{NL}(r,z,t)}{\partial t^2} \tag{3.4}$$

3.2 Model for 1-D Propagation

In the HHG experiment the gas jet is usually located at the focus. If the driving field is loosely focused, we can approximate it on focus as a plane wave.

We represent the harmonic field and the nonlinear polarization as a sum of their various frequency components [26]

$$E_h(r,z,t) = \sum_q E_q(r,z,t)e^{ik_q z} \tag{3.5}$$

$$P^{NL}(r,z,t) = \sum_q p_q^{NL}(r,t)e^{iqk_1 z} \tag{3.6}$$

where q is the order of each harmonic, $E_q(r,z,t)$ and $p_q^{NL}(r,t)$ are the envelopes of the harmonic field and the nonlinear polarization respectively. In the following, we assume that the nonlinear polarization of the medium does not change the fundamental driving field except for a change in its phase velocity due to the plasma generated. This effect enters only the wave number k_1, and therefore, the nonlinear polarization envelopes $p_q^{NL}(r,t)$ driving the harmonics do not depend on z. By substituting Eq. 3.5 and Eq. 3.6 into

Eq. 3.3 and performing the paraxial approximation, as well as the slowly varying envelope approximation, [27] we obtain a wave equation which is valid for each frequency component of the harmonic field

$$\nabla_\perp^2 E_q(r,z,t) + 2ik_q \frac{\partial E_q(r,z,t)}{\partial z} - k_q^2 E_q(r,z,t) - \frac{n^2}{c^2}\frac{\partial^2 E_q(r,z,t)}{\partial t^2} = \frac{1}{\epsilon_0 c^2}\frac{\partial^2 p_q^{NL}(r,z,t)}{\partial t^2} e^{i(qk_1 - k_q)z} \tag{3.7}$$

We substitute in Eq. 3.7 the Fourier transforms of the harmonic field E_q and the nonlinear polarization p_q^{NL}

$$\tilde{E}_q(r,z,\omega_q) = \frac{1}{\sqrt{2\pi}} \int_0^T E_q(r,z,t) e^{i\omega_q t} dt \tag{3.8}$$

and

$$\tilde{p}_q^{NL}(r,\omega_q) = \frac{1}{\sqrt{2\pi}} \int_0^T p_q(r,t) e^{i\omega_q t} dt \tag{3.9}$$

with $\omega_q = q\omega$, and we define $\tilde{p}_q^{NL}(r,\omega_q) = \rho \tilde{d}_q(r,\omega_q)$, where d_q is the dipole moment and ρ is the density of atoms. Thus

$$\frac{c}{2i\omega_q}\nabla_\perp^2 \tilde{E}_q(r,z,\omega_q) + \frac{\partial \tilde{E}_q(r,z,\omega_q)}{\partial z} = -\frac{1}{2\epsilon_0 c}\rho \tilde{v}_q(r,\omega_q) e^{i(qk_1 - k_q)z} - \frac{\rho\sigma(\omega_q)}{2}\tilde{E}_q(r,z,\omega_q) \tag{3.10}$$

where σ is the absorption cross section and $\tilde{v}(\omega)$ is the dipole velocity.

If we neglect the transverse Laplace operator term $\nabla_\perp^2$ in Eq. 3.10, i.e. convert to a one-dimensional propagation situation, and introduce atomic units ($4\pi\epsilon_0 = 1$), and $c = \alpha^{-1}$, we obtain a purely one-dimensional equation for the amplitudes of the plane waves [28]

$$\frac{\partial \tilde{E}_q(r,z,t)}{\partial z} = -(2\pi\alpha\rho)\tilde{v}_q(\omega_q) e^{i(qk_1 - k_q)z} - \frac{\rho\sigma(\omega_q)}{2}\tilde{E}_q(z,\omega_q) \tag{3.11}$$

Note, that in our derivation we have neglected the depletion of the fundamental field. Since $\tilde{v}(\omega)$ does not depend on z, i.e. the changes in amplitude and phase of the driving

pulse are small over the medium length L, the solution to Eq. 3.11 is:

$$\tilde{E}_h(\omega) = -\frac{4\pi\alpha\tilde{v}(\omega)}{\sigma(\omega)} g(\Delta k, L) \tag{3.12}$$

where

$$g(\Delta k, L) = \frac{e^{i(\Delta k \cdot L) - e^{-L/(2 \cdot L_{abs})}}}{1 + 2i(\Delta k \cdot L_{abs})} \tag{3.13}$$

describes the macroscopic response of the medium (Figure 3-1) and $L_{abs} = 1/(\rho\sigma)$ is the absorption length. If perfect phase matching conditions are satisfied, i.e. $\Delta k = 0$, and the propagation distance L is long compared to the absorption length L_{abs}, i.e. absorption limited conditions, then $|g(\Delta k, L)| = 1$ and Eq. 3.12 approaches its absorption limited value $\tilde{E}_h(\omega) = -4\pi\alpha\tilde{v}(\omega)/\sigma(\omega)$. Eq. 3.13 is valid for nonlinear optics in general and can be rewritten as a function of the ratios of medium length to absorption length and coherence length, $L_{coh} = \pi/\Delta k$, to absorption length. In general for $L > 3L_{abs}$ and $L_{coh} > 5L_{abs}$ the macroscopic response is at least half the maximum response [29, 30].

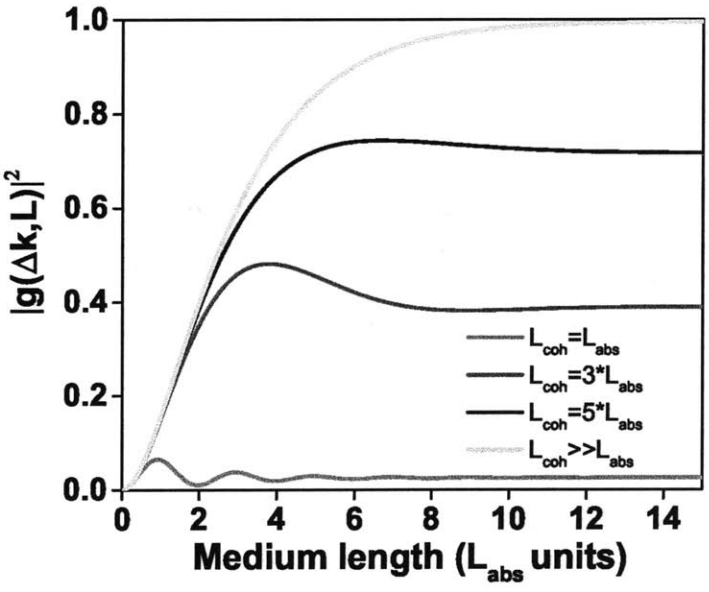

Figure 3-1: Macroscopic response as a function of the ratios between L/L_{abs} and L_{coh}/L_{abs}.

3.3 Model for 3-D Propagation

The driving field is not assumed to be a plane wave anymore, but a Gaussian pulse in space and time. The propagation equation for the driving field should include the effects of diffraction, self-focusing, plasma defocusing, ionization loss and electron-neutral inverse bremsstrahlung. In the slowly evolving wave approximation, a first order propagation equation is [31]

$$\frac{\partial E}{\partial z} = \frac{i}{2k}\nabla_{\perp}^2 E + i\frac{k}{2}n_2\epsilon_0 c|E|^2 E - \frac{1}{2c}\int_{-\infty}^{\tau} \omega_p^2 E d\tau' - \frac{I_p}{2c\epsilon_0 Re(E)^2}\frac{\partial \rho}{\partial \tau}E - \frac{\sigma_{IB}}{2}(1+i\omega\tau_{sc})\rho E \quad (3.14)$$

where, E is the complex representation of the electric field; z and τ are the propagation distance and the retarded time in the retarded time frame respectively; k is the wave-vector at the carrier frequency; $\nabla_{\perp}^2$ is the transversal Laplace operator; n_2 is the nonlinear index of refraction; ω_p is the plasma frequency; I_p is the ionization potential of the atom; ρ is the number density of the ionized atoms; σ_{IB} is the cross section for electron-neutral inverse bremsstrahlung; τ_c is the electron collision relaxation time. Because of cylindrical symmetry, E is a function of z , τ and the radial coordinate r .

3.4 Phase Mismatch

If the driver field is assumed to be a Gaussian beam,

$$E_1(r,z,t) = \frac{bE_0}{b+2iz}\exp\left(-\frac{k_1 r^2}{b+2iz}\right)\exp\left(-2ln(2)\left(\frac{t}{\tau}\right)^2\right)e^{ik_1 z} \quad (3.15)$$

not modified as it propagates in the medium, where E_0 is the field amplitude, τ is the full width at half maximum, b is the laser confocal parameter, then the polarization of the q-th

harmonic can always be written as

$$\tilde{P}_q(r,\omega_q) = \rho\tilde{d}_q(r,\omega)\exp\left(iq\left(k_1 z - tan^{-1}\left(\frac{2z}{b}\right) + \frac{2k_1 r^2 z}{b^2+4z^2}\right)\right) \tag{3.16}$$

where the dependence of the dipole amplitude $\tilde{d}_q(r,\omega)$ as a function of the electric field is not yet determined. With Eq. 3.16 we can write:

$$\frac{c}{2i\omega_q}\nabla_\perp^2\tilde{E}_q(r,z,\omega_q) + \frac{\partial\tilde{E}_q(r,z,\omega_q)}{\partial z} = \frac{1}{2\epsilon_0 c}i\omega_q\rho\tilde{d}_q(r,\omega_q)e^{i(qk_1-k_q)z}e^{iq\left(-tan^{-1}\left(\frac{2z}{b}\right)+\frac{2k_1r^2z}{b^2+4z^2}\right)}$$

$$-\frac{1}{2L_{abs}}\tilde{E}_q(r,z,\omega_q) \tag{3.17}$$

The derivative of the dipole amplitude in the frequency domain $i\omega_q\rho\tilde{d}_q(r,\omega_q)$ is related to the dipole acceleration

$$-i\omega_q\tilde{d}_q(r,\omega_q) = \frac{\tilde{\ddot{\xi}}(\omega_q)}{i\omega_q} = \frac{|\tilde{\ddot{\xi}}(\omega_q)|e^{-i\tilde{S}_q}}{i\omega_q} \tag{3.18}$$

where $\tilde{S}$ is the action. Eq. 3.17 can be written as

$$\frac{c}{2i\omega_q}\nabla_\perp^2\tilde{E}_q(r,z,\omega_q) + \frac{\partial\tilde{E}_q(r,z,\omega_q)}{\partial z} = \frac{1}{2\epsilon_0 c}\rho\frac{1}{i\omega_q}|\tilde{\ddot{\xi}}(\omega_q)|e^{-i\tilde{S}_q}e^{i(qk_1-k_q)z}e^{iq\left(-tan^{-1}\left(\frac{2z}{b}\right)+\frac{2k_1r^2z}{b^2+4z^2}\right)}$$

$$-\frac{1}{2L_{abs}}\tilde{E}_q(r,z,\omega_q) \tag{3.19}$$

The phase is

$$\phi(z) = (qk_1 - k_q)z - qtan^{-1}\left(\frac{2z}{b}\right) + q\frac{2k_1r^2z}{b^2+4z^2} - \tilde{S}_q \tag{3.20}$$

The two first terms of Eq. 3.20 account for the phase mismatch due to plasma and neutral dispersion, the third and fourth terms are the geometric phase and the last term is the dipole phase [32–34]. The difference $k_q - qk_1$ can be written as $qk_0n(\omega_q) - qk_0n(\omega_0)$, where n is the refractive index and ω_0 is the driving frequency.

The refractive index can be written as $n^2(\omega) = 1 + \chi(\omega)$, with $\chi(\omega)$ being the di-

electric susceptibility. For an optically thin medium, i.e. $\chi \ll 1$, $n(\omega) = 1 + \chi(\omega)/2$. The susceptibility has contributions from the neutral atoms and the plasma and can be written as $\chi(\omega) = \chi_{neutral}(\omega) + \chi_{plasma}(\omega)$, with $\chi_{plasma/neutral}(\omega) = N_{bound/free}\alpha(\omega)/\epsilon_0$, where $N_{bound/free}$ is the density of atoms and $\alpha_{neutral/plasma}(\omega)$ is the polarizability. Since $\alpha_{plasma} = -e^2/m\omega^2$, the refractive index can be written as

$$n = 1 + \frac{N_b \alpha_{neutral}(\omega)}{2\epsilon_0} - \frac{N_{free}}{2\epsilon_0}\frac{e^2}{m\omega^2} \tag{3.21}$$

where N_b is the density of the neutral atoms and N_f is the density of the electrons freed by ionization [32].

The density of atoms N is equal to PN_{1Atm}, where P is the pressure in atmospheres and N_{1Atm} is the density of atoms for 1 atmosphere. If we define as δ the ionization level, then $N_b = (1-\delta)N$ and $N_f = \delta N$. Then the refractive index, taking into account the contribution from neutral atoms and free electrons can be written as

$$n = 1 + \frac{(1-\delta)PN_{1Atm}\alpha_{neutral}(\omega)}{2\epsilon_0} - \frac{\delta PN_{1Atm}e^2/(m\omega^2)}{2\epsilon_0} \tag{3.22}$$

The phase mismatch Δk is equal to the derivative over z of the phase ($r = 0$) [35]

$$\begin{aligned}\Delta k =& \frac{d\phi}{dz} = \\ =& \frac{qk_0}{2\epsilon_0}PN_{1Atm}(1-\delta)(\alpha_{neutral}(\omega_0) - \alpha_{neutral}(\omega_q)) - \frac{q}{2\omega_0 c}\delta PN_{1Atm}\frac{e^2}{m\epsilon_0} - q\frac{2}{b}\frac{1}{1+\frac{4z^2}{b^2}} - \nabla S\end{aligned} \tag{3.23}$$

3.5 Plasma Defocusing

The imaginary part of $\frac{1}{2c}\int_{-\infty}^{\tau} \omega_p^2 E d\tau'$ in Eq. 3.14 describes the plasma defocusing. Plasma defocusing starts to become important as the free electron density increases and as a result the higher the pressure the stronger the plasma defocusing. A previous study has shown

that plasma defocusing in Neon at 80 mbar can significantly reduce the peak intensity of an 800 nm driver pulse and diverges the driver pulse energy within a few hundred microns [36]. This effect not only decreases the cutoff photon energy but also shortens the interaction length for HHG.

The physical origin of plasma defocusing comes from the difference between the refractive indices at the center and the wings of the pulse along the radial coordinate r. Inside the gas jet there is a distribution of atoms. As the driving field propagates along the z direction in the gas, it ionizes the electrons and plasma (free electrons) is created. Since the intensity at center of the pulse is higher than the intensity away from the center, more electrons are ionized at the center than at increasing radii and as a result the center of the pulse "sees" more plasma. The plasma contribution to the refractive index is negative (see Eq. 3.21) and as a result the total refractive index at the center of the gas jet is smaller than the refractive index around the center. Since the velocity is inverse proportional to the refractive index, the center of the pulse travels faster than that around the center and thus the pulse gets defocused. Thus, the plasma behaves like a concave lens.

Figure 3-2 shows the peak intensity versus radial coordinate r and propagation z when a 10 mJ, 35 fsec, 2 μm drive wavelength and 177 μm beam waist laser pulse propagates from negative z to positive z through a Helium jet, 2 mm long, with two different pressures, one very low (0.1 bar) in Figure 3-2.a and one very high (10 bar) in Figure 3-2.b.

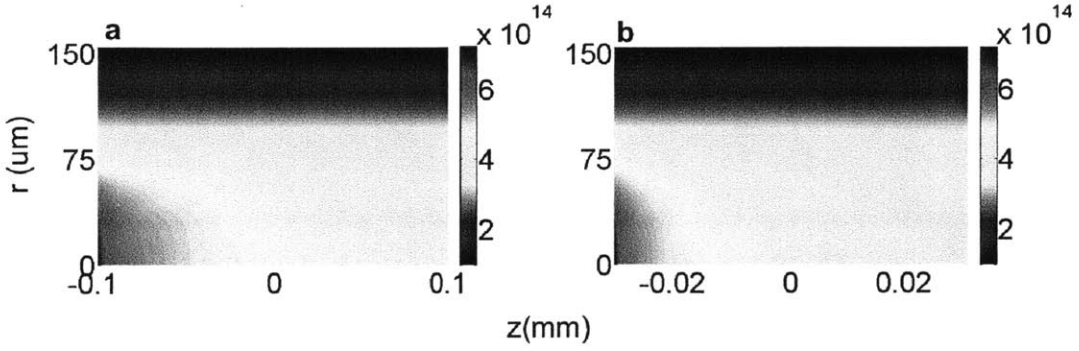

Figure 3-2: Dependence of plasma defocusing on pressure. a) for small pressure of 0.1 bar there is no plasma defocusing, b) for high pressure of 10 bar plasma causes defocusing of the pulse at positive z. The colorbar shows the intensity in W/cm^2.

3.6 Electron-neutral Inverse Bremsstrahlung

Laser radiation is absorbed primarily by inverse bremsstrahlung. Inverse bremsstrahlung is the process of absorption of electromagnetic wave energy by the plasma, induced by electron-neutral and electron-ion collisions. It is called inverse because usually the electron has the energy and generates radiation, but here it first picks up the energy from the radiation and then it starts to radiate. The cross section for electron-neutral inverse bremsstrahlung is [37]

$$\sigma_{IB} = \frac{ke^2\tau_c}{\omega m\epsilon_0(1+(\omega\tau_c)^2)} \tag{3.24}$$

where k is the wavenumber, m and e are the electron mass and charge respectively, ω is the driving frequency and τ_c is the electron collision relaxation time.

In Figure 3-3, is shown the cross section for electron-neutral inverse bremsstrahlung as a function of pressure for drive wavelength 800 and 2000 nm.

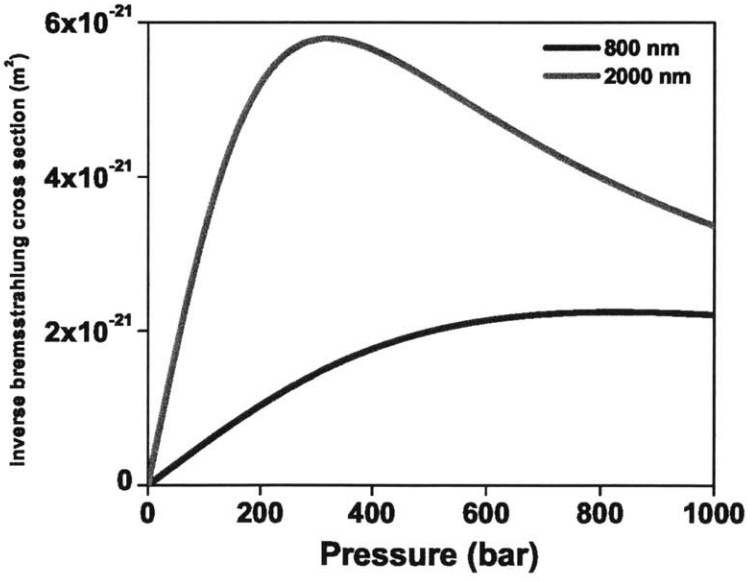

Figure 3-3: Electron-neutral inverse bremsstrahlung cross section as a function of pressure for drive wavelengths 800 and 2000 nm.

The electron collision relaxation time τ_c is inversely proportional to pressure and thus for small pressures, since $\omega\tau_c > 1$, the cross section is linearly proportional to pressure. The electron-neutral inverse bremsstrahlung cross section is small for 800 nm compared to 2000 nm, because the electron does not make such a large motion for the 800 nm wavelength.

Chapter 4

Single Atom Response

For completeness and to be self-contained, we give a detailed derivation of the single atom response in the single active electron approximation of the Three Step Model following the work of Lewenstein and Gordon [18,38].

4.1 The Single Active Electron Approximation

The Hamiltonian of an atom with a single electron in an external field in atomic units and in the dipole approximation is given by

$$H = -\frac{\nabla^2}{2} + V(x) - E(t)x + I_p \tag{4.1}$$

In the single active electron approximation the atom under the influence of an electric field satisfies, in the length gauge, the Schrödinger equation

$$i|\dot{\psi}(t)\rangle = H|\psi(t)\rangle = \left[-\frac{\nabla^2}{2} + V(\vec{r}) - E(t)x + I_p\right]|\psi(t)\rangle \tag{4.2}$$

where we have used atomic units ($\hbar = m = e = 1$), $|\psi(t)\rangle$ is the time dependent electron wave function, $V(\vec{r})$ is the atomic potential, I_p is the ionization potential and $E(t)$ is the

applied electric field which is polarized along the x direction. Note that we have shifted the energy scale by I_p, thus the ground state energy of the atom is aligned with the zero of the energy scale. Following [18,38] the time dependent electron wave function can be written as

$$|\psi(t)\rangle = \alpha(t)|0\rangle + |\phi(t)\rangle \tag{4.3}$$

where $|0\rangle$ is the ground state, $|\phi(t)\rangle$ represents the continuum part and $|\alpha(t)|^2$ is the probability that the electron is in the ground state. Then

$$H|\psi(t)\rangle = \alpha(t)H|0\rangle + H|\phi(t)\rangle \tag{4.4}$$

We know that

$$\left[-\frac{\nabla^2}{2} + V(x)\right]|0\rangle = E_1|0\rangle \tag{4.5}$$

where E_1 is the eigenvalue (energy) of the ground state. But $E_1 = -I_p$ and thus we add in both sides I_p, so that the energy level of the ground state $|0\rangle$ is zero. Then we have

$$\left[-\frac{\nabla^2}{2} + V(x) + I_p\right]|0\rangle = (E_1 + I_p)|0\rangle = 0 \tag{4.6}$$

Since

$$H|0\rangle = \left[-\frac{\nabla^2}{2} + V(x) + I_p - E(t)x\right]|0\rangle = -E(t)x|0\rangle \tag{4.7}$$

then

$$H|\psi(t)\rangle = -E(t)x\alpha(t)|0\rangle + H|\phi(t)\rangle \tag{4.8}$$

and the Schrödinger equation reads as

$$i\left(\dot{\alpha}(t|0\rangle) + |\dot{\phi}(t)\rangle\right) = -E(t)x\alpha(t)|0\rangle + H\phi(t)\rangle \tag{4.9}$$

The above equation is solved in two steps. To compute the amplitude of the ground state, we use the quasi-static approximation and thus $|a(t)|^2 = \exp\left(-\int_0^t w(E(t'))dt'\right)$, where $w(E)$

is the static ionization rate, given from the Ammosov-Delone-Krainov formula [21]. In order to get the equation for $|\phi(t)\rangle$ we apply the projector operator $P = 1 - |0\rangle\langle 0|$ from the left in Eq. 4.9. The motivation to do that is that $|\phi(t)\rangle$ should be orthogonal to the ground state wave function. Thus the left hand side of Eq. 4.9 becomes

$$\begin{aligned} iP\left(\dot{\alpha}(t|0\rangle) + |\dot{\phi}(t)\rangle\right) &= i\left(1 - |0\rangle\langle 0|\right)\left(\dot{\alpha}(t)|0\rangle + |\dot{\phi}(t)\rangle\right) \\ &= i\dot{\alpha}(t)|0\rangle - i|0\rangle\langle 0|\dot{a}(t|0\rangle + i|\dot{\phi}(t)\rangle \\ &= i\dot{\alpha}(t)|0\rangle - i\dot{\alpha}(t)|0\rangle + i\dot{\phi}(t)\rangle \\ &= i\dot{\phi}(t)\rangle \end{aligned} \tag{4.10}$$

since $\langle 0|\dot{\phi}(t)\rangle = 0$.

For the right hand side of Eq. 4.9, $-E(t)x\alpha(t)|0\rangle + H|\phi(t)\rangle$, we first apply the projector operator P on the term $-E(t)x\alpha(t)|0\rangle$:

$$\begin{aligned} -PE(t)x\alpha(t)|0\rangle &= -E(t)x\alpha(t)|0\rangle + |0\rangle E(t)\alpha(t)\langle 0|x|0\rangle \\ &= -E(t)x\alpha(t|0\rangle) \end{aligned} \tag{4.11}$$

Then we apply the projector P on the term $H|\phi(t)\rangle$:

$$\begin{aligned} &\left(1 - |0\rangle\langle 0|\right)H|\phi(t)\rangle = H|\phi(t)\rangle - |0\rangle\langle 0|H|\phi(t)\rangle \\ &= H\phi(t) - |0\rangle\langle 0| - \frac{\nabla^2}{2} + V(x) + I_p - E(t)x|\phi(t)\rangle \end{aligned} \tag{4.12}$$

We have $\langle 0| - \frac{\nabla^2}{2} + V(x) + I_p\rangle = \lambda_1\langle 0|\phi(t)\rangle = 0$, and thus the application of the projector on the term $H|\phi(t)\rangle$, gives $H|\phi(t)\rangle + |0\rangle\langle 0|E(t)x\phi(t)\rangle$. Thus, the right hand side becomes

$$H\phi(t) + |0\rangle\langle 0|E(t)x|\phi(t)\rangle - E(t)x\alpha(t)|0\rangle =$$

$$H_V|\phi(t)\rangle + V(x)|\phi(t)\rangle + |0\rangle\langle 0|E(t)x|\phi(t)\rangle - E(t)x\alpha(t)|0\rangle \tag{4.13}$$

where

$$H_V(t) = -\frac{1}{2}\nabla^2 - E(t)x + I_p \tag{4.14}$$

is the Volkov Hamilonian, i.e. the Hamiltonian of a free electron in the laser field neglecting the presence of the ionized core.

Thus the Schrödinger equation Eq. 4.9 becomes

$$i|\dot{\phi}(t)\rangle = H_V|\phi(t)\rangle + V(x)\phi(t)\rangle + |0\rangle\langle 0|E(t)x|\phi(t)\rangle - E(t)x\alpha(t)|0\rangle \tag{4.15}$$

If we use the strong field approximation (SFA), assuming that the freed electron does not "see" the core potential $V(x)$, $|\phi(t)\rangle$ satisfies approximately the equation (Volkov equation)

$$i|\dot{\phi}(t)\rangle = H_V(t)|\phi(t)\rangle - E(t)x\alpha(t)|0\rangle \tag{4.16}$$

4.2 Volkov Solutions

Initially we want to solve the homogeneous Volkov equation in order to find the time evolution operator or equivalently the Green's function, which we will use for the evaluation of the particular solution. The homogeneous Volkov equation is

$$i|\dot{\phi}_V(t)\rangle = H_V(t)|\phi_V(t)\rangle \tag{4.17}$$

We assume that the homogeneous solution is a time dependent eigensolution of the velocity operator $k(t)$ and can be written as

$$|\phi_V(t)\rangle = e^{if(t)}|k(t)\rangle \tag{4.18}$$

with $k(t)$ being the real momentum and $f(t)$ the action. We assume $k(0) = k$ and $f(0) = 0$. Substituting the ansatz in the homogeneous Volkov equation we obtain

$$i|\dot{\phi}_V(t)\rangle = -\dot{f}(t)e^{if(t)}|k(t)\rangle + ie^{if(t)}|\dot{k}(t)\rangle \tag{4.19}$$

and for the right hand side

$$H_V(t)|\phi_V(t)\rangle = \left(-\frac{\nabla^2}{2} + I_p\right) e^{if(t)}|k(t)\rangle - E(t)xe^{if(t)}|k(t)\rangle \tag{4.20}$$

But $v = -i\nabla$ so $v^2 = -\nabla^2$ and since $v|k\rangle = k|k\rangle$ we have

$$-\nabla^2|k(t)\rangle = k^2(t)|k(t)\rangle \tag{4.21}$$

So the right hand side of Eq. 4.17 is

$$H_V(t)|\phi_V(t)\rangle = \left(\frac{1}{2}k^2(t) + I_p\right) e^{if(t)}|k(t)\rangle - E(t)xe^{if(t)}|k(t)\rangle \tag{4.22}$$

and Eq. 4.17 becomes

$$-\dot{f}(t)e^{if(t)}|k(t)\rangle + ie^{if(t)}|\dot{k}(t)\rangle = \left(\frac{1}{2}k^2(t) + I_p\right) e^{if(t)}|k(t)\rangle - E(t)xe^{if(t)}|k(t)\rangle \tag{4.23}$$

We can solve Eq. 4.23 as following:

$$\dot{f}(t) = \left(\frac{1}{2}k^2(t) + I_p\right) \Rightarrow f(t) = -\frac{1}{2}\int_0^t k^2(t')dt' - I_p t \tag{4.24}$$

and

$$|\dot{k}(t)\rangle = iE(t)x|k(t)\rangle \Rightarrow |k(t)\rangle = c_1 e^{i\int_0^t E(t')xdt'} \tag{4.25}$$

But since $|k(0)\rangle = |k\rangle$, $c_1 = |k\rangle$ and thus

$$v|k(t)\rangle = -i\nabla|k(t)\rangle = -i\nabla e^{i\int_0^t E(t')xdt'}|k\rangle$$

$$= -i^2\int_0^t E(t')dt'\frac{dx}{dx}e^{i\int_0^t E(t')xdt'}|k\rangle - i\nabla e^{i\int_0^t E(t')xdt'}|k\rangle$$

$$= \int_0^t E(t')dt'e^{i\int_0^t E(t')xdt'}|k\rangle + ke^{i\int_0^t E(t')xdt'}|k\rangle = \left(k + \int_0^t E(t')dt'\right)e^{i\int_0^t E(t')xdt'}|k\rangle$$

$$= \left(k + \int_0^t E(t')dt'\right)|k + \int_0^t E(t')dt'\rangle = k(t)|k(t)\rangle \tag{4.26}$$

The homogeneous Volkov solution is

$$|\phi_V(t)\rangle = e^{-\frac{i}{2}\int_0^t (k-A(t')+A(0))^2dt' - iI_pt}|k - A(t) - A(0)\rangle \tag{4.27}$$

which can also be written in terms of a time evolution operator as

$$|\phi_V(t)\rangle = U_V(t,0)|k\rangle \tag{4.28}$$

Thus the time evolution operator of the Volkov equation in velocity representation $U_V(t,t')$ also called propagator is:

$$\langle k|U_V(t,t')|k'\rangle = \langle k|e^{-\frac{i}{2}\int_{t'}^t (k'-A(t'')+A(t'))^2 - iI_p(t-t')}|k' - A(t) + A(t')\rangle$$

$$= \delta(k - k' + A(t) - A(t'))\exp\left(-\frac{i}{2}\int_{t'}^t (k' - A(t'') + A(t'))^2dt'' - iI_p(t-t')\right) \tag{4.29}$$

The time evolution operator (i.e. the Green's function) fulfills the homogeneous Volkov Equation itself

$$i\frac{d}{dt}U_V(t,t') = H_V(t)U_V(t,t') \tag{4.30}$$

and then we can use the Green's function in order to calculate the particular solution of the inhomogeneous Volkov equation (Eq. 4.16). Thus the particular solution of the inhomogeneous Volkov equation is

$$|\phi(t)\rangle = -i \int_0^t U_V(t,t')E(t')x\alpha(t')|0\rangle dt' \tag{4.31}$$

The "-" is because in usual Physics notation the Green's function is defined with the opposite sign. Thus the Green's function is the exponential of the action.

4.3 Dipole Acceleration

We use the improved three step model (ITSM) [38] for the calculation of the dipole acceleration. Instead of calculating the dipole moment and differentiating twice in time [18], we use the Ehrenfest theorem

$$\ddot{x} = -\partial_x V(r) + E(t) \tag{4.32}$$

and thus the expectation value of the dipole acceleration is

$$\ddot{x} = \langle\psi(t)|\left(-\partial_x V(r) + E(t)\right)|\psi(t)\rangle = -\langle\psi(t)|\partial_x V(r)|\psi(t)\rangle + E(t) \tag{4.33}$$

We drop $E(t)$ since it does not include any high harmonics. So the remaining expectation value of the dipole acceleration is

$$\ddot{x}(t) = -|\alpha(t)|^2\langle 0|V'(r)|0\rangle - \alpha^*(t)\langle 0|V'(r)|\phi(t)\rangle - \alpha(t)\langle\phi(t)|V'(r)|0\rangle - \langle\phi(t)|V'(r)|\phi(t)\rangle \tag{4.34}$$

The first term vanishes due to odd symmetry and the last term describes scattering of the returning electron from the potential (free-free transitions). Thus

$$\ddot{x}(t) = \ddot{\xi}(t) + \ddot{\xi}^*(t) \tag{4.35}$$

with

$$\ddot{\xi}(t) = -\alpha^*(t)\langle 0|V'(r)|\phi(t)\rangle \tag{4.36}$$

For the derivation of the dipole acceleration we expand the particular Volkov solution $|\phi(t)\rangle$ into plane waves $|k\rangle$.

$$\langle k|\phi(t)\rangle = -i\int_0^t \langle k|U_V(t,t')E(t')x\alpha(t')|0\rangle dt' \tag{4.37}$$

We insert in Eq. 4.37 $\int\langle k'|k'\rangle dk'^3 = 1$ and thus we have

$$\langle k|\phi(t)\rangle = -i\int_0^t dt'\int dk'^3\langle k|U_V(t,t')|k'\rangle\alpha(t')E(t')\langle k'|x|0\rangle \tag{4.38}$$

Inserting Eq. 4.29, in Eq. 4.38 we get

$$\langle k|\phi(t)\rangle = -i\int_0^t dt'\int dk'^3\delta(k-k'+A(t)-A(t'))\alpha(t')E(t')\langle k'|x|0\rangle$$

$$\times\exp\left(-\frac{i}{2}\int_{t'}^t (k'-A(t'')+A(t'))^2dt'' - iI_p(t-t')\right) \tag{4.39}$$

Defining

$$p' = k' + A(t') \tag{4.40}$$

and

$$p = k + A(t) \tag{4.41}$$

we get

$$\langle p - A(t)|\phi(t)\rangle =$$

$$-i\int_0^t dt'\alpha(t')E(t')\langle p-A(t')|x|0\rangle\exp\left(-\frac{i}{2}\int_{t'}^t (p-A(t''))^2dt'' - iI_p(t-t')\right) \tag{4.42}$$

Defining the action of the free particle in the laser field

$$S(p,t,t') \equiv \frac{1}{2}\int_{t'}^{t}(p - A(t''))^2 dt'' - iI_p(t-t') \tag{4.43}$$

we conclude that

$$\langle p - A(t)|\phi(t)\rangle = -i\int_{0}^{t} dt'\alpha(t')E(t')\langle p - A(t')|x|0\rangle e^{-iS(p,t,t')} \tag{4.44}$$

where $A(t) = -\hat{x}\int_{-\infty}^{t} E(t')dt'$ is the vector potential which describes the electric field.

The standard derivation involves a three-dimensional momentum integration carried out in the stationary phase approximation and the t' integration carried out later in the saddle-point approximation. However, much insight can be gained if the t' integration is carried out first, right away in Eq. 4.44. So, instead of calculating the integral in the action term over all the birth times t', we only evaluate it at those values at which the derivative of action with respect to birth time is zero. It should be noted that taking the derivative with respect to t' is a mathematical method of implementing the Landau-Dykhne formula [39]
The equation for the saddle point is:

$$\partial_{t'}S(p,t,t') = -\frac{1}{2}(p - A(t'))^2 - I_p = 0 \tag{4.45}$$

For a sinusoidal pulse, many birth times $t' = t_n$ (where n=1,2,3,) can satisfy this condition. Eq. 4.45 has two complex solutions:

$$p_x - A_x(t') = \pm i\sqrt{2I_p + p_\perp^2} \tag{4.46}$$

where $p_\perp^2 \equiv p_y^2 + p_z^2$ is the momentum vector component squared in the y-z plane, orthogonal to the applied field. The saddle points t' need to be complex to fulfill Eq. 4.45, i.e. $t' = t'_r \pm t'_i$. Under the assumption that the imaginary part is much smaller than the period of the driving

field, i.e. $\gamma = \omega_0 t_i' \ll 1$, the vector potential can be linearized around the real part of the saddle point and we obtain

$$p_x - A_x(t_r') \pm iE(t_r')t_i' = \pm i\sqrt{2I_p + p_\perp^2} \tag{4.47}$$

Thus the real part of the saddle point, which is the birth time of an electron with canonical moment p_x, is determined by the solution of $p_x - A_x(t_r') = 0$, i.e. the particle starts with zero velocity. The imaginary part is the well known tunneling time given the field $E(t_r')$, that suppresses the potential barrier of height I_p, [40]

$$t_i' = \sqrt{2I_p + p_\perp^2}/E(t_r') \tag{4.48}$$

which holds for small Keldysh parameter $\gamma = \omega_0\sqrt{2I_p}/E(t_r')$.
We set $\theta = p_x - A_x(t')$ and rewriting Eq. 4.43 in terms of t_n and θ we have

$$S(p, t, t_n(p_x, \theta)) = \frac{1}{2}\int_{t_n(p_x,\theta)}^{t} dt''(p_x - A(t''))^2 + \theta^2(t - t_n(p_x, \theta)) \tag{4.49}$$

Next we want to expand the above integral about $t_n(p_x, \theta = 0)$. The Taylor expansion gives

$$S(p, t, t_n(p_x, \theta)) = S(p, t, t_n(p_x, \theta = 0)) + \frac{\partial S}{\partial t_n}\Delta t + \frac{1}{2}\frac{\partial^2 S}{\partial t_n^2}\Delta t^2 + \frac{1}{3!}\frac{\partial^3 S}{\partial t_n^2}\Delta t^3 + ... \tag{4.50}$$

Note that $t_n(p_x, 0)$ are the (possibly many or none) positive real solutions of Eq. 4.46. Let us look at the above equation term by term.
Zeroth order:

$$S(p, t, t_n(p_x, \theta = 0)) = \frac{1}{2}\int_{t_n(p_x,\theta=0)}^{t} dt''(p_x - A(t''))^2 \tag{4.51}$$

First order:

$$\left.\frac{\partial S}{\partial t_n}\right|_{t_n=t_n(p_x,\theta=0)} = -\frac{1}{2}(p_x - A(t_n(p_x, \theta = 0)))^2 \tag{4.52}$$

Since, $t_n(p_x, \theta = 0)$ is the saddle point for $S(p, t, t_n(p_x, \theta = 0))$, the first derivative goes to zero, as $p_x - A(t_n(p_x, \theta = 0)) = 0$

Second order:

$$\left.\frac{\partial^2 S}{\partial t_n^2}\right|_{t_n = t_n(p_x, \theta = 0)} = -\left(p_x - A(t_n(p_x, \theta = 0))\right) E(t_n, (p_x, \theta = 0)) \tag{4.53}$$

This term goes to zero for the same reason as the first order.

Third order:

$$\begin{aligned}\left.\frac{\partial^3 S}{\partial t_n^3}\right|_{t_n = t_n(p_x, \theta = 0)} &= -\left(p_x - A(t_n(p_x, \theta = 0))\right) \dot{E}(t_n, (p_x, \theta = 0)) - \left(E(t_n, (p_x, \theta = 0))\right)^2 \\ &= -\left(E(t_n, (p_x, \theta = 0))\right)^2 \end{aligned} \tag{4.54}$$

Before we go into expanding the action, let's find Δt by expanding $t_n(p_x, \theta)$ around $t_n(p_x, \theta = 0)$

$$t_n(p_x, \theta) = t_n(p_x, \theta = 0) + \frac{\partial t_n}{\partial \theta}\theta + \frac{1}{2}\frac{\partial^2 t_n}{\partial \theta^2}\theta^2 + \frac{1}{3!}\frac{\partial^3 t_n}{\partial \theta^3}\theta^3 + ... \tag{4.55}$$

and thus

$$\begin{aligned}\Delta t = t_n(p_x, \theta) - t_n(p_x, \theta = 0) &= \frac{\partial t_n}{\partial \theta}\theta + \frac{1}{2}\frac{\partial^2 t_n}{\partial \theta^2}\theta^2 + \frac{1}{3!}\frac{\partial^3 t_n}{\partial \theta^3}\theta^3 + ... \\ &= \frac{1}{E(t_n(p_x, \theta = 0))}\theta - \frac{1}{2}\frac{\dot{E}(t_n(p_x, \theta = 0))}{E^3(t_n(p_x, \theta = 0))}\theta^2 \end{aligned} \tag{4.56}$$

By taking only the first order term for Δt and inserting it in the expansion of the action Eq. 4.50 we get:

$$S(p, t, t_n(p_x, \theta)) = S(p, t, t_n(p_x, \theta = 0)) - \frac{i}{3E(t_n(p_x, \theta = 0))}\theta^3 \tag{4.57}$$

Eq. 4.57 is the expansion for the action around $t_n(p_x, 0)$.

We expand the action in Eq. 4.44 around $t_n(p_x,\theta)$ up to 2^{nd} order. The first derivative of the action at the saddle point $t_n(p_x,\theta)$ is zero. Thus

$$\langle p - A(t)|\phi(t)\rangle =$$

$$-i\int_0^t dt'\alpha(t_n(p_x,\theta))E(t_n(p_x,\theta))\langle p - A(t_n(p_x,\theta))|x|0\rangle e^{-i\left(S(p,t,t_n(p_x,\theta))+\frac{1}{2}\frac{\partial^2 S}{\partial t'^2}\Big|_{t'=t_n(p_x,\theta)}(t'-t_n(p_x,\theta)\right)}$$

$$= -i\alpha(t_n(p_x))\int_0^t dt' E(t_n(p_x,\theta))\langle p - A(t_n(p_x,\theta))|x|0\rangle e^{-i\left(S(p,t,t_n(p_x,\theta))+\frac{1}{2}\frac{\partial^2 S}{\partial t'^2}\Big|_{t'=t_n(p_x,\theta)}(t'-t_n(p_x,\theta)\right)} \tag{4.58}$$

In Eq. 4.58 we substitute $S(p,t,t_n(p_x,\theta))$ with its expansion around $t_n(p_x,0)$, i.e. Eq. 4.57. At the saddle point $\theta = \pm i\sqrt{2I_p + p_\perp^2}$ and then

$$\langle p - A(t)|\phi(t)\rangle =$$

$$= -i\alpha(t_n(p_x))\int_0^t dt' E(t_n(p_x,\theta))\langle p - A(t_n(p_x,\theta))|x|0\rangle e^{-iS(p,t,t_n(p_x))}e^{-\frac{(2I_p+p_\perp^2)^{3/2}}{3|E|}}$$

$$\times e^{-i\frac{1}{2}\frac{\partial^2 S}{\partial t'^2}\Big|_{t'=t_n(p_x,\theta)}(t'-t_n(p_x,\theta))^2} \tag{4.59}$$

For hydrogen-like 1s wavefunctions we have

$$\langle \nu|x|0\rangle = -i\frac{8\sqrt{2}(2I_p)^{5/4}}{\pi}\frac{\nu_x}{(2I_p+|v|^2)^3} \tag{4.60}$$

Since $\nu = p - A_x(t)$ and $\theta = \pm i\sqrt{2I_p + p_\perp^2}$ at the saddle point, we have $|\nu|^2 = (p_x - A_x(t))^2 + p_\perp^2$ and then $2I_p + |\nu|^2 = 2I_p + p_\perp^2 + \theta^2$. So

$$\langle p - A(t_n(p_x,\theta))|x|0\rangle = -i\frac{2^{7/2}(2I_p)^{5/4}}{\pi}\frac{\theta}{(2I_p+p_\perp^2+\theta^2)^3} \tag{4.61}$$

We have set $\theta = p_x - A_x(t')$, which is proportional to set $\theta = Et'$ and thus $d\theta = dt'E(t_n(p_x,\theta))$. We calculate Eq. 4.59 at the saddle points, thus the integral becomes a sum,

since we sum over all the saddle points and that's why θ varies from -∞ to ∞.

$$\langle p - A(t)|\phi(t)\rangle =$$

$$\sum_n -\alpha(t_n(p_x))e^{-iS(p,t,t_n(p_x))}\frac{2^{7/2}(2I_p)^{5/4}}{\pi}e^{-\frac{(2I_p+p_\perp^2)^{3/2}}{3|E|}}\int_{-\infty}^{\infty}d\theta\frac{\theta}{(2I_p+p_\perp^2+\theta^2)^3}$$

$$\times\, e^{-i\frac{1}{2}\frac{\partial^2 S}{\partial t'^2}\Big|_{t'=t_n(p_x,\theta)}(t'-t_n(p_x,\theta))^2} \tag{4.62}$$

From Eq. 4.53 and since at the saddle point $p_x - A_x(t_n(p_x,\theta)) = i\sqrt{2I_p+p_\perp^2} = i\tilde{p}$ we get

$$\left.\frac{\partial^2 S}{\partial t'^2}\right|_{t'=t_n(p_x,\theta)} = -i\tilde{p}E(t_n(p_x,\theta)) \tag{4.63}$$

So

$$\begin{aligned}-i\frac{1}{2}\left.\frac{\partial^2 S}{\partial t'^2}\right|_{t'=t_n(p_x,\theta)}(t'-t_n(p_x,\theta))^2 &= -\frac{\tilde{p}}{2}E(t_n(p_x,\theta))(t'-t_n(p_x,\theta))^2\\ &= -\frac{\tilde{p}}{2E}E^2(t'-t_n(p_x,\theta))^2\end{aligned} \tag{4.64}$$

and since at the saddle point (and only there) $\theta = \pm i\sqrt{1+p_\perp^2}$, thus

$$-\frac{\tilde{p}}{2E}E^2(t'-t_n(p_x,\theta))^2 = -\frac{\tilde{p}}{2E}(\theta - i\sqrt{2I_p+p_\perp^2}) \tag{4.65}$$

and we get

$$\langle p - A(t)|\phi(t)\rangle = \sum_n \alpha(t_n(p_x))e^{-iS(p,t,t_n(p_x))}f(E(t_n),p_\perp) \tag{4.66}$$

where

$$f(E(t_n),p_\perp) = -\frac{2^{7/2}(2I_p)^{5/4}}{\pi}e^{-\frac{(2I_p+p_\perp^2)^{3/2}}{3|E|}}\int_{-\infty}^{\infty}d\theta\frac{\theta\exp\left(-\frac{\tilde{p}}{2E}(\theta - i\sqrt{2I_p+p_\perp^2})^2\right)}{(2I_p+p_\perp^2+\theta^2)^3} \tag{4.67}$$

We need now to calculate the integral

$$\int_{-\infty}^{\infty} d\theta \frac{\theta \exp\left(-\frac{\tilde{p}}{2E}(\theta - i\sqrt{2I_p + p_\perp^2})^2\right)}{(2I_p + p_\perp^2 + \theta^2)^3} = \int_{-\infty}^{\infty} d\theta \frac{\theta \exp\left(-\frac{\tilde{p}}{2E}(\theta - i\sqrt{2I_p + p_\perp^2})^2\right)}{\left(\theta - i\sqrt{2I_p + p_\perp^2}\right)^3 \left(\theta + i\sqrt{2I_p + p_\perp^2}\right)^3} \tag{4.68}$$

By using the Residue method the integral is equal to

$$2\pi i \frac{1}{2!}\frac{d^2}{d\theta^2} \left. \frac{\theta \exp\left(-\frac{\tilde{p}}{2E}(\theta - i\sqrt{2I_p + p_\perp^2})^2\right)}{\left(\theta + i\sqrt{2I_p + p_\perp^2}\right)^3} \right|_{\theta = i\sqrt{1+p_\perp^2}} = \pi i \frac{\tilde{p}}{2E} \frac{1}{4(2I_p + p_\perp^2)} \tag{4.69}$$

$$= \pi i \frac{\tilde{p}}{2E} \frac{1}{4\tilde{p}^2} = \pi i \frac{1}{8E\tilde{p}}$$

Thus,

$$f(E(t_n), p_\perp) = -\frac{2^{7/2}(2I_p)^{5/4}}{\pi} \left(\pi i \frac{1}{8E\tilde{p}}\right) e^{-\frac{\tilde{p}^3}{3|E|}} \frac{1}{\sqrt{(2)}E\tilde{p}} = -i(2I_p)^{5/4} e^{-\frac{\tilde{p}^3}{3|E|}} \frac{1}{\sqrt{2}E\tilde{p}} \tag{4.70}$$

is the static ionization amplitude into a state with transverse momentum $p_\perp$, and $t_n(p_x)$ are the (possibly many or none) positive solutions of the real part of Eq. 4.46.
Inserting a momentum space completeness before $|\phi(t)\rangle$ in Eq. 4.36 and using Eq. 4.66 we construct the expression for the dipole acceleration $\ddot{\xi}$,

$$\begin{aligned} \ddot{\xi} &= -\alpha^*(t)\langle 0|V'(r)|\phi(t)\rangle = -\alpha^*(t) \int d^3p \langle 0|V'(r)|p - A(t)\rangle \langle p - A(t)|\phi(t)\rangle \\ &= -i\alpha^*(t) \sum_n \alpha(t_n(p_x)) \int d^3p \langle 0|V'(r)|p - A(t)\rangle f(E(t_n), p_\perp) e^{-iS(p,t,t_n(p_x))} \end{aligned} \tag{4.71}$$

where we have taken the imaginary unit i outside of $f(E, p_\perp)$ but we kept the minus sign.

The dipole acceleration at time t is now expressed as a sum over all possible trajectories arriving at time t, indexed by their possible birth times $t_n(p_x)$ and canonical momentum p at arrival. The integration over momentum p can again be carried out using the stationary phase approximation, which describes the impact of quantum diffusion on the dipole acceleration.

We expand $S(p,t,t')$ to second order around the stationary phase point $\bar{p}$, which is given from $\nabla_p S(p,t,t') = 0$. Thus

$$S(p,t,t') = S(\bar{p},t,t') + \nabla_p^2 S(\bar{p},t,t')\frac{(p-\bar{p})^2}{2} \tag{4.72}$$

with $\nabla_p^2 S(\bar{p},t,t') = t - t'$ and

$$S(p,t,t') = S(\bar{p},t,t') + (t-t')\frac{(p-\bar{p})^2}{2} \tag{4.73}$$

leads to

$$\ddot{\xi} = e^{3i\pi/4}\alpha^*(t)\sum_n \left(\frac{2\pi}{t - t_n(p_x)}\right)^{3/2} \alpha(t_n(p_x))\langle 0|V'(r)|\bar{p} - A(t)\rangle f(E(t_n), p_\perp) e^{-iS(\bar{p},t,t_n(p_x))} \tag{4.74}$$

We now want to express $f(E,p_\perp)$ in terms of the static ionization rate $w(E)$. Eq. 4.66 is the ionized part of the wavefunction projected on a plane wave. In order to obtain the static ionization rate, we consider the case of constant field $E = E_0$. We assume that $\alpha(t) = 1$, which means that the ground state population is kept constant. In order to find the ionization rate, we need to perform a three-dimensional momentum integration on the square modulus of Eq. 4.72. For a constant field there is only one n at most in Eq. 4.72. So $A_x = -E_0 t$ and then

$$p_x + E_0 t' = 0 \Rightarrow t' = -\frac{p_x}{E_0} \tag{4.75}$$

is the only saddle point and

$$\int d^3p |\langle p - A(t)|\phi(t)\rangle|^2 = \int d^3p |f|^2 = \int dp_x dp_y dp_z |f|^2 \tag{4.76}$$

We have

$$p_x = \nu_x + A_x(t) = -E_0 T \tag{4.77}$$

since $\nu_x = 0$ (assuming zero velocity at liberation). Since f does not depend on p_x (i.e. $f(E(t_n), p_\perp) = -i(2I_p)^{5/4} e^{-\frac{\tilde{p}^3}{3|E|}} \frac{1}{\sqrt{2E\tilde{p}}}$, $\tilde{p} = \sqrt{2I_p + p_\perp^2}$), the integration over dp_x gives $-E_0 T$.

Performing the integration over $dp_y dp_z$ we get

$$\int dp_y dp_z |f|^2 = \frac{(2I_p)^{10/4}}{2|E|^2} \int dp_y dp_z \frac{e^{-\frac{2(2I_p+p_\perp^2)^{3/2}}{3|E|}}}{(2I_p+p_\perp^2)} = \frac{(2I_p)^{10/4}}{2|E|^2} \int dp_y dp_z \frac{e^{-\frac{2}{3|E|}(2I_p)^{3/2}\left(1+\frac{p_\perp^2}{2I_p}\right)^{3/2}}}{(2I_p+p_\perp^2)} \tag{4.78}$$

Assuming that $p_\perp \approx 0$ the integral can be calculated

$$\begin{aligned}
\int dp_y dp_z |f|^2 &= \frac{(2I_p)^{6/4}}{2|E|^2} \int dp_y dp_z e^{-\frac{2}{3|E|}(2I_p)^{3/2}\left(1+\frac{3}{2}\frac{p_\perp^2}{2I_p}\right)} \\
&= \frac{(2I_p)^{6/4}}{2|E|^2} e^{-\frac{2}{3|E|}(2I_p)^{3/2}} \int dp_y dp_z e^{-\frac{(2I_p)^{3/2}}{|E|}\frac{p_\perp^2}{2I_p}} \\
&= \frac{(2I_p)^{6/4}}{2|E|^2} e^{-\frac{2}{3|E|}(2I_p)^{3/2}} \left(\sqrt{\frac{\pi|E|}{\sqrt{2I_p}}}\right)^2 \\
&= \frac{2I_p}{|E|} e^{-\frac{2}{3|E|}(2I_p)^{3/2}} \frac{\pi}{2}
\end{aligned} \tag{4.79}$$

Since the integration over dp_x gives $-E_0 T$

$$\int d^3p |f|^2 = T(2I_p) e^{-\frac{2}{3|E|}(2I_p)^{3/2}} \frac{\pi}{2} \tag{4.80}$$

The static ionization rate is defined as

$$w(E) = \frac{\int d^3p |f|^2}{T} \tag{4.81}$$

Thus

$$w(E) = (2I_p) e^{-\frac{2}{3|E|}(2I_p)^{3/2}} \frac{\pi}{2} \tag{4.82}$$

Since

$$f(E,0) = -\frac{(2I_p)^{3/4}}{\sqrt{2}|E|} e^{-\frac{(2I_p)^{3/2}}{3|E|}} \tag{4.83}$$

we can express $f(E,0)$ in terms of the static ionization rate $w(E)$ [38, 41]

$$f(E,0) = -\frac{(2I_p)^{1/4}}{|E|} \frac{\sqrt{w(E)}}{\sqrt{\pi}} \tag{4.84}$$

and the expression for the dipole acceleration is [38]

$$\ddot{\xi}(t) = -2^{\frac{3}{2}}\pi(2I_p)^{\frac{1}{4}}e^{\frac{3i\pi}{4}}\sum_n \frac{\alpha(t_{nb}(t))\alpha(t)\sqrt{w(E(t_{nb}(t)))}}{E(t_{nb}(t))(t-t_{nb}(t))^{\frac{3}{2}}}\alpha_{rec}e^{-i\bar{S}_n(t)} \tag{4.85}$$

where $\alpha_{rec} = \langle 0|V'(r)|\bar{p} - A(t)\rangle$ is the recombination amplitude [42] and t_{nb} is the birth time of an electron that returns to the origin at time t and n denotes the classical trajectory (Figure 4-1). Note, that we have set $S(p,t,t_n(p_x)) \equiv S_n(t)$.

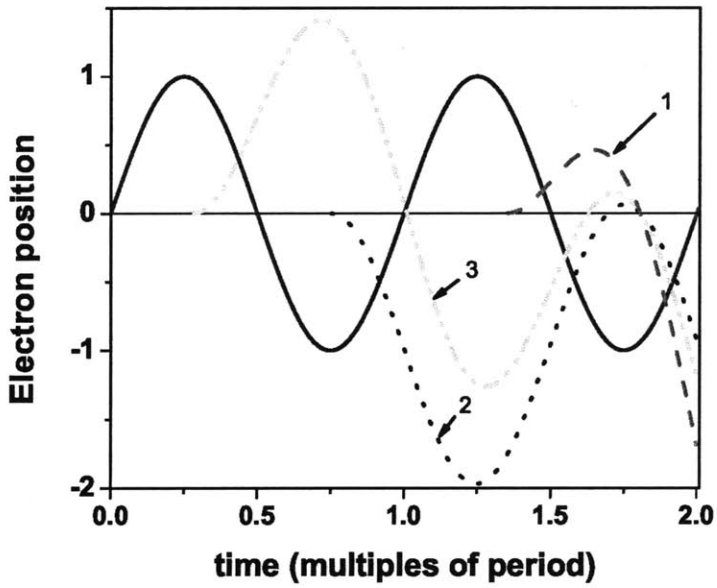

Figure 4-1: The solid line shows the driving electric field. The dotted, dash-dotted and dashed lines show electron trajectories (n) with the same arrival time, but different birth times in different half-cycles.

As an example, three trajectories, that arrive at the same time instant, but are born at different times, are shown in Figure 4-1. Each label corresponds to the birth time of each trajectory. The trajectory labeled with 1, whose birth time is closest to the arrival time, travels the shortest distance and thus has the smallest quantum diffusion, while the other two, labeled with 2 and 3, travel longer and therefore quantum diffusion reduces their contribution to the single atom response. Thus in Eq. 4.85, we will include only the trajectory with label

1, since the other two, and earlier ones, contribute considerably less, due to the increased quantum diffusion.

Chapter 5

High Harmonic Generation Efficiency

In this Chapter we derive an analytical expression for the calculation of the efficiency at a given odd harmonic in the plateau and cutoff region. The efficiency formula is based in the 1-D model and takes the laser and material parameters and macroscopic effects into account. The main result of this Chapter is that the efficiency per given harmonic scales with ω_0^6 in the plateau and with ω_0^5 in the cutoff region of the spectrum, where ω_0 is the driving frequency.

5.1 Definition

Of interest is the conversion efficiency for driver pulse energy into a given (odd) harmonic of ω_0 (Figure 5-1), whose frequency is denoted by Ω, and which is given by

$$\eta = \frac{\int_{\Omega-\omega_0}^{\Omega+\omega_0} |\tilde{E}_h(\omega)|^2 d\omega}{\int_0^{\infty} |\tilde{E}(\omega)|^2 d\omega} \tag{5.1}$$

where $\tilde{E}(\omega) \equiv \frac{1}{\sqrt{2\pi}} \int_0^T E(t) e^{i\omega t} dt$ is the Fourier transform of the driving field.

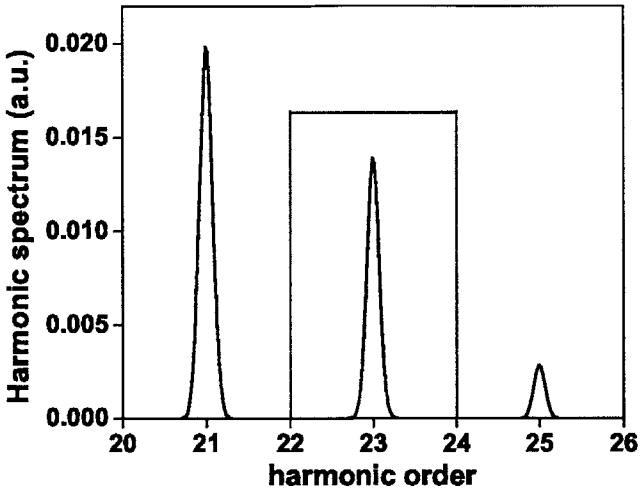

Figure 5-1: Definition of the efficiency of an odd harmonic. The blue line is the harmonic field and inside the red box are the limits of the odd harmonic, over which we integrate the harmonic field. These limits are the even harmonics before and after the odd harmonic.

The driving field is assumed to be a top-hat pulse (Figure 5-2), defined as

$$E(t) = \begin{cases} E_0 sin(\omega_0 t) & ,0 < t < T \\ 0 & \text{, elsewhere} \end{cases} \tag{5.2}$$

The denominator of Eq. 5.1 is the energy of the driving field. We calculate it using the Parseval theorem.

$$\int_{-\infty}^{\infty} |\tilde{E}(\omega)|^2 d\omega = E_0^2 N\pi/\omega_0 \tag{5.3}$$

To evaluate the numerator in Eq. 5.1, we express the harmonic field in terms of the dipole moment acceleration, using

$$\tilde{v}(\omega) \equiv \frac{1}{\sqrt{2\pi}i\omega} \int_0^T \ddot{\xi}(t) e^{i\omega t} dt \tag{5.4}$$

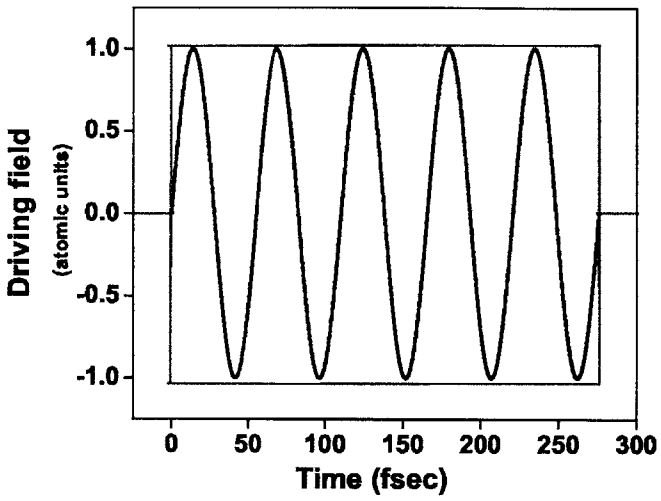

Figure 5-2: Top hat pulse.

and, substituting it into Eq. 3.12, we obtain

$$\tilde{E}_h(\omega) = -\frac{4\pi\alpha}{\sqrt{2\pi}i\omega\sigma(\omega)} g\left(\Delta k, L\right) \int_0^T \ddot{\xi}(t) e^{i\omega t} dt \tag{5.5}$$

In the quasistatic approximation, we can express the ground state probability by the quasistatic ionization rate, which has a half-cycle symmetry in the field of the top hat pulse

$$\left|\alpha\left(t+\frac{\pi}{\omega_0}\right)\right|^2 = \exp\left[-\int_0^t w(E(t'))dt'\right] \exp\left[-\int_0^{\frac{\pi}{\omega_0}} w(E(t'))dt'\right]$$

$$\Rightarrow \left|\alpha\left(t+\frac{\pi}{\omega_0}\right)\right|^2 = \left|\alpha\left(t\right)\right|^2 \beta \tag{5.6}$$

where

$$\beta = \left|\alpha\left(\frac{\pi}{\omega_0}\right)\right|^2 = \exp\left[-\int_0^{\frac{\pi}{\omega_0}} w(E(t'))dt'\right] \tag{5.7}$$

is the depletion factor of the ground state amplitude during each half-cycle.

The ground state population is assumed to be constant during each half-cycle, which is an excellent approximation, since the ionization level, and as a result the ground state population, of each half-cycle changes significantly only at the maxima of the absolute value of the electric field and stays constant during the interval, where a significant dipole radiation is generated (Figure 5-3).

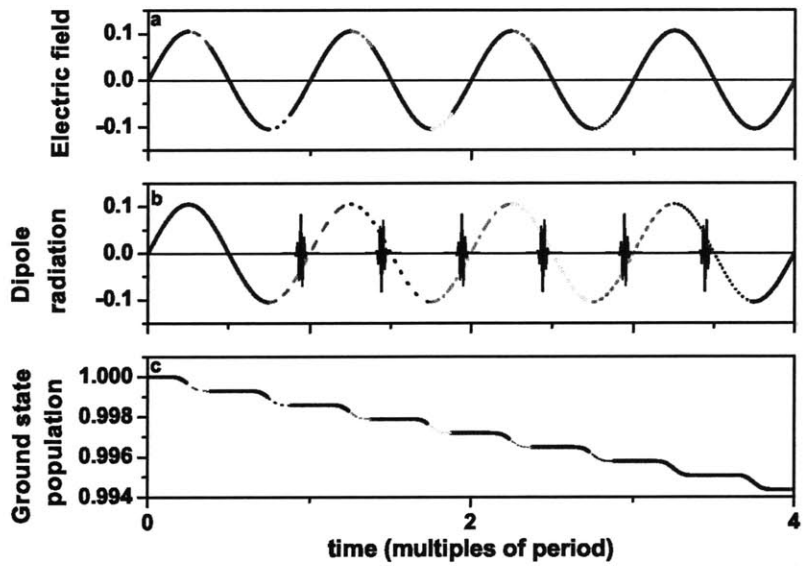

Figure 5-3: a) Driving field and periods of significant ionization, where launched trajectories may return to the core atom, shown as dashed lines, b) driving field with corresponding recombination events shown in dashed lines and attosecond bursts, c) ground state population as a function of time indicating periods of strong ionization by dashed lines.

To calculate the Fourier transform of the harmonic radiation field (Eq. 5.5) we need to calculate the integral of the dipole acceleration. We can calculate this integral numerically, but we will try to reduce the computational complexity and calculate it analytically, exploiting the symmetry of the EUV pulses that are generated at different half cycles (Figure 5-4).

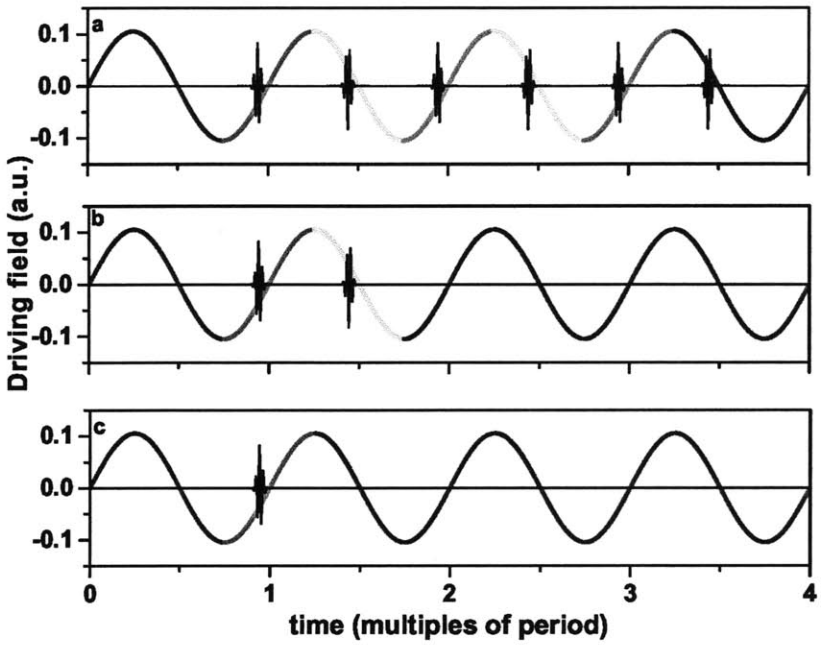

Figure 5-4: a) Calculation of Fourier transform of dipole acceleration over the whole time interval over which EUV pulses are generated, b) calculation for the 1st cycle over which EUV pulses are generated, using the fact that the dipole acceleration between EUV pulses generated at different cycles are related with the depletion factor β^2, c) calculation of Fourier transform of dipole acceleration only at the 1st half cycle where an EUV pulse is generated, using the the fact that the dipole acceleration between EUV pulses generated at different cycles are related with the depletion factor $-\beta$.

The Fourier transform of the harmonic radiation field $E_h(t)$ is

$$\tilde{E}_h(\omega) = \frac{1}{\sqrt{2\pi}} \int_0^{\frac{2\pi}{\omega_0}(N-1)} E_h(t) e^{-i\omega t} dt =$$

$$= -\frac{4\pi\alpha}{\sqrt{2\pi} i\omega\sigma(\omega)} \sum_{n=0}^{N-2} \left(g(\Delta k_{2n+1}, L) \int_{\frac{2\pi}{\omega_0}n}^{\frac{2\pi}{\omega_0}(n+\frac{1}{2})} \ddot{\xi}(t) e^{-i\omega t} dt + g(\Delta k_{2n+2}, L) \int_{\frac{2\pi}{\omega_0}(n+\frac{1}{2})}^{\frac{2\pi}{\omega_0}(n+1)} \ddot{\xi}(t) e^{-i\omega t} dt \right) \tag{5.8}$$

where n denotes the full cycle. The choice of the integration interval comes from the fact that high order harmonics are only produced after the first three quarters of a cycle of the driver pulse and we neglect the last quarter of the last cycle for simplicity, (see Figure 5-3.b). Thus the integration is only over $N-1$ full cycles. The Fourier transform is carried out by using the periodicity of the driver pulse and trajectories in each half-cycle and factoring in the different half-cycle ionization levels. As said before, the ionization level is constant during each half cycle and as a result the macroscopic response in each half cycle is independent of time and can be taken out of the integral. We first consider the case of perfect phase matching and absorption limited conditions, where the sum over half-cycles can be carried out analytically.

5.2 HHG Efficiency under Absorption-limited Conditions

If we assume perfect phase matching over the whole spectrum and absorption limited conditions, then $|g(\Delta k, L)|^2 = 1$, and we obtain:

$$\tilde{E}_h(\omega) = -\frac{4\pi\alpha}{\sqrt{2\pi}i\omega\sigma(\omega)} \int_0^{\frac{2\pi}{\omega_0}} \ddot{\xi}(t) e^{-i\omega t} dt \sum_{n=0}^{N-2} \beta^{2n} e^{-i\omega n \frac{2\pi}{\omega_0}} \tag{5.9}$$

Thus, the contribution of each half cycle is proportional to the exponentially decaying ground state population at the time of birth and recombination of the trajectory. We then integrate the square modulus of the above expression over a frequency range associated with one (odd) harmonic and finally obtain, an expression for the efficiency defined in Eq. 5.1,

$$\eta = \frac{2^5\omega_0^2\alpha^2}{E_0^2\Omega^2\sigma^2(\Omega)} \cdot \frac{1-\beta^{4(N-1)}}{(1-\beta^4)N} \cdot \left|1+\beta e^{i\pi\left(1-\frac{\Omega}{\omega_0}\right)}\right|^2 B(\Omega) \tag{5.10}$$

where

$$B(\Omega) = \left| \int_{\frac{3\pi}{2\omega_0}}^{\frac{5\pi}{2\omega_0}} \ddot{\xi}(t) e^{i\Omega t} dt \right|^2 \tag{5.11}$$

is the Fourier transform of the dipole acceleration over the first half-cycle of recombination events that contribute to the harmonic field. The magnitude square in Eq. 5.10 describes the interference of harmonics emitted in two subsequent half-cycles and the prefactor describes the sum over the $N-1$ contributing cycles.

5.3 HHG Efficiency including Phase-Mismatch

In general, it is difficult, if not impossible, to achieve phase matching over the whole harmonic spectrum. The ionization level and hence the phase mismatch associated with the plasma is different for each half-cycle and thus the term $|g(\Delta k, L)|$ (given in Eq. 3.13) varies for each half-cycle and this variation has to be accounted for in the harmonic spectrum,

$$\begin{aligned} \tilde{E}_h(\omega) = -\frac{4\pi\alpha}{\sqrt{2\pi} i\omega\sigma(\omega)} \sum_{n=0}^{N-2} \left(g(\Delta k_{2n+1}, L) + \beta e^{i\pi\left(1-\frac{\omega}{\omega_0}\right)} g(\Delta k_{2n+2}, L) \right) \\ \times \beta^{2n} e^{-i\omega n \frac{2\pi}{\omega_0}} \int_0^{\frac{\pi}{\omega_0}} \ddot{\xi}(t) e^{-i\omega t} dt \end{aligned} \tag{5.12}$$

The expression accounts for the different phase mismatch, Δk_n, in each half cycle. It is assumed to be constant during each half-cycle, since the ionization level stays constant for the time interval where significant dipole radiation is generated, as explained before (see Figure 5-3). The bracket in Eq. 5.12 accounts for the second half-cycle with its opposite sign and reduced ground-state population.

Following the same steps as in the case of perfect phase matching and assuming that the polarizability, which appears in Δk_n, varies slowly over the bandwidth of one harmonic, we

obtain

$$\eta = \frac{2^5\omega_0^2\alpha^2}{E_0^2\Omega^2\sigma^2(\Omega)} \cdot \frac{1}{N} \cdot B(\Omega) \cdot \sum_{n=0}^{N-2} \beta^{4n} \left| g(\Delta k_{2n+1}, L) + \beta e^{i\pi\left(1-\frac{\Omega}{\omega_0}\right)} g(\Delta k_{2n+2}, L) \right|^2 \tag{5.13}$$

5.4 Dipole Acceleration Spectrum

The dipole acceleration spectrum $B(\Omega)$ of the first half-cycle of recombination events, Eq. 5.13, can either be calculated numerically by computing the dipole acceleration for each classical trajectory, or by using the stationary phase method which enables us to get closed formulas for the efficiency

$$B(\Omega) = \int_{\frac{3\pi}{2\omega_0}}^{\frac{5\pi}{2\omega_0}} \ddot{\xi}(t) e^{-i\Omega t} dt = 2^{\frac{3}{2}}\pi(2I_p)^{\frac{1}{4}} e^{\frac{3i\pi}{4}} \sum_n \int_{\frac{3\pi}{2\omega_0}}^{\frac{5\pi}{2\omega_0}} \frac{\alpha(t_{nb})\alpha(t)\sqrt{w(E(t_{nb}))}}{E(t_{nb})(t-t_{nb})^{\frac{3}{2}}} \alpha_{rec} e^{-i(S_n(t)-\Omega t)} dt \tag{5.14}$$

The phase $\phi_n(t) = S_n(t) - \Omega t$, which contains the classical action, varies much faster than the other factors in the integral (Figure 5-5). Therefore, the major contribution to the integral comes from the stationary points of the phase. These points are the time instants at which the derivative of the phase is zero (stationary phase) $\partial_t \phi_n(t) = 0 \Rightarrow \partial_t S_n(t) = \Omega_n$. The two stationary points are clearly visible in Figure 5-5.

From Figure 5-5 we see that the curvature of the phase for the short and long trajectory is smaller and larger, respectively, which leads to a larger contribution of the short trajectory compared to the long one, as a result of its smaller quantum diffusion.

In the stationary phase approximation, the slowly varying terms $\frac{\alpha(t_{nb})\alpha(t)\sqrt{w(E(t_{nb}))}}{E(t_{nb})(t-t_{nb})^{\frac{3}{2}}}$ can be moved out of the integral and evaluated at the time of stationary phase, implying the transition energy of the recolliding electron has to be equal to Ω. This condition is fulfilled twice during each half-cycle and is referred to as short and long trajectories (Figure 5-6).

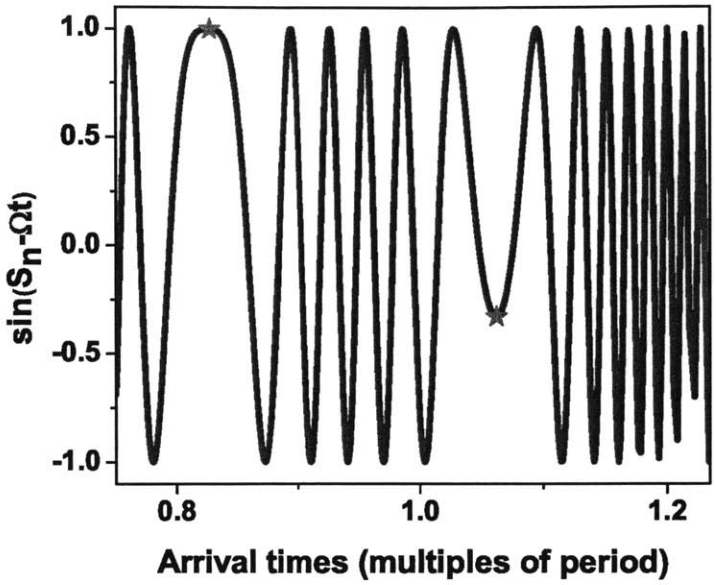

Figure 5-5: Oscillation of the phase as a function of arrival times. We denote the saddle points with the *.

In the stationary phase approximation, the action is expanded up to 2nd order

$$S_n(t) = \bar{S}_n + \Omega_n \cdot (t - ta_n) + \partial_t^2 S_n \frac{(t - ta_n)^2}{2} \tag{5.15}$$

where ta_n is the arrival time of each trajectory and $\bar{S}_n = S(ta_n, tb_n)$ the action of the classical electron trajectory. Figure 5-7 compares the second order approximation with the exact action according to Eq. 5.15.

For a particular harmonic of the plateau region both short and long trajectories contribute and the term $D(\Omega) = \int_{3\pi/2\omega_0}^{5\pi/2\omega_0} e^{-i(S_n(t)-\Omega t)}$ can be written as $D(\Omega) = D_s(\Omega) + D_l(\Omega)$, where s stands for short trajectory and l for long trajectory. We obtain

$$D_{s/l}(\Omega) = \int_{\frac{3\pi}{2\omega_0}}^{\frac{5\pi}{2\omega_0}} e^{-i(\bar{S}_n - \Omega t_{na} + \frac{1}{2}\partial_t^2 \bar{S}_n (t-t_{na})^2)} dt = e^{-i(\bar{S}_n - \Omega t_{na})} \int_{\frac{3\pi}{2\omega_0}}^{\frac{5\pi}{2\omega_0}} e^{-\frac{\partial_t^2 \bar{S}_n}{2}(t-t_{na})^2} dt \tag{5.16}$$

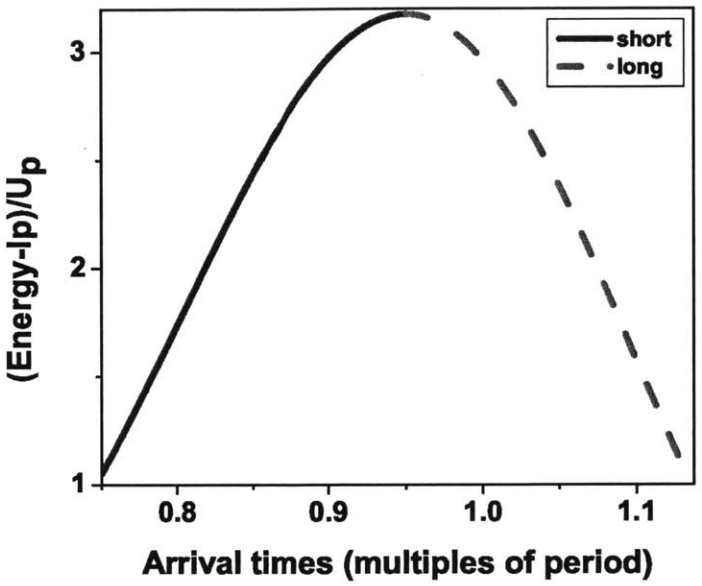

Figure 5-6: First derivative of the action as a function of arrival times.

where n stands for either long or short trajectory contributing to that particular harmonic. The result is

$$D_{s/l}(\Omega) = e^{-i(\bar{S}_n - \Omega t_{na})} \frac{1-i}{2} \sqrt{\frac{\pi}{\partial_t^2 \bar{S}_n}} \times \left(Erf\left(\frac{i+1}{2} \sqrt{\partial_t^2 \bar{S}_n} \left(\frac{5\pi}{2\omega_0} - t_{na} \right) \right) - Erf\left(\frac{i+1}{2} \sqrt{\partial_t^2 \bar{S}_n} \left(\frac{3\pi}{2\omega_0} - t_{na} \right) \right) \right) \tag{5.17}$$

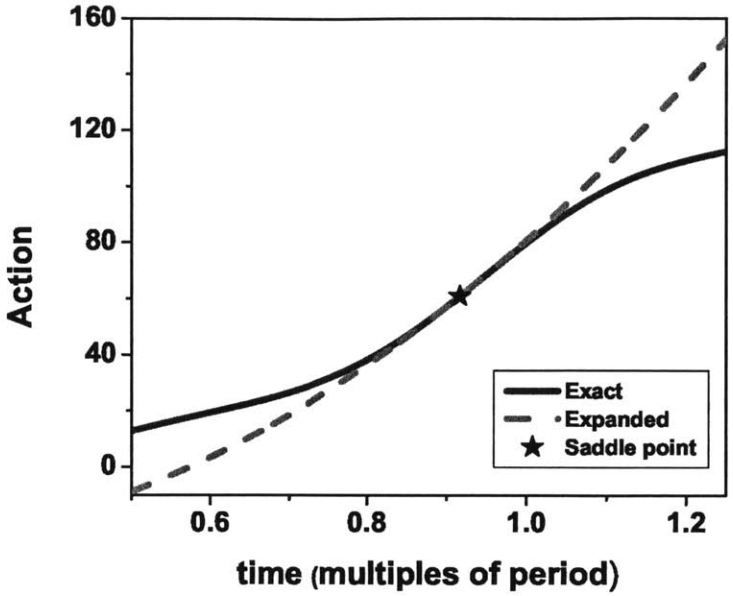

Figure 5-7: Classical action calculated from the analytical formula (Eq. 4.43) and the second order expansion (Eq. 5.15).

where Erf is the error function and, therefore,

$$\int_{\frac{3\pi}{2\omega_0}}^{\frac{5\pi}{2\omega_0}} \ddot{\xi}(t)e^{-i\Omega t}dt = 2^{\frac{3}{2}}\pi(2I_p)^{\frac{1}{4}}e^{\frac{3i\pi}{4}}$$
$$\times\left(\frac{\alpha(t_{1s})\alpha(t_{2s})\sqrt{w(E(t_{1s}))}}{E(t_{1s})(t_{2s}-t_{1s})^{\frac{3}{2}}}\alpha_{rec}(t_{2s})D_s(\Omega)+\frac{\alpha(t_{1l})\alpha(t_{2l})\sqrt{w(E(t_{1l}))}}{E(t_{1l})(t_{2l}-t_{1l})^{\frac{3}{2}}}\alpha_{rec}(t_{2l})D_l(\Omega)\right) \tag{5.18}$$

In the asymptotic limit the Error functions approach -2 and 2, for the long and short trajectory, respectively. It turns out that these asymptotic values are excellent approximations for the times of interest in Eq. 5.18. By taking into account that the second derivative of the action for the long trajectories is negative and can be written as $\partial_t^2\bar{S}_l = |\partial_t^2\bar{S}_l|e^{i\pi}$, the closed formula for the efficiency in the plateau region is [43]

$$\eta = 0.0107\frac{\sqrt{2I_p}\omega_0^5|\alpha_{rec}|^2}{E_0^4\Omega^2\sigma^2(\Omega)}\cdot\frac{1}{N}\cdot\sum_{n=0}^{N-2}\beta^{4n}\left|g(\Delta k_{2n+1},L)+\beta e^{i\pi\left(1-\frac{\Omega}{\omega_0}\right)}g(\Delta k_{2n+2},L)\right|^2\times$$
$$\left|\frac{\alpha(t_{bs})\alpha(t_{as})\sqrt{w(E(t_{bs}))}}{sin(\omega_0 t_{bs})[\omega_0(t_{as}-t_{bs})/(2\pi)]^{3/2}}\frac{e^{-i(\bar{S}_s-\Omega t_{as})}}{\sqrt{\partial_t^2 S_s|}}+\frac{\alpha(t_{bl})\alpha(t_{al})\sqrt{w(E(t_{bl}))}}{sin(\omega_0 t_{bl})[\omega_0(t_{al}-t_{bl})/(2\pi)]^{3/2}}\frac{e^{-i(\bar{S}_l-\Omega t_{al}-\frac{\pi}{2})}}{\sqrt{|\partial_t^2 S_l|}}\right|^2 \tag{5.19}$$

where, (t_{bs},t_{as}), (t_{bl},t_{al}) and $\bar{S}_{s,l}=S(t_{as,l},t_{bs,l})$ are the pairs of birth/arrival times and the corresponding classical action for short and long trajectories of a particular harmonic, respectively. Eq. 5.19 is valid for harmonic energies Ω in the plateau region, satisfying the condition $1<(\Omega-I_p)/U_p<3.1$. The upper limit allows us to expand the classical action up to second order and the lower limit is determined by the validity of using the asymptotic values for the error function used in $D_{s/l}(\Omega)$ in Eq. 5.17.

The last two terms show two interference mechanisms. The first one is the interference between each half-cycle and the second one is the interference between long and short trajectories. The first interference mechanism allows only odd harmonics under the condition $\beta\approx 1$. The symmetry can be broken by very intense pulses and in this case even harmonics can also occur.

The efficiency of a single harmonic in the plateau region scales with ω_0^6. This power law arises from a cubic dependence of the quantum diffusion on the laser cycle period, another factor of ω_0 is due to the fact that we integrate over a single harmonic and an additional factor comes from the scaling of the driving field energy with ω_0, given a fixed number of cycles and peak intensity. There is an additional dependence on ω_0 from the second derivative of the action which scales with $1/\omega_0$.

As Ω increases approaching the cutoff frequency, $\Omega_{cutoff}\equiv I_p+3.17U_p$ the two trajectories merge. At this point of degeneracy (i.e. cutoff) $\partial_t^2 S_n(t)=0$ and as a consequence an expansion of the action up to 3rd order is necessary:

$$S_n(t)=\bar{S}_n+\Omega_n\cdot(t-ta_n)+\partial_t^2 S_n\frac{(t-ta_n)^2}{2}+\partial_t^3 S_n\frac{(t-ta_n)^3}{6} \tag{5.20}$$

$B(\Omega)$ is reduced to an Airy function which can be evaluated numerically. The respective birth and arrival times are $tb_{cutoff} \approx 1.88/\omega_0$ and $t\alpha_{cutoff} \approx 5.97/\omega_0$. Thus, the efficiency at the cutoff point can be written as [43]:

$$\eta = 0.0236 \frac{\sqrt{2I_p}\omega_0^5 |\alpha_{rec}|^2}{E_0^{16/3}\Omega_{cutoff}^2 \sigma^2(\Omega_{cutoff})} \cdot \frac{1}{N} \times \sum_{n=0}^{N-2} \beta^{4n} \left| g(\Delta k_{2n+1}, L) + \beta e^{i\pi\left(1-\frac{\Omega_{cutoff}}{\omega_0}\right)} g(\Delta k_{2n+2}, L) \right|^2 \kappa_0 w[E(tb_{cutoff})] \tag{5.21}$$

where $\kappa_0 = |\alpha(tb_{cut})\alpha(ta_{cut})|^2$ accounts for the intra-cycle depletion of the ground state.

Chapter 6

Results using 1-D model

In this Chapter we compare the results of the efficiency formula derived in Chapter 5, with experimental results from the literature for 400 and 800 nm drivers and we show very good agreement. The main result is that the efficiency for 400 nm is 1-2 orders of magnitude higher than the one at 800 nm. We also study the effects that interference of long and short trajectories have on the spectra. In addition, we investigate two different ionization models, the ADK and the Yudin-Ivanov and we show that the Yudin-Ivanov model, which includes both tunneling and multiphoton ionization, gives more accurate results especially for short drive wavelengths.

6.1 Comparison of 1-D Theory with Experiments at 400 nm and 800 nm

The 1-D theory is compared with experimental results of HHG efficiency measurements, using 400 and 800 nm driver pulses on several noble gases as reported in [44]. Since Ti:sapphire lasers became a standard high-power femtosecond laser source, most HHG experiments have been performed at its emission wavelength of 800 nm [8, 15]. Typical conversion efficiencies from Ti:sapphire lasers are in the range of 10^{-6} to 10^{-8} for 50-100 eV photon energy. Many

applications in the < 100 eV range, such as EUV lithography, seeding of X-ray free electron lasers and attosecond spectroscopy require high energies or average power and therefore, HHG needs higher efficiencies. For these applications the use of shorter driving wavelength with slightly higher electric fields than that of 800 nm pulses is a favorable route towards higher HHG efficiencies, because of the scaling of the single atom response with drive wavelength, and the reduced plasma dispersion.

Figure 6-1.a shows the HHG efficiencies and spectra obtained experimentally using a 400 nm driver pulse for Argon, Neon and Helium, while Figure 6-1.b shows the corresponding simulation results. In the experiment, the peak intensity of the driver pulse measured from the peak power and spot size was $2.7 \cdot 10^{15}$ W/cm^2, with pulse energy of 1 mJ for which we observed the strongest HHG signal. However, our theory suggests that this intensity will lead to strong ionization, which will make it difficult to achieve phase matching for the EUV wavelengths. Thus, the actual intensity is estimated to be in the range of $10^{14} - 10^{15}$ W/cm^2 due to spatial effects distorting the beam, like plasma defocusing, which are not taken into account by the one-dimensional model. Actual measurements at intensities of about 10^{14} W/cm^2 show similar HHG efficiencies, as discussed in [44]. Therefore, in our simulations based on the one-dimensional model, we adjusted the laser intensity to achieve optimum phase matching conditions for the half cycle in the center of the pulse. The intensities used in our simulations are lower than in the experiment. In the experiment, peak efficiencies of $1 \cdot 10^{-4}$ at 28 eV are reached for Argon, $1 \cdot 10^{-5}$ at 34 eV for Neon, and $1 \cdot 10^{-5}$ at 53 eV for Helium, while the peak efficiencies from simulations are $6 \cdot 10^{-5}$ at 33.5 eV for Argon, $2 \cdot 10^{-5}$ at 51.7 eV for Neon, and $4 \cdot 10^{-5}$ at 66.5 eV for Helium, close to the experiments.

Figure 6-2.a and Figure 6-2.b summarize the experimental and simulation results respectively, for 800 nm drivers. As predicted by the theory, the efficiencies from the 800 nm driver are 1-2 orders of magnitude lower than that from the 400 nm driver. However, the cutoff energy is significantly increased to beyond 100 eV with Helium. In the experiment, the conversion efficiencies at the cutoff are $1 \cdot 10^{-7}$ at 45 eV for Argon, $1 \cdot 10^{-7}$ at 88 eV for Neon, and $1 \cdot 10^{-8}$ at 110 eV for Helium, while the theory predicts $1 \cdot 10^{-6}$ at 41 eV for

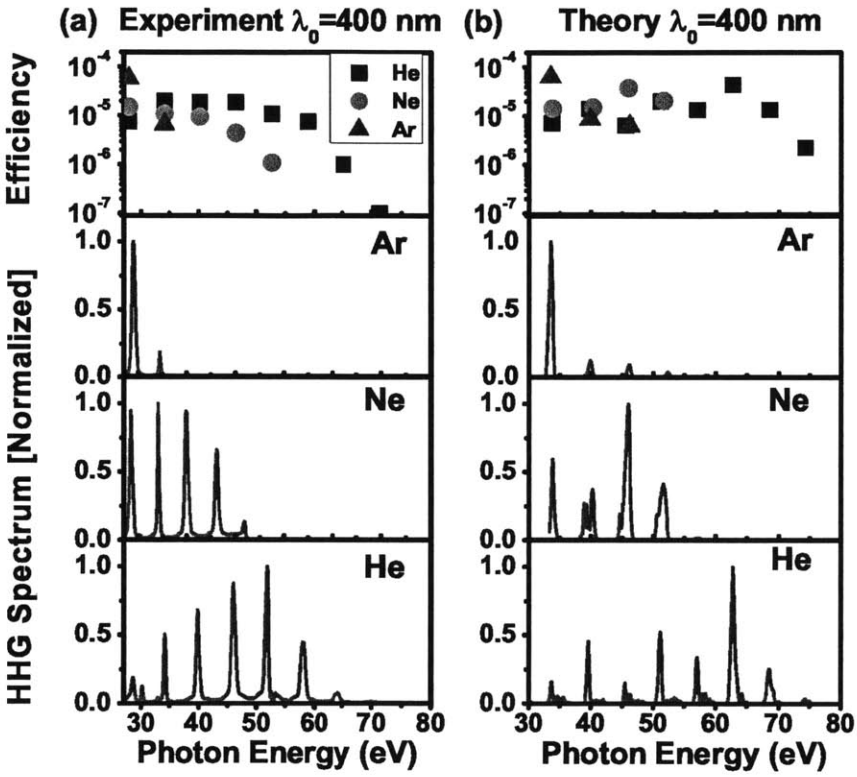

Figure 6-1: a) Experimental results for HHG driven by 400 nm, 1 mJ and 26 fsec driver pulses with beam waist 30 μm: top row, efficiencies for Argon (50 mbar), Neon (300 mbar) and Helium (2 bar) using a 2 mm long nozzle; remaining rows, the respective normalized HHG spectra [44], b) Simulation results for Argon ($2.5 \cdot 10^{14}$ W/cm^2), Neon ($5.3 \cdot 10^{14}$ W/cm^2) and Helium ($8.5 \cdot 10^{14}$ W/cm^2) for the same interaction parameters like in (a).

Argon, $1 \cdot 10^{-7}$ at 82 eV for Neon, and $1 \cdot 10^{-8}$ at 107 eV for Helium.

In our simulations, in Figures 6-1.b and 6-2.b, we observe, in addition to inter-cycle interference which leads to odd harmonics, intra-cycle interference patterns on each harmonic. We observe, that (a) theoretical HHG spectra do not show clean harmonics like their exper-

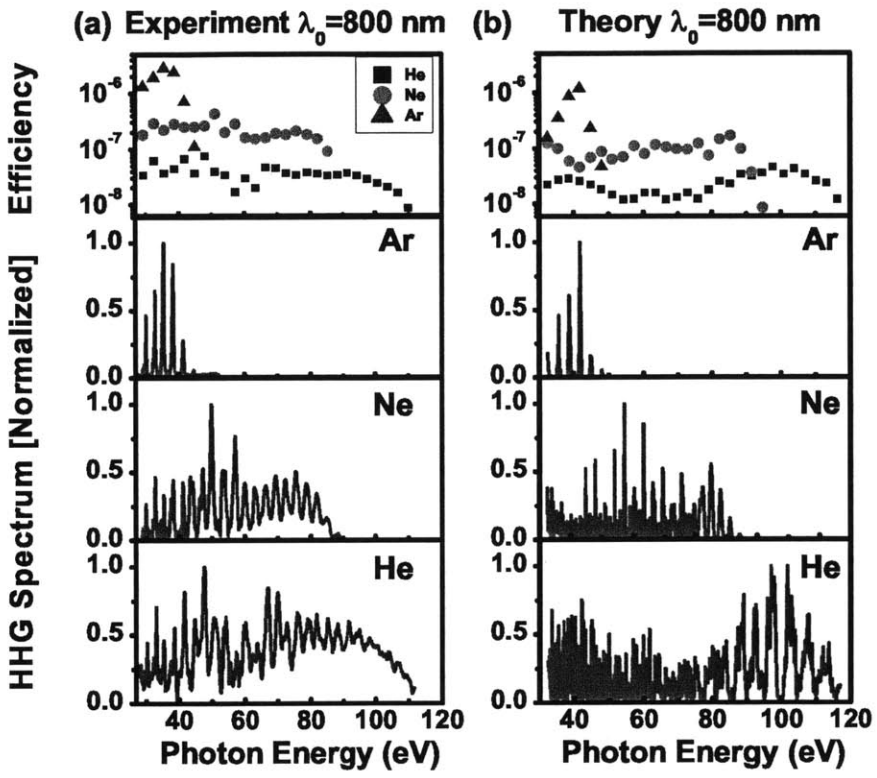

Figure 6-2: a) Experimental results for HHG driven by 800 nm, 35 fsec driver pulses with beam waist 40 μm: top row, efficiencies for Argon (50 mbar, 0.6 mJ), Neon (300 mbar, 2 mJ) and Helium (2 bar, 2mJ) using a 2 mm long nozzle; remaining rows, the respective normalized HHG spectra [44], b) Simulation results for Argon ($1.2 \cdot 10^{14}$ W/cm^2), Neon ($3.2 \cdot 10^{14}$ W/cm^2) and Helium ($7.4 \cdot 10^{14}$ W/cm^2) for the same interaction parameters like in (a).

imental counterpart and (b) that theoretical HHG spectra exhibit an interference structure even within a harmonic. Both of the aforementioned discrepancies stem from the fact that in the experiment we collect mostly the radiation from short electron trajectories by optimizing

phase-matching conditions and overall HHG yield, whereas in the theory the radiation from both the short and long electron trajectories is included in the harmonic spectrum. The intra-cycle harmonic structure is caused by interference between the long and short trajectories, which have the same return energy but different quantum phases [45]. Figure ?? shows the theoretical power spectrum for Neon with 800 nm driver pulses when we keep both short and long trajectories (Figure ??.a), short trajectories only (Figure ??.b) and long trajectories only (Figure ??.c). When we collect only the short trajectories the HHG spectrum shows clean harmonics without any interference structure. On the other hand, when we collect only the long trajectories, the harmonics are not clean anymore and there is interference structure resulting from inter-cycle interferences. These inter-cycle interferences are caused by the different quantum phases of long trajectories in each half cycle, which arc strongly intensity dependent leading to incoherent addition of the different half-cycle contributions to the same harmonic. If the driver pulse is flat top, then the intensity would be identical in each half-cycle, the phases would add up coherently and clear harmonics would appear.

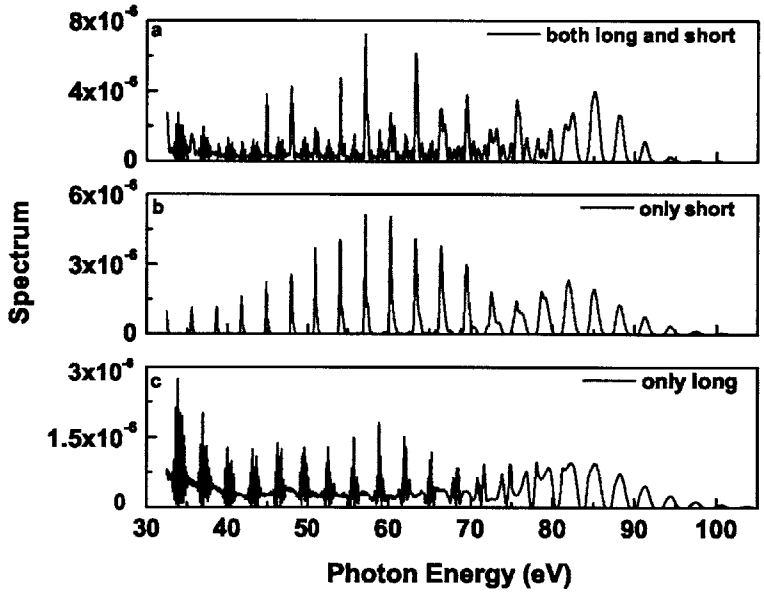

Figure 6-3: Theoretical power spectrum for Neon at 800 nm when we keep (a) both short and long trajectories, (b) only short trajectories and (c) only long ones.

6.2 Interplay of Multiphoton and Tunneling Ionization

Ionization is the first step in the HHG process and the choice of the proper model to describe it is crucial in achieving good agreement between theoretical and experimental results. The most commonly used ionization model is the theory established by Ammosov, Delone and Krainov, known as ADK theory [21]. This model is preferred due to its computational convenience and is derived for the case of a DC driving field, which corresponds to $\gamma = 0$ and therefore the channel of ionization is pure tunneling. It is commonly used for sinusoidal driving fields, but it is valid only for small Keldysh parameter for which the field-matter interaction is a non-perturbative process and tunneling is the main mechanism of ionization.

An alternative and more general method to calculate the ionization rate has been shown using the Landau-Dykhne method [20, 39]. A detailed discussion on the Landau-Dykhne method can be found in [46–48]. This method is valid in the adiabatic regime and includes multiphoton and tunneling ionization and is referred to as Yudin-Ivanov (YI) ionization theory [20].

When using the ADK theory for calculating the single atom response, a mismatch between theoretical and experimental results is observed, especially for low-order harmonics by short driver wavelengths. The Keldysh parameter, which is inversely proportional to the electric field, is larger in the wings of the pulse than near the peak of the pulse. Additionally, by decreasing the wavelength of the driver pulse (from 800 nm to 400 nm), the Keldysh parameter becomes larger than 1 in the wings and multiphoton ionization becomes important. Hence, ADK theory cannot model the ionization process accurately as it underestimates the ionization yield. Therefore, we use the YI ionization theory (in Figures 6-1.b and 6-2.b) for calculation of the HHG spectra and we find that it results in much better agreement with experimental results than ADK theory.

To get more insight, we compare the ionization rates (Figure 6-4.a and Figure 6-5.a) and the single atom response (Figure 6-4.b and Figure 6-5.b) calculated for a 400 nm and a 800 nm driver pulse using the ADK and the YI ionization models, respectively. For a 400 nm Gaussian driver pulse with a peak intensity of $8.5 \cdot 10^{14}$ W/cm^2 (Keldysh parameter $\gamma \sim 1$)

the YI ionization rate is higher than the ADK rate, over the entire pulse (Figure 6-4.a), but the relative mismatch is much more pronounced in the wings (Figure 6-4.a inset). As a result, there is a noticeable difference between the HHG spectra generated by the two models, especially for low photon energies (Figure 6-4.b inset). On the other hand, for 800 nm and a peak intensity $7.4 \cdot 10^{14}$ W/cm^2 (Keldysh parameter $\gamma = 0.52$) the two models give similar ionization rates over the entire pulse (Figure 6-5.a) and (Figure 6-5.a inset). The corresponding spectra generated from the two models are similar over the whole range of energies (Figure 6-5.b) and (Figure 6-5.b inset).

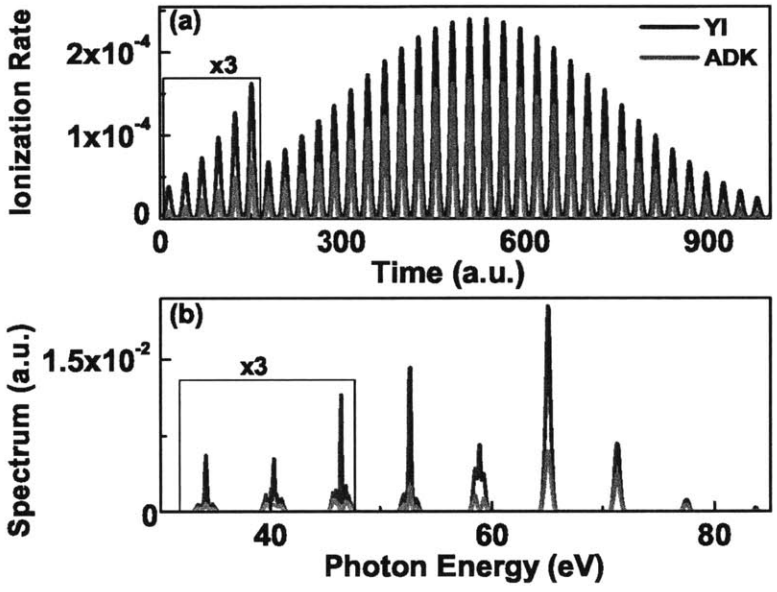

Figure 6-4: Ionization rates and spectral intensities of single atom response in Helium for the same conditions like in Figure 6-1 when using the YI (gray) and ADK (red (dark gray)) theory for 400 nm driver pulses ($\gamma \sim 1$). The insets show the ionization rates for the wings of the fields and the spectral intensities for the low harmonics pronounced three times.

A time-frequency representation gives a better understanding of a dynamic process involving broad spectral components. For this purpose, we plotted the spectrograms of the high-harmonic photons for 400 nm and 800 nm driver pulses using YI and ADK ionization models as shown in Figures 6-6 - 6-8. The spectrograms are calculated using a short-time

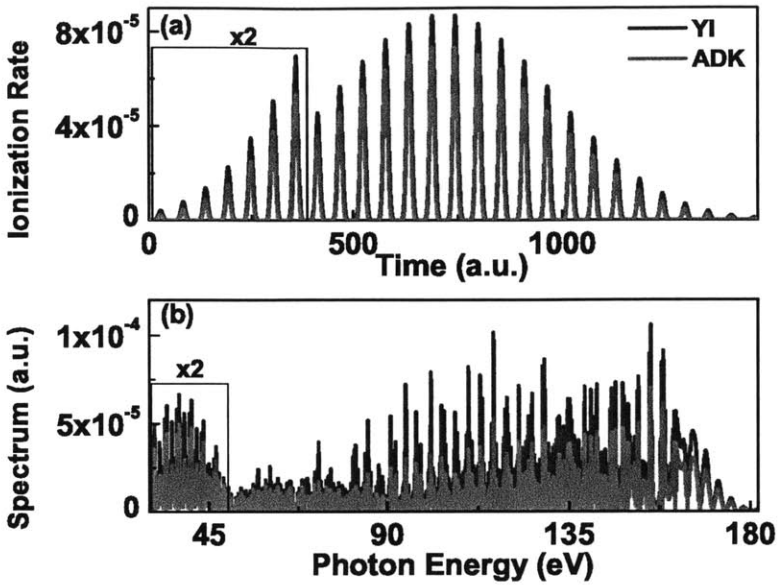

Figure 6-5: Ionization rates and spectral intensities of single atom response in Helium for the same conditions like in Figure 6-2 when using the YI (gray) and ADK (red (dark gray)) theory for 800 nm driver pulse ($\gamma \sim 0.52$). The insets show the ionization rates for the wings of the fields and the spectral intensities for the low harmonics pronounced two times.

Fourier transform with a Gaussian window function, which has a FWHM of 58 attoseconds. In Figure 6-6, we notice that the HHG spectrograms generated by the 800 nm pulse are insensitive to the choice of the ionization model. However, this is not the case for the 400 nm driver pulse in Figure 6-7. The spectrogram shows a higher photon yield over the different half cycles of the driver pulse when we use the YI model of ionization . This contrast is further enhanced in the wings of the driver pulse where the Keldysh parameter is the highest and multiphoton ionization the most prominent (Figure 6-8). Since the ADK model underestimates the ionization rate in the wings of the 400 nm driver pulse, which contribute strongly to low-order harmonics, it drastically underestimates the low harmonic energy photon yield.

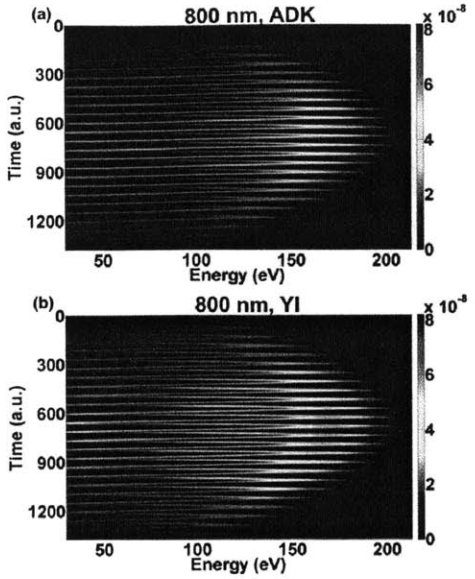

Figure 6-6: Spectrogram of the HHG spectrum from 800 nm driver pulse using (a) ADK and (b) YI ionization rates respectively. Both models (YI and ADK) predict similar low frequency photon intensity in the wings of the driver pulse.

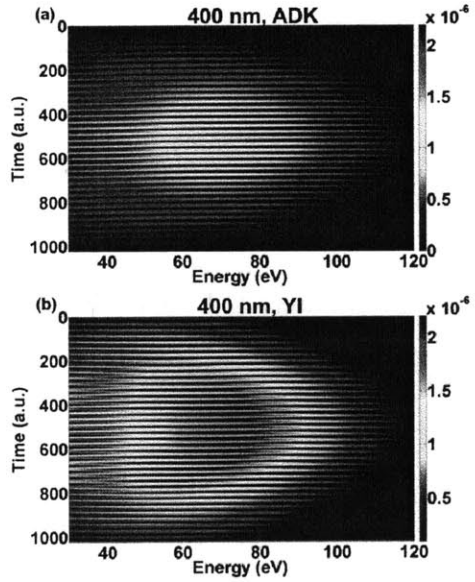

Figure 6-7: Spectrogram of the HHG spectrum with 400 nm driver pulse using (a) ADK and (b) YI ionization rates respectively. The YI model predicts a much higher low frequency photon intensity in the wings of the driver pulse than the ADK model.

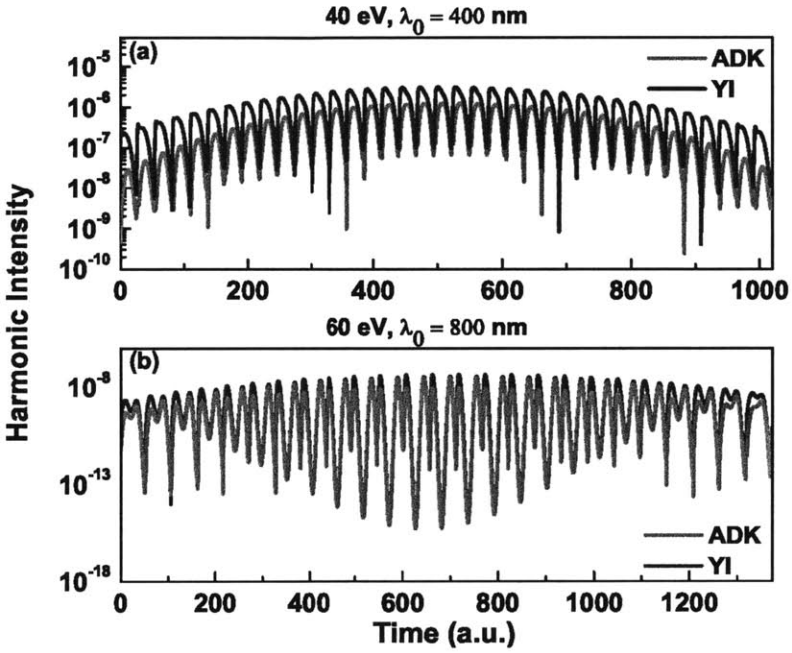

Figure 6-8: Harmonic intensity, calculated using YI and ADK theory for low photon energies. (a) For 40 eV and 400 nm driver pulses and (b) for 60 eV and 800 nm driver pulses. These ionization theories predict very different harmonic intensity, especially in the wings of the 400 nm driver pulse where γ is the largest.

Chapter 7

Results using 3-D model

In this Chapter, we extend the 1-D model to 3-D and we study the generation of radiation in the water window region of the spectrum by using driver pulses with 2 μm drive wavelength. We show that within the range of pressures one might choose for performing the experiment, at low pressures diffraction enhanced by plasma defocusing is the dominant limitation, at high pressures loss due to electron-neutral inverse bremsstrahlung is the main limitation and there is an intermediate regime of medium pressures, where both diffraction effects and loss due to electron-neutral inverse bremsstrahlung have an effect. These two effects do not allow phase matching to be maintained for long distance resulting in low efficiencies. Finally, we explore ways to mitigate the effect of plasma defocusing by using Supergaussian pulses and Gaussian pulses with large beam waists.

7.1 HHG using Long Wavelenghs

One important application of HHG is the creation of a coherent soft x-ray light source. As we have mentioned in Chapter 1, the spectral range between K-absorption edges of carbon (284 eV) and oxygen (543 eV), called the water window, can be used for high resolution biological imaging, since in this energy range water has low absorption for soft x-ray radiation, while carbon atoms absorb it [8]. An intense ultrafast water-window X-ray pulse would allow us

to capture images of live cells by instantaneously halting their motion, preserving structural information that is lost in the samples preparation process for electron microscopy [49].

There are two ways to extend the cutoff (Eq. 2.3). The first one is using a higher laser intensity, which has the disadvantage of leading to higher ionization levels and consequently to higher plasma density, making phase matching impossible. The phase mismatch between wavevectors of the driving and the harmonic fields is a very important limiting parameter for the conversion efficiency. The second way to extend the cutoff is by using longer drive wavelengths, as was first proposed by Lewenstein [18] and was explored experimentally as early as 2001 in Argon [50], and numerous work both theoretical and experimental followed [51–56].

Unfortunately the extension of the cutoff by increasing the drive wavelength comes with a dramatic decrease in the conversion efficiency. The conversion efficiency scales from the old to the new cutoff wavelength with ω_0^9 [28]. Thus increasing the drive wavelength by a factor of two, which increases the cutoff frequency by about a factor of 4, leads to an expected reduction of the single atom response by about 500.

We can increase the efficiency by increasing the number of atoms, which is achieved by working at high pressures or long medium lengths. It is fortunate that Helium and Neon which have high ionization potentials, which means we can work at high intensities, have low absorption cross sections and as a result long absorption lengths in the water window range (Figure 7-1) [57, 58]. This fact allows us to scale the pressure all the way up to 100 bars and have a reasonably sized medium length.

The inability to achieve phase matching limits the efficiency dramatically, as we can see in Figure 7-2, where we calculate the conversion efficiency per eV when a 10 mJ, 35 fsec, 2 μm drive wavelength and 154 μm beam waist Gaussian pulse in time and space, propagates through a 2 mm Helium jet with pressure 10 bar, when phase matching is not achieved ($\Delta k \neq 0$) (blue curve) and when phase matching is achieved ($\Delta k = 0$) (red curve). The gas jet is located on the focus of the beam. The value of the beam waist corresponds to an intensity at $t = 0$, which is 1.3 times the critical intensity I_{cr} at which the plasma and

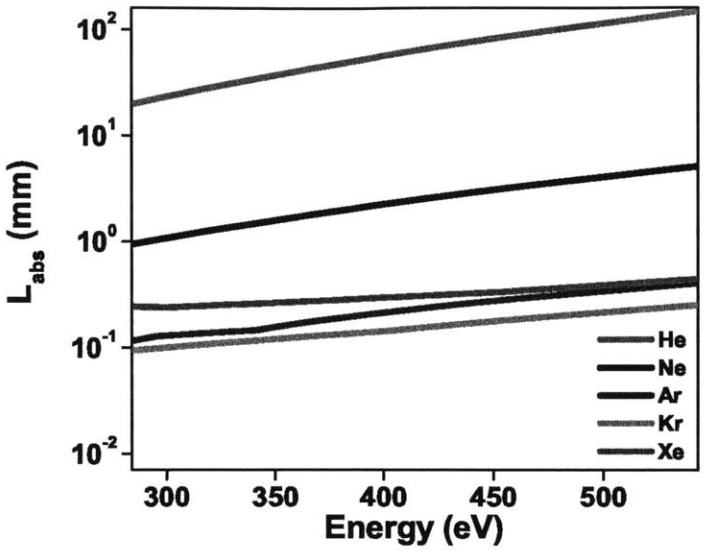

Figure 7-1: Absorption lengths of noble gases in water window region for pressure of 1 bar.

the neutral terms of the phase mismatch balance each other, as we will discuss below. We see that when $\Delta k = 0$, the efficiency per eV is three orders of magnitude higher than the case that $\Delta k \neq 0$. The case ($\Delta k = 0$) is not realistic, since it is impossible to achieve phase matching for the whole range of energies, but we present it here to show the limitation that Δk imposes to efficiency.

The phase mismatch Δk is the sum of the plasma-neutral contribution, the Gouy phase shift and the dipole phase. Here we consider the change in phase mismatch with z due to propagation effects. The effects, summarized in Chapter 3, include diffraction, which changes the beam width and intensity after propagation, plasma defocusing, which further alters the wavefront of the drive beam, thus enhancing the effects of diffraction, and driver field losses, which are dominated by inverse bremsstrahlung. Considering these effects, we may rewrite Eq. 3.23 in terms of the macroscopic quantities that change during propagation, i.e. beam width and intensity. The Gouy phase may be written as a function of beam width w_0, the plasma-neutral contribution as a function of beam width and intensity and the dipole phase

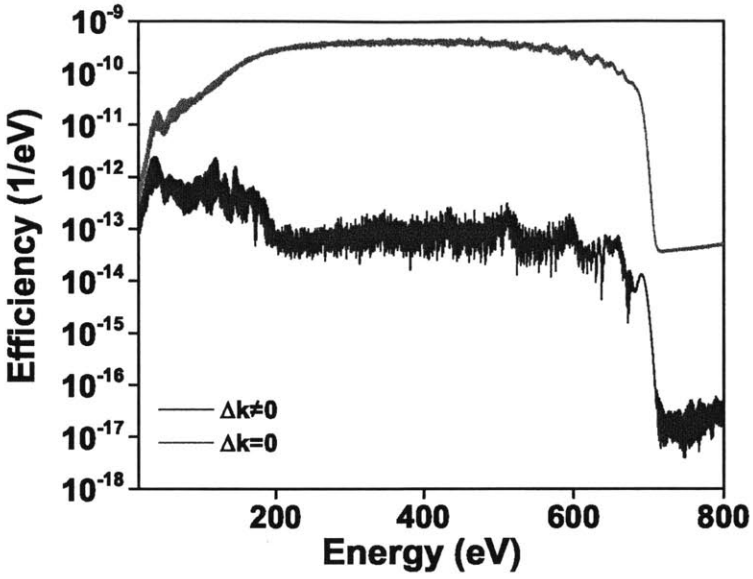

Figure 7-2: Efficiency per eV for HHG driven by 2000 nm, 10 mJ and 35 fsec Gaussian pulse in time and space with beam waist 154 μm in Helium when $\Delta k \neq 0$ (blue curve) and when $\Delta k = 0$ (red curve). The efficiency for $\Delta k = 0$ is three orders of magnitude higher than the case that $\Delta k \neq 0$.

as a function of intensity.

$$\Delta k(z) = \Delta k_{Gouy}(w_0(z)) + \Delta k_{plasma-neutral}(I(w_0(z), z)) + \Delta k_{dipole}(I(z)) \qquad (7.1)$$

It is much harder to achieve phase matching in this long wavelength regime for two main reasons. First, the harmonic order q is high and second since we would like to work at high pressures the phase matching becomes very sensitive to intensity and wavefront. When q is high, changes in pressure and/or intensity (beam waist) change the phase mismatch Δk very quickly. In addition, the higher is the pressure the stronger is the plasma created, which distorts the wavefront and this leads to rapid changes of beam shape and intensity with propagation. Thus, achieving phase matching is harder, since the phase matching condition changes rapidly with propagation.

As this Chapter will show, the main limitation to achieve high conversion efficiency

in long wavelength-driven HHG in a gas cell is the extreme sensitivity of Δk to changes in wavefront and intensity during propagation. This behavior is the result of the large number of atoms we employ in order to make up for the low single atom response and boost the conversion efficiency. We show that within the range of pressures one might choose for performing the experiment, at low pressures (0.1-1 bar) diffraction enhanced by plasma defocusing is the dominant limitation, at high pressures >20 bar) loss due to electron-neutral inverse bremsstrahlung is the main limitation and there is an intermediate regime of medium pressures (1-20 bar) where both diffraction effects and loss due to electron-neutral inverse bremsstrahlung have an effect.

In Figure 7-3, is shown the peak intensity of the driving field versus radial coordinate r and propagation z for the samc parameters like in Figure 7-2 apart from the pressure and the medium length, whose product however is kept constant. The peak intensity is plotted for cases at which the product of pressure and medium length is kept constant, so that the number of atoms is the same for all four cases. In Figure 7-3.a (pressure 1 bar and medium length 20 mm) and 7-3.b (pressure 10 bar and medium length 2 mm) the effects of diffraction and plasma defocusing are dominant and in Figure 7-3.c (pressure 100 bar and medium length 200 μm) and 7-3.d (pressure 1000 bar and medium length 20 μm), which correspond to higher pressures and consequently smaller medium lengths, the effect of absorption due to electron-neutral collisions is the dominant phenomenon. In Figures, 7-3.c and 7-3.d the diffraction and as a result the plasma defocusing have a minimal role since the Rayleigh length is for this set of parameters is 36.2 mm.

The HHG efficiencies for the four cases presented in Figure 7-3 are shown in Figure 7-4. We see that the efficiency depends highly on the pressure. In the following sections we investigate the factors leading to these outcomes.

At high pressure and short medium length the dominant effect is the absorption due to electron-neutral inverse bremsstrahlung. For pressure 320 bar, at which the electron-neutral inverse bremsstrahlung cross section has its highest value, the peak intensity shows the highest absorption due to electron-neutral collisions (Figure 7-5).

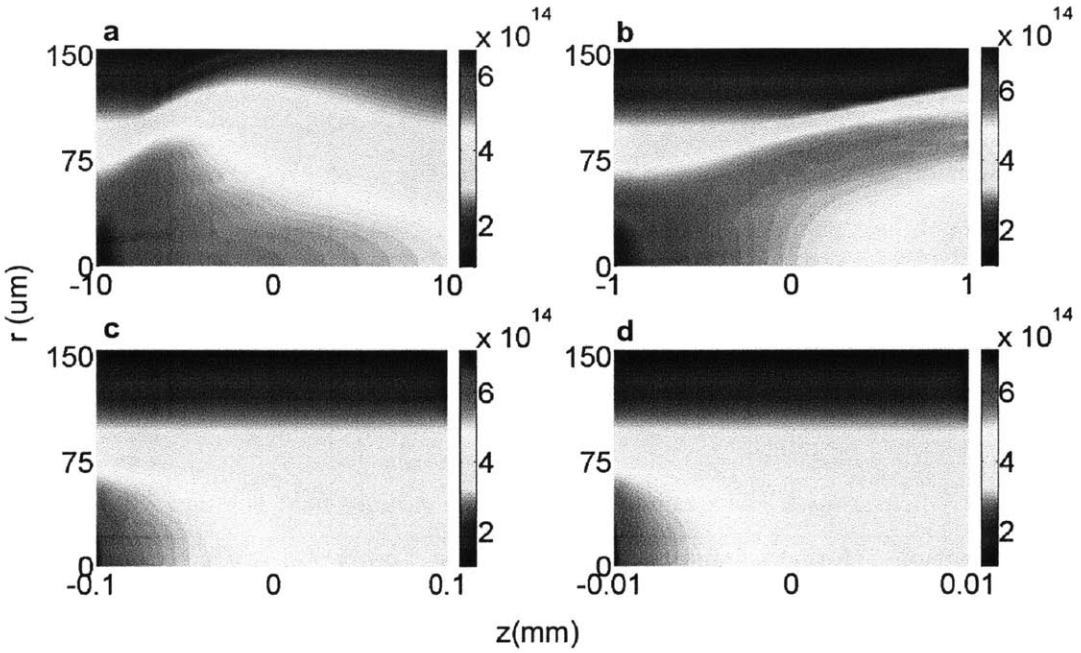

Figure 7-3: Peak intensity versus radial coordinate r and propagation z when a 10 mJ, 35 fsec, 2 μm drive wavelength and 154 μm beam waist Gaussian pulse propagates through a Helium jet, for a) pressure 1 bar and medium length 20 mm, b) pressure 10 bar and medium length 2 mm, c) pressure 100 bar and medium length 200 μm, d) pressure 1000 bar and medium length 20 μm.

In the following section, we will study the effect of change of phase matching with propagation distance z which limits the coherence length, and the losses due to electron-neutral inverse bremsstrahlung. These phenomena were not taken into account in the 1-D study. For all these effects we will define quantities which enable us to appreciate the importance of the different macroscopic phenomena in harmonic generation. Finally, due to the nature of the 3-D problem, which is very sensitive to phase matching, we should expect some very complicated spatial-temporal properties to the generated harmonics.

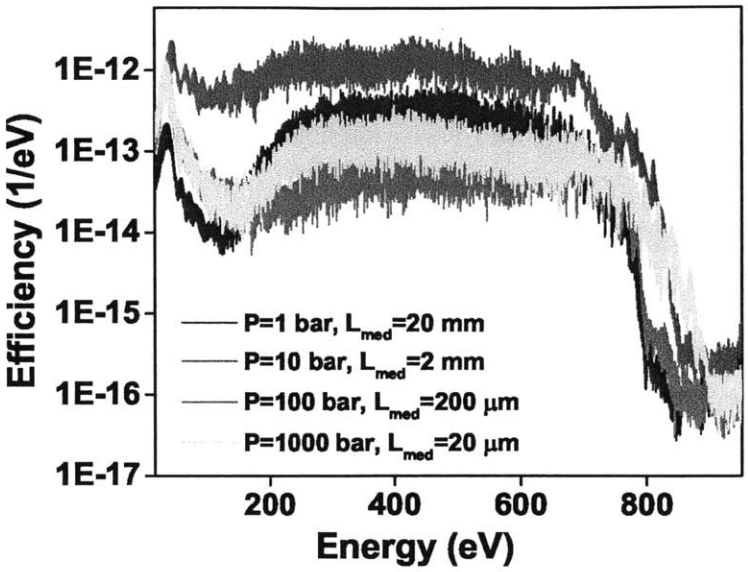

Figure 7-4: HHG effieciency when a 10 mJ, 35 fsec, 2 μm drive wavelength and 154 μm beam waist Gaussian pulse is focused in a Helium jet, for pressure 1 bar and medium length 20 mm (blue), pressure 10 bar and medium length 2 mm (red), pressure 100 bar and medium length 200 μm (magenta) and pressure 1000 bar and medium length 20 μm (green).

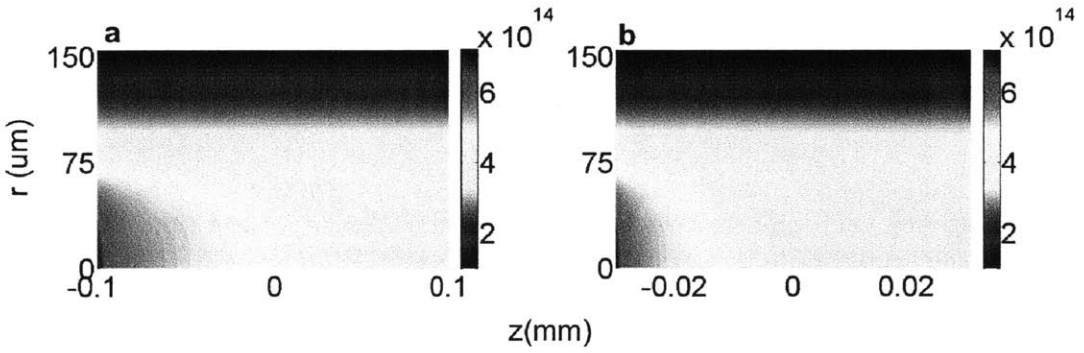

Figure 7-5: Peak intensity versus radial coordinate r and propagation z when a 10 mJ, 35 fsec, 2 μm drive wavelength and 154 μm beam waist laser pulse propagates through a Helium jet, for a) pressure 100 bar and medium length 200 μm, b) pressure 320 bar and medium length 62.5 μm. The colorbar is in W/cm^2.

7.2 Observation of Variation in Coherence Length during Propagation

In this section we look how the driving and harmonic fields vary along z for a case with the same parameters like in Figure 7-2. The driving field evolution along propagation distance z as a function of radial coordinate r and time t is shown in Figure 7-6. In Figure 7-6.a the pulse is at the beginning of the medium and in Figure 7-6.b the driving pulse has propagated and the peak of the pulse does not happen anymore at $t = 0$, but at an earlier time. In Figures 7-6.c, 7-6.d, 7-6.e and 7-6.f, which correspond to later points along z, the plasma highly distorts the driving pulse and is shown specifically how the plasma, which is generated by the front of the pulse, highly distorts the back of the pulse.

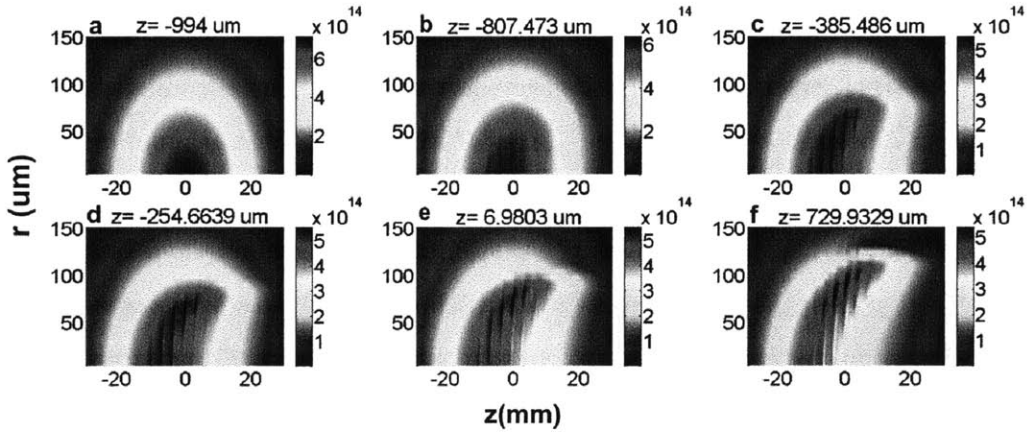

Figure 7-6: Driving field intensity as function of radial coordinate r and time t for different points along the propagation distance z. The colorbar is in W/cm^2.

The generated harmonic spectrum from the driving field in Figure 7-6 as we propagate along z is shown in Figure 7-7. From the beginning of the medium until z=-800 μm, we see buildup of harmonics up to 200 eV and until we reach z=-400 μm not much happens in the water window. Around z=-250 μm we see an abrupt generation of water window radiation, but for the rest of the propagation we see no buildup of the harmonic field. We observe only a gradual loss. The reason is that due to large phase mismatch, L_{coh} is short. Thus,

harmonic generation takes place at limited points in z.

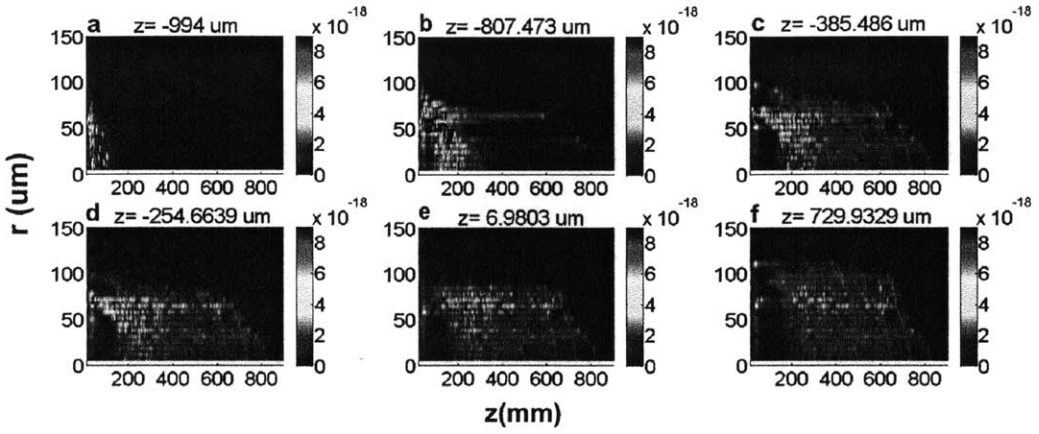

Figure 7-7: Harmonic field as function of radial coordinate r and EUV energy for different points along the propagation distance z.

The generation of harmonics at specific points in z is more evident when we integrate the HHG spectrum for the energies in the water window range and we plot it as a function of radial coordinate r and propagation distance z (Figure 7-8). We observe that we have an abrupt generation in z and for different points in r, the points in z that generation takes place are different. The light in the lower half of the water window starts to decay due to EUV absorption, while in the higher frequencies there is less absorption.

In Figure 7-8.b, there is a 1.2 mm length (between -200 μm up to 1 mm) over which photons in the water window range (284-543 eV) are generated. For z between -200 μm up to 200 μm and $r = 65\mu$m the water window radiation has the highest values and then drops, remaining slightly constant until the end of the medium. The drop in intensity matches very well the rate of absorption of Helium in the water window region (Figure 7-8.a). Phase matching happens at a particular radius (65 μm) because at this radius the ionization probability has the proper value.

In Helium at 10 bar, the absorption length at 400 eV is 5.6 mm while the absorption length at 300 eV is 2.3 mm (Figure 7-8.a). Since the absorption length for the smallest energies of the water window region is significantly shorter than the one for the higher

energies of that region, we expect that the initial high value of the intensity of the integrated spectrum for z between -200 μm up to 200 μm is followed by a significant drop, due to the absorption length of all water window energies. On the other hand, the almost constant intensity of the integrated spectrum between 200 μm up to 1 mm is due to the absorption length between 400 and 543 eV, since the absorption length for the range 284 up to 400 eV is smaller and as a result the intensity drops faster.

The previous argument is illustrated in the next two Figures. In Figure 7-8.c is shown the integrated harmonic spectrum of Helium over the water window energies between 284-400 eV as a function of radial coordinate r and propagation distance z, while in Figure 7-8.d is shown the integrated harmonic spectrum of Helium over the water window energies between 400-543 eV as a function of radial coordinate r and propagation distance z. In Figure 7-8.c the intensity of the harmonic spectrum drops along z from its peak value at z=-200 μm, while in Figure 7-8.d the intensity stays almost the same. The reason is the fact that the absorption length for the energy range 284-400 eV is smaller than the range 400-543 eV, which means that the HHG yield in the range 284-400 eV is absorbed more than the HHG yield in the range 400-543 eV.

7.3 Effect of Beam Waist and Intensity Change on Phase Matching

Here we take the simplistic approach giving a measure of how sensitive the phase matching is to beam waist changes due to diffraction and to intensity changes due to electron-neutral inverse bremsstrahlung.

In order to study how quickly phase mismatch changes along propagation, we take the derivative of phase mismatch Δk with z.

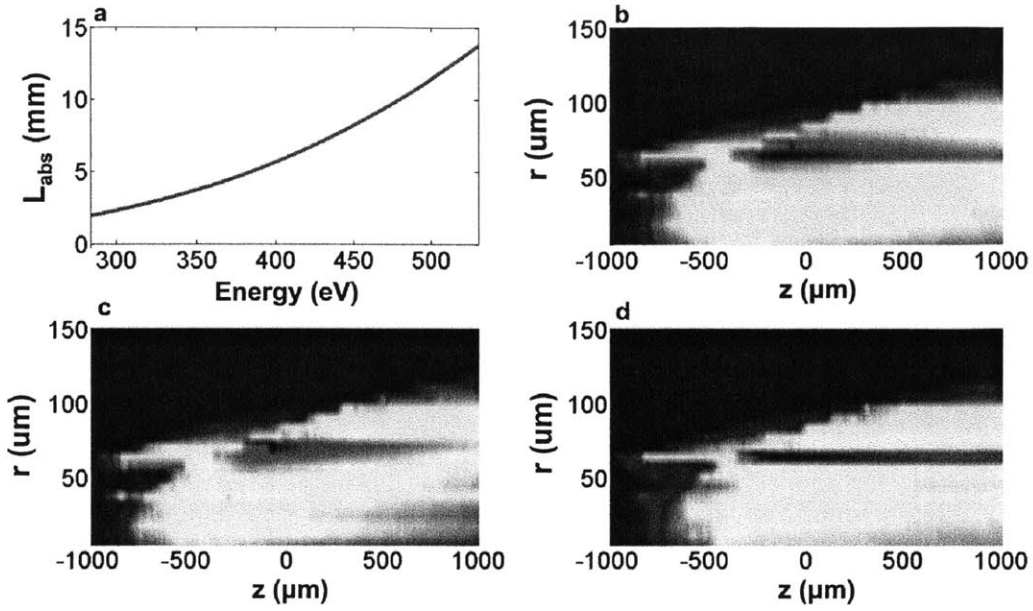

Figure 7-8: a) Absorption length of Helium for 10 bar at the water window range, b) HHG spectrum integrated over the water window energy range, as a function of radial coordinate r and propagation distance z, c) HHG spectrum as a function of radial coordinate r and propagation distance z integrated over the energy range 284-400 eV, d) HHG spectrum as a function of radial coordinate r and propagation distance z integrated over the water window energy range 400-543 eV.

$$\frac{\partial \Delta k}{\partial z} = \frac{\partial \Delta k_{Gouy}}{\partial w_0}\frac{\partial w_0}{\partial z} + \frac{\partial \Delta k_{plasma-neutral}}{\partial I}\frac{\partial I}{\partial w_0}\frac{\partial w_0}{\partial z} + \frac{\partial \Delta k_{plasma-neutral}}{\partial I}\frac{\partial I}{\partial z} + \frac{\partial}{\partial z}\alpha_{dipole}\left(\frac{\partial I}{\partial z} + \frac{\partial I}{\partial w_0}\frac{\partial w_0}{\partial z}\right) \tag{7.2}$$

If we group the terms in Eq. 7.2 in terms of beam waist change and intensity change, we see that diffraction (beam waist change) has effect on Gouy phase shift, plasma-neutral and dipole phase contribution, while electron-neutral inverse bremsstrahlung (intensity change)

affects the plasma-neutral and the dipole phase contribution (Eq. 7.3).

$$\frac{\partial \Delta k}{\partial z} = \left[\frac{\partial \Delta k_{Gouy}}{\partial w_0} + \left(\frac{\partial \Delta k_{plasma-neutral}}{\partial I} + \frac{\partial}{\partial z}\alpha_{dipole}\right)\frac{\partial I}{\partial w_0}\right]\frac{\partial w_0}{\partial z} + \left(\frac{\partial \Delta k_{plasma-neutral}}{\partial I} + \frac{\partial}{\partial z}\alpha_{dipole}\right)\frac{\partial I}{\partial z} \tag{7.3}$$

At high pressures the electron-neutral inverse bremstrahlung acts faster than diffraction, while for low pressures the diffraction is dominant. We will ignore the contribution of the dipole phase to phase matching, since it is a second order term in z and the analysis becomes complex. Thus, we focus on the plasma-neutral and Gouy terms.

The optimizing conditions under which the macroscopic response is more than half the maximum response are $L_{med} > 3L_{abs}$ and $L_{coh} > 5L_{abs}$, which means that the smallest ratio under which phase matching conditions are partially fulfilled is $L_{med}/L_{coh} = 0.6$. When $\Delta k = 0$ then $L_{med}/L_{coh} = 0$. Thus for L_{med}/L_{coh} between 0 and 0.6, Δk does not vary dramatically and we can consider that phase matching is preserved.

7.3.1 Effect of Diffraction

In Figure 7-9 are shown the plasma-neutral contribution to phase mismatch for different pressures and the Gouy contribution (black curve) as a function of beam waist. The points at which the curves cross with the black one, correspond to the beam waists for which the plasma-neutral contribution and the Gouy contribution balance each other and phase matching is achieved, i.e. $\Delta k = 0$. The higher is the pressure the smaller is the beam waist at which $\Delta k = 0$.

Looking at the relative slopes, the rates of change at the crossing points, which correspond to beam waists for which $\Delta k = 0$, we see that the higher is the pressure the steeper is the slope which translates to the fact that a tiny change in intensity rapidly changes the phase mismatch. The differences between the curves with orange, red, blue, purple and green colors in Figure 7-9 are factors of pressure times plasma neutral contribution. There is a much higher sensitivity of phase mismatch to beam waist (intensity change) as pressure

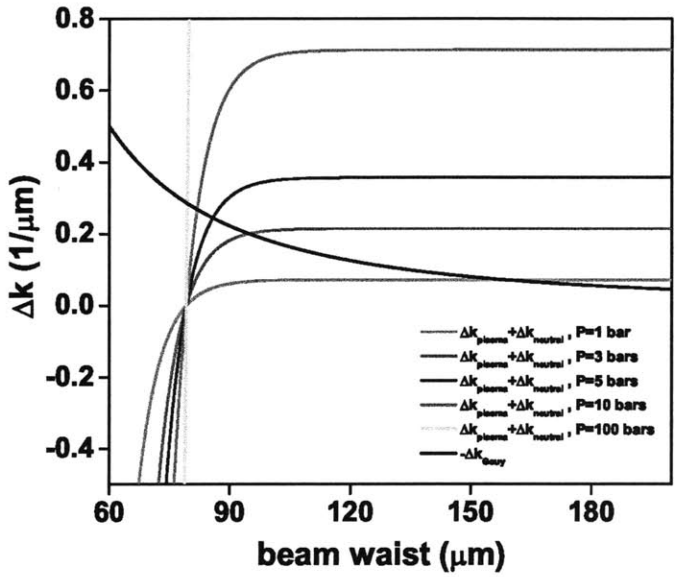

Figure 7-9: Plasma-neutral contribution for different pressures and Gouy phase shift (black curve) contribution to phase mismatch at 400 eV, as a function of beam waist for pulse 2 mJ, 35 fsec, drive wavelength 2.06 μm in Helium.

increases, but this translates to a much smaller length at which the driving and harmonic field can propagate and stay in phase.

In addition, we want to study how L_{med}/L_{coh} changes as a function of beam waist for the plasma-neutral and Gouy phase shift contributions to phase mismatch, as shown in Figure 7-10. If $L_{med} = 3L_{abs}$ (one of the two conditions for optimum harmonic generation) and since $L_{coh} = \pi/\Delta k$, then $L_{med}/L_{coh} = \Delta k \cdot L_{abs}$. The black curve is the change of L_{med}/L_{coh} versus beam waist, due to plasma neutral contributions. The plasma-neutral contribution is now fixed because it is pressure independent. The other curves show the change of L_{med}/L_{coh} versus beam waist for different pressures due to Gouy phase shift. The pressure dependence is due to the absorption length, since Gouy phase shift is pressure independent. The points at which the curves cross are the waists for which $\Delta k = 0$. Following the black curve shows how much a change in intensity changes phase matching through the plasma neutral balance, and following the other curves shows how much a change in beam waist affects the phase

mismatch due to the Gouy phase shift.

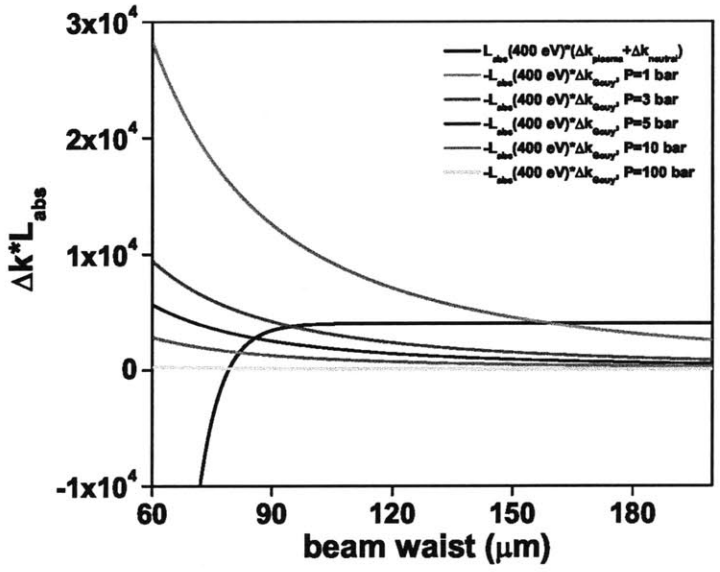

Figure 7-10: L_{med}/L_{coh} as a function of beam waist due to plasma-neutral contribution (black curve) and Gouy phase shift contribution for different pressures at 400 eV for pulse 2 mJ, 35 fsec, drive wavelength 2.06 μm in Helium.

The orange curve (1 bar) has a larger slope than the red one, meaning that L_{med}/L_{coh} is more sensitive to a change due to the Gouy phase shift. However at higher pressures (10 bar and 100 bar) the red curve has a higher slope than the purple and green curves and thus L_{med}/L_{coh} is more sensitive to a change in intensity due to plasma-neutral balance. So change in intensity plays more role than change in beam waist for high pressures.

Starting with the beam waist change, we define a beam waist sensitivity parameter $\mathcal{B}$, which measures how quickly phase matching is affected by the beam waist change. It is equal to the fractional change in beam waist w_0, when L_{med}/L_{coh} goes from 0 ($\Delta k = 0$) to 0.6 and is defined as

$$\mathcal{B} = \frac{\Delta w_0}{w_0|_{\frac{L_{med}}{L_{coh}}=0}} \tag{7.4}$$

The slope of L_{med}/L_{coh} versus beam waist w_0, for the beam waist at which $L_{med}/L_{coh} = 0$ is

$$\left.\frac{d\left(\frac{L_{med}}{L_{coh}}\right)}{dw_0}\right|_{w_0\left(\frac{L_{med}}{L_{coh}}=0\right)} = \frac{\Delta\left(\frac{L_{med}}{L_{coh}}\right)}{\Delta w_0} = \frac{0.6}{\Delta w_0} \tag{7.5}$$

and from Eq. 7.4 and Eq. 7.5

$$\mathcal{B} = \frac{1}{w_0|_{\frac{L_{med}}{L_{coh}}=0}} \cdot \frac{0.6}{\left.\frac{d\left(\frac{L_{med}}{L_{coh}}\right)}{dw_0}\right|_{w_0\left(\frac{L_{med}}{L_{coh}}=0\right)}} \tag{7.6}$$

We also want to calculate how long the field can propagate with phase matching, varying from 0 to a value at which $L_{med}/L_{coh} = 0.6$. In other words, we want to find the distance over which diffraction does not change the beam waist a lot.

The variation of waist due to diffraction is given by

$$w_0' = w_0\sqrt{1 + \left(\frac{z}{z_R}\right)^2} \tag{7.7}$$

where z_R is the Rayleigh length. The beam waist sensitivity parameter $\mathcal{B}$ is

$$\mathcal{B} = \frac{w_0' - w_0}{w_0} = \sqrt{1 + \left(\frac{z}{z_R}\right)^2} - 1 \tag{7.8}$$

and, from Eq. 7.8, we can define the propagation tolerance parameter z_{tol} which shows how long the beam can propagate with phase matching varying from 0 to value at which $L_{med}/L_{coh} = 0.6$. Thus

$$z_{tol} = z_R\sqrt{(\mathcal{B}+1)^2 - 1} \approx z_R\sqrt{2\mathcal{B}} \tag{7.9}$$

Grouping the sensitivity parameters when the beam waist changes, for HHG in Helium using a 2.06 μm driver pulse with energy 2 mJ and duration 35 fsec we get:

Table 7.1: Sensitivity parameters for beam waist change for HHG in Helium using a 2.06 μm driver pulse with energy 2 mJ and duration 35 fsec

P(bar)	$w_0(\Delta k = 0)$ (μm)	I(Δk=0) (W/cm^2)	$\delta(t = 0)$ (%)	$\mathcal{B}$ (%)	E_{Cutoff} (eV)	$L_{abs}(400eV)$ (mm)	b(mm)	z_{tol} (mm)	$\frac{z_{tol}}{3L_{abs}}$ (%)
1	158.77	$1.35 \cdot 10^{14}$	$8 \cdot 10^{-7}$	$7.44 \cdot 10^{-3}$	185.22	56.62	76.88	0.46	0.276
3	94.83	$3.8 \cdot 10^{14}$	0.004	$5.05 \cdot 10^{-3}$	474.87	18.87	27.42	0.13	0.243
5	85.81	$4.64 \cdot 10^{14}$	0.023	$2.44 \cdot 10^{-3}$	574.51	11.32	22.45	0.078	0.231
10	81.89	$5.09 \cdot 10^{14}$	0.046	$1.53 \cdot 10^{-3}$	628.35	5.66	20.45	0.056	0.333
100	79.43	$5.41 \cdot 10^{14}$	0.07	$1.11 \cdot 10^{-3}$	667.08	0.56	19.24	0.045	2.667

where P denotes pressure, w_0 the beam waist, I the intensity, δ the ionization probability, E_{cutoff} the cutoff energy and b the confocal parameter.

From Table 7.1, looking at the last column $z_{tol}/3L_{abs}$, we see that the higher is the pressure the bigger is the fraction of the medium length over which phase matching is preserved. However, the higher the pressure the smaller is the tolerance to beam waist change, column $\mathcal{B}$, but this quantity is less important than $z_{tol}/3L_{abs}$. The higher the pressure, the higher the ionization probability δ at which phase matching is achieved and as a result the efficiency gets higher. The higher the pressure the smaller the L_{abs} and as a result the smaller L_{med} we need, which results to less diffraction and less defocusing. Small medium lengths are more practical for performing the experiments. In addition, the higher the pressure (the smaller the confocal parameter) the smaller the beam waist we need to achieve phase matching, but in this case diffraction is stronger. On the other hand, the higher the pressure the higher the losses, due to electron-neutral inverse bremsstrahlung. However, this is not taken into account here. Also we do not take into account the sensitivity of phase matching to shot to shot fluctuations of the peak power, which affects phase matching through the plasma and neutral elements.

From the last column of the Table 7.1 we can conclude that the higher is the pressure the longer Δk is preserved. Since there are 3 parameters that are changing in the last column, $z_{tol}/3L_{abs}$ goes through a local minimum and grows again. As the pressure increases, L_{abs}

and as a result the medium length shrinks, we win since there is not any beam propagation. The medium length is shrinking faster than the diffraction length, so there is not significant change of the beam waist over the medium length.

Regarding the optimum values for each of the columns in Table 7.1, we conclude the following. The optimum beam waist is the one with the highest value within the water window range, since it gives less defocusing. The optimum intensity is the one with the lowest value within the water window region, since it results to less wavefront distortion. The optimum ionization probability δ is the one which has the closest value to the δ for which only neutral and plasma contributions to Δk are taken into account. Also the higher the ionization probability, the higher is the efficiency. For the beam waist sensitivity parameter $\mathcal{B}$ we would choose the highest one within the water window range. The optimum L_{abs} are the ones which give practical medium lengths up to 2 cm. Finally, for $z_{tol}/3L_{abs}$ the higher value it has the better, since this means that we can propagate longer in the medium without Δk deteriorating.

7.3.2 Effect of Electron-neutral Inverse Bremsstrahlung

As mentioned earlier, the effect of electron-neutral inverse bremsstrahlung is dominant for high pressures and short medium lengths, as it is shown in Figure 7-11, which is for the same parameters like Figure 7-3, without including the effect of electron-neutral inverse bremsstrahlung. Comparing Figure 7-11.c with Figure 7-3.c and Figure 7-11.d with Figure 7-3.d respectively, it is clear that the electron neutral inverse bremsstrahlung is dominant, the higher the pressure and the shorter the medium length.

For the intensity change, given the amount of electron-neutral collisions, we will calculate the length over which the beam can propagate, so that phase matching varies from 0 to value at which $L_{med}/L_{coh} = 0.6$. We will call this length electron-neutral collision tolerance.

The slope of L_{med}/L_{coh} versus intensity I, for the intensity at which $L_{med}/L_{coh} = 0$

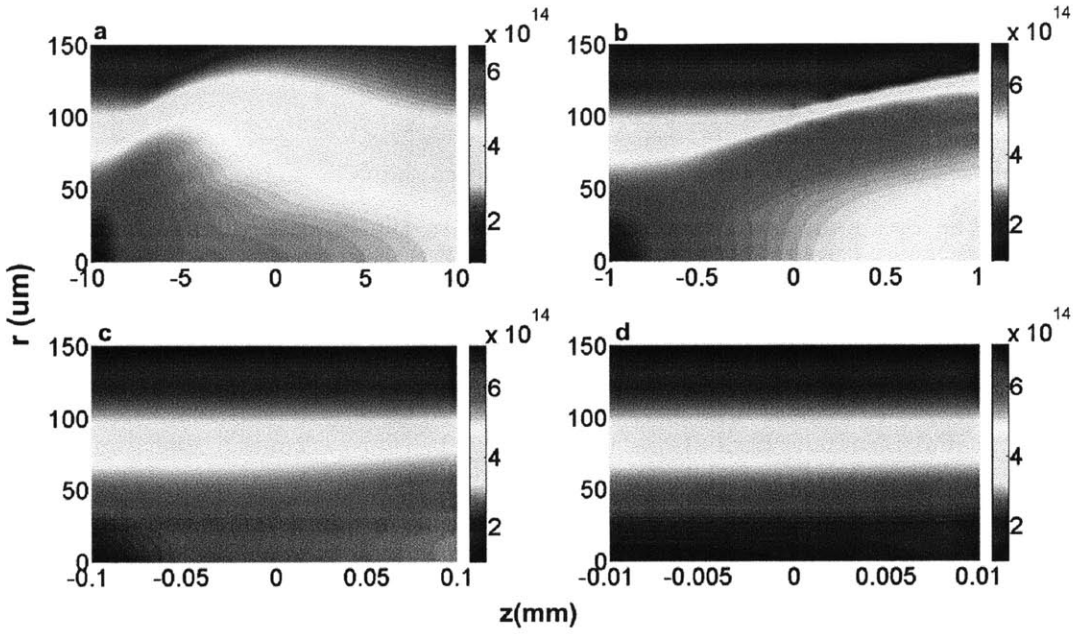

Figure 7-11: Peak intensity versus radial coordinate r and propagation z without including the effect of electron-neutral inverse bremsstrahlung, when a 10 mJ, 35 fsec, 2 μm drive wavelength and 154 μm beam waist laser pulse propagates through a Helium jet, for a) pressure 1 bar and medium length 20 mm, b) pressure 10 bar and medium length 2 mm, c) pressure 100 bar and medium length 200 μm, d) pressure 1000 bar and medium length 20 μm. The colorbar is in W/cm^2.

$(\Delta k = 0)$ is

$$\left.\frac{d\left(\frac{L_{med}}{L_{coh}}\right)}{dI}\right|_{I\left(\frac{L_{med}}{L_{coh}}=0\right)} = \frac{\Delta\left(\frac{L_{med}}{L_{coh}}\right)}{\Delta I} = \frac{0.6}{\Delta I} \tag{7.10}$$

In addition,

$$\left.\frac{dI}{dz}\right|_{\frac{L_{med}}{L_{coh}}=0} = \frac{\Delta I}{\Delta z} \tag{7.11}$$

and we get

$$\Delta I = \Delta z \left.\frac{dI}{dz}\right|_{\frac{L_{med}}{L_{coh}}=0} \tag{7.12}$$

From Eq. 7.10 and Eq. 7.12 we get the electron-neutral collision tolerance

$$\Delta z = \frac{1}{\frac{dI}{dz}\Big|_{\frac{L_{med}}{L_{coh}}=0}} \cdot \frac{0.6}{\frac{d\left(\frac{L_{med}}{L_{coh}}\right)}{dI}\Big|_{I\left(\frac{L_{med}}{L_{coh}}=0\right)}} \tag{7.13}$$

We can express $\frac{dI}{dz}\Big|_{\frac{L_{med}}{L_{coh}}=0}$ as following:
The absorption of the driving field due to electron-neutral collisions is

$$\frac{\partial E}{\partial z} = -\frac{\sigma_{IB}}{2}(1 + i\omega\tau_c)\rho E \tag{7.14}$$

We have

$$\frac{\partial |E|^2}{\partial z} = E^* \frac{\partial E}{\partial z} + E\frac{\partial E^*}{\partial z} = -|E|^2\frac{\rho\sigma_{IB}}{2}(1 + i\omega\tau_c) - |E|^2\frac{\rho\sigma_{IB}}{2}(1 - i\omega\tau_c) = -\rho\sigma_{IB}|E|^2 \tag{7.15}$$

and in Eq. 7.13

$$\frac{dI}{dz}\Big|_{\frac{L_{med}}{L_{coh}}=0} = -\rho\left(\frac{L_{med}}{L_{coh}} = 0\right)\sigma_{IB} I\left(\frac{L_{med}}{L_{coh}} = 0\right) \tag{7.16}$$

In addition to the electron-neutral collision tolerance, we define the electron-neutral collision length, which is the length at which the electron-neutral collision reduces the intensity by e, equal to $1/(\rho\sigma_{IB})$.

Grouping the sensitivity parameters when the intensity changes, for HHG in Helium using a 2.06 μm driver pulse with energy 2 mJ and duration 35 fsec we get:

Table 7.2: Sensitivity parameters for intensity change for HHG in Helium using a 2.06 μm driver pulse with energy 2 mJ and duration 35 fsec

P(bar)	$w_0(\Delta k = 0)$ (μm)	I(Δk=0) (W/cm^2)	$\delta(t = 0)$ (%)	E_{Cutoff} (eV)	$L_{abs}(400eV)$ (mm)	$1/(\rho\sigma_{IB})$ (m)	Δz(m)	$\frac{\Delta z}{3L_{abs}}$ (%)
1	158.77	$1.35 \cdot 10^{14}$	$8 \cdot 10^{-7}$	185.22	56.62	$1.29 \cdot 10^{6}$	$1.246 \cdot 10^{7}$	$7.33 \cdot 10^{9}$
3	94.83	$3.8 \cdot 10^{14}$	0.004	474.87	18.87	2.53	$6.99 \cdot 10^{-4}$	1.23
5	85.81	$4.64 \cdot 10^{14}$	0.023	574.51	11.32	0.1898	$1.19 \cdot 10^{-5}$	0.03
10	81.89	$5.09 \cdot 10^{14}$	0.046	628.35	5.66	0.024	$7.97 \cdot 10^{-7}$	$4.7 \cdot 10^{-3}$
100	79.43	$5.41 \cdot 10^{14}$	0.07	667.08	0.56	$1.7 \cdot 10^{-4}$	$3.8 \cdot 10^{-9}$	$2.24 \cdot 10^{-4}$

From Table 7.2, looking at the last column $\Delta z/3L_{abs}$, we see that the higher the pressure the shorter is the fraction of the medium length over which phase matching is preserved. This is expected since the higher is the pressure the stronger is the effect of the electron-neutral inverse bremsstrahlung.

7.4 Mitigation of Plasma Defocusing

As we discussed before, the effect of plasma defocusing is significant and does not permit phase matching. We want to reduce the effect of diffraction and consequently of plasma defocusing. We wish to test three possible ways of achieving that: a) choose a beam shape that diffracts less (i.e. Supergaussian pulse), b) make a larger Gaussian beam which will diffract less and c) minimize diffraction by shortening the medium length and increasing the pressure. However, the last way increases the effect of electron-neutral inverse bremmstrahlung loss and thus it is not favorable.

7.4.1 Supergaussian Pulse

The beam shape that we choose in order to reduce the effect of diffraction is the Supergaussian pulse, which has the form:

$$E = E_0 \exp\left(\frac{r}{w_0}\right)^n \tag{7.17}$$

where E_0 is the field amplitude, r is the radial coordinate, w_0 is the beam waist and n is the order of the Supergaussian. The shape of the Supergaussian makes the wings to diffract less than the ones of the Gaussian pulse and as a result the effect of plasma defocusing is less significant in the Supergaussian than the Gaussian.

In Figure 7-12 we see how the Supergaussian pulse evolves as it propagates along z for $t = 0$, as a function or radius r. The Supergaussian pulse experiences diffraction, which causes energy to move off axis and as a result the pulse becomes less flat. Wings diffract more than the center and there is a strong local diffraction at the edges. The edges move outwards and we see a drop of peak intensity.

At low pressures plasma defocusing is more important than the loss due to the electron-neutral inverse bremsstrahlung. At high pressures the loss due to the electron-neutral inverse bremsstrahlung is more important. Both phenomena are present in both cases and what matters is their relative strength. There is this intermediate regime between 10 bar and 100 bar, where it is unclear which of the two phenomena is dominant.

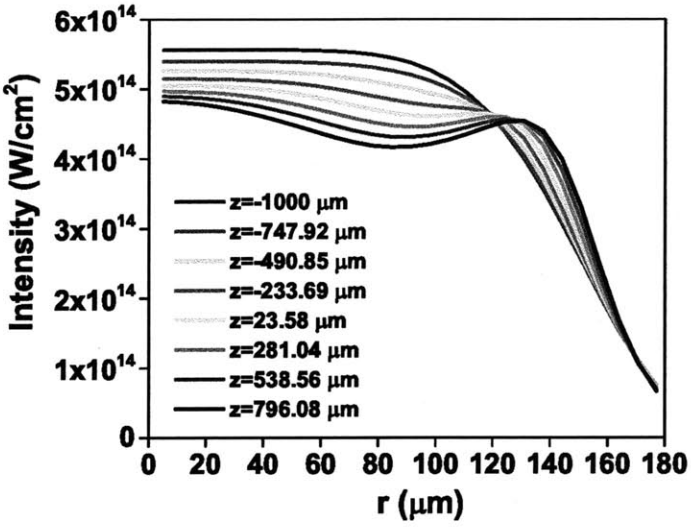

Figure 7-12: Supergaussian pulse as a function of radius r for $t = 0$ as it propagates along z.

In Figure 7-13 is shown the peak intensity at $t = 0$ when a 10 mJ, 35 fsec, 2 μm drive wavelength and 177 μm beam Gaussian pulse ($n = 2$) propagates through Helium when a) only diffraction is included, b) diffraction and plasma defocusing are included and c) the electron-neutral inverse bremsstrahlung cross section is taken into account. By looking at Figure 7-13 we conclude that plasma defocusing has a dominant role. However, losses due to electron-neutral inverse bremsstrahlung have also influence. This argument is supported in Figure 7-14 where is shown the peak intensity at $t = 0$ and $r = 0$, along propagation distance z when a) only diffraction is included, b) diffraction and plasma defocusing are included and c) the electron-neutral bremsstrahlung cross section is taken into account. The green and blue curves are set by the plasma defocusing. The loss is reducing the intensity and the slope dI/dz (intensity dependence of Δk) is a larger negative number for the blue curve than the green one at the start. Thus, the initial drop of peak intensity is faster, due to inverse bremsstrahlung. Without the losses, the pulse can propagate a little bit more without the peak intensity at $t = 0$ to drop. Thus, losses due to electron-neutral bremsstrahlung play an important tole, although is the plasma defocusing that is dominating the overall trend.

We move from a Gaussian ($n = 2$) to a Supergaussian ($n = 6$) beam. A Supergaussian

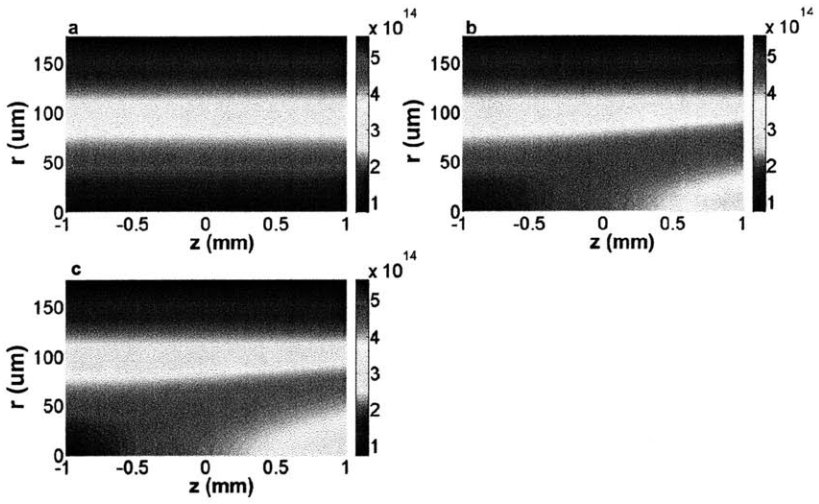

Figure 7-13: Peak intensity at $t = 0$ versus radial coordinate r and propagation z, when a 10 mJ, 35 fsec, 2 μm drive wavelength and 177 μm beam waist Gaussian pulse ($n = 2$) propagates through a Helium jet when a) only diffraction is included, b) diffraction and plasma defocusing are included and c) the electron-neutral bremsstrahlung cross section is taken into account. The colorbar shows the intensity in W/cm^2.

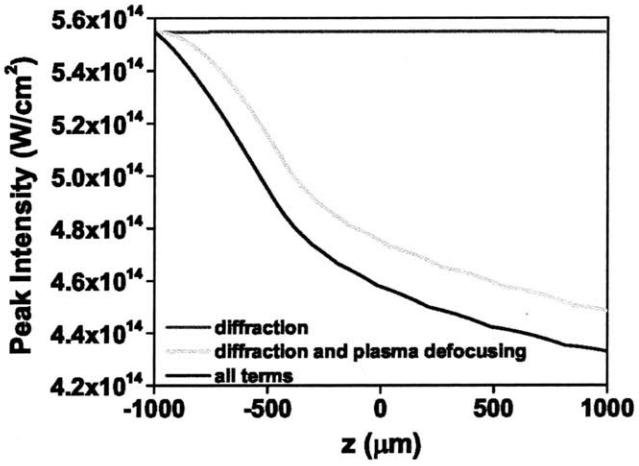

Figure 7-14: Peak intensity at $t = 0$ and $r = 0$ versus propagation z when a 10 mJ, 35 fsec, 2 μm drive wavelength and 177 μm beam waist Gaussian pulse ($n = 2$) propagates through a Helium jet when only diffraction is included (red), diffraction and plasma defocusing are included (green) and the electron-neutral bremsstrahlung cross section is taken into account (blue).

beam shape has two advantages relative to a Gaussian one:

- the Supergaussian pulse has the right intensity (the one for which $\Delta k = 0$ is preserved) for a wider range of radii
- the Supergaussian pulse experiences less diffraction and thus less of a drop of intensity as the pulse propagates (dI/dz smaller)

The diffraction length for the Supergaussian is longer and thus we expect the losses due to the electron-neutral inverse bremsstrahlung to dominate, although we work in the 10 bar pressure regime. In Figure 7-15, is shown the peak intensity at $t = 0$ when a 10 mJ, 35 fsec, 2 μm drive wavelength and 177 μm beam Supergaussian pulse ($n = 6$) propagates through a Helium gas jet when a) only diffraction is included, b) diffraction and plasma defocusing are included and c) the electron-neutral bremsstrahlung cross section is taken into account. Losses due to electron-neutral inverse bremsstrahlung are dominant and stronger than the $n = 2$ case. Thus, moving to a Supergaussian beam shape for 10 bar pressure does not help a lot. It would help for lower pressures. In Figure 7-16 is shown the peak intensity at $t = 0$ and $r = 0$ along propagation distance z when a) only diffraction is included, b) diffraction and plasma defocusing are included and c) the electron-neutral inverse bremsstrahlung cross section is taken into account. It is evident that losses play a dominant role.

Comparing $n = 2$ with $n = 6$ case, diffraction for $n = 6$ is weaker and thus losses dominate the initial drop of peak intensity. The same behavior (dominance of losses) is also observed for $n = 10$ (Figures 7-17 and 7-18).

In Figure 7-19 is shown the peak intensity at $t = 0$ and $r = 0$ for the different beam shapes. Initially everything drops along the rate that we would expect due to the loss, but in $n = 2$ case diffraction sets in quickly and power drops. As we move from $n = 2$ to $n = 6$ and then to $n = 10$ cases the initial slope is the same. It is really important to understand how long is the region that reasonable Δk at the start of propagation can be achieved and the losses are really important in order to appreciate what is happening.

Comparing the HHG efficiencies for the three cases (Figure 7-20) we conclude that there is a large increase in efficiency when we move from a Gaussian ($n = 2$) to a Supergaussian

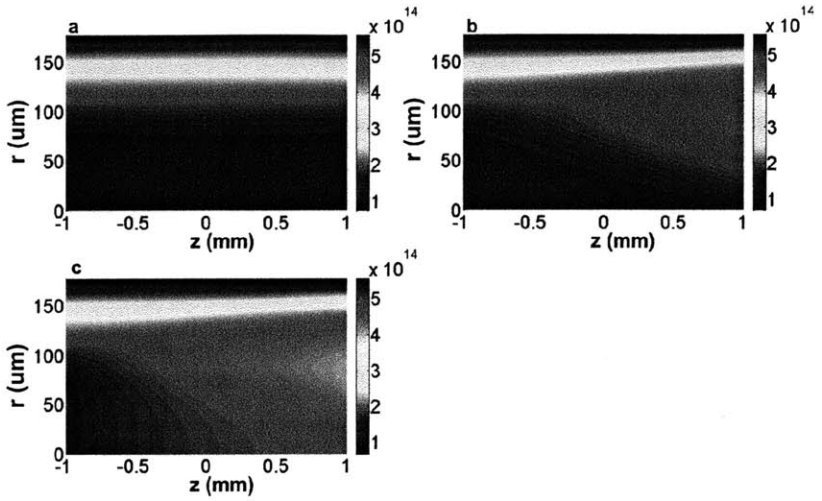

Figure 7-15: Peak intensity at $t = 0$ versus radial coordinate r and propagation z when a 10 mJ, 35 fsec, 2 μm drive wavelength and 177 μm beam waist Gaussian pulse ($n = 6$) propagates through a Helium jet when a) only diffraction is included, b) diffraction and plasma defocusing are included and c) the electron-neutral bremsstrahlung cross section is taken into account. The colorbar shows the intensity in W/cm^2.

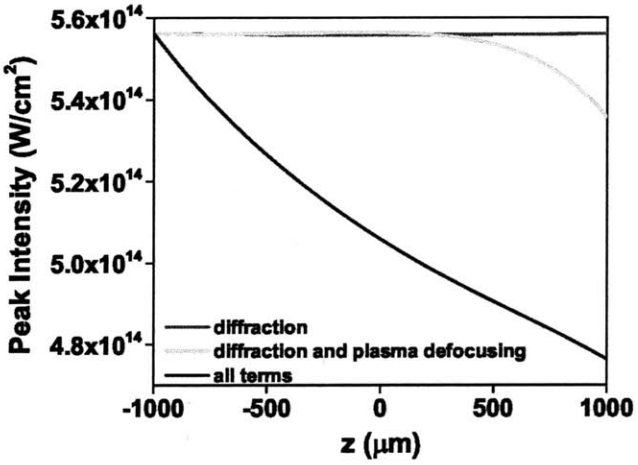

Figure 7-16: Peak intensity at $t = 0$ and $r = 0$ versus propagation z when a 10 mJ, 35 fsec, 2 μm drive wavelength and 177 μm beam waist Gaussian pulse ($n = 6$) propagates through a Helium jet when only diffraction is included (red), diffraction and plasma defocusing are included (green) and the electron-neutral bremsstrahlung cross section is taken into account (blue).

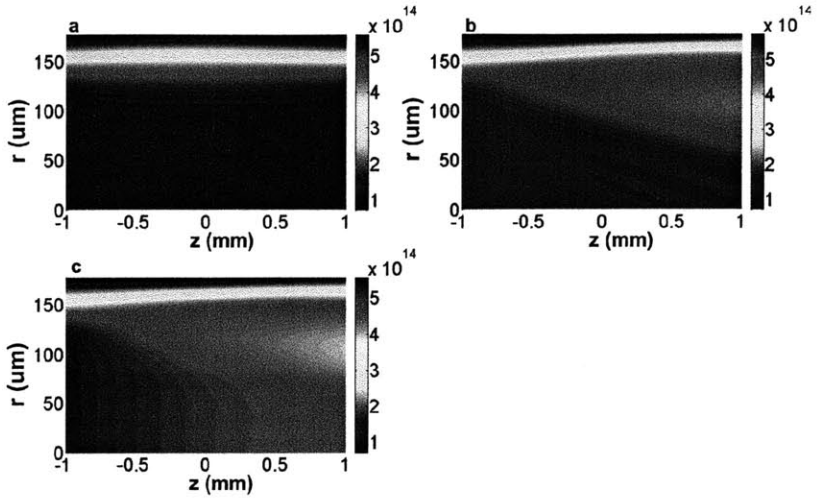

Figure 7-17: Peak intensity at $t = 0$ versus radial coordinate r and propagation z when a 10 mJ, 35 fsec, 2 μm drive wavelength and 177 μm beam waist Gaussian pulse ($n = 10$) propagates through a Helium jet when a) only diffraction is included, b) diffraction and plasma defocusing are included and c) the electron-neutral bremsstrahlung cross section is taken into account. The colorbar shows the intensity in W/cm^2.

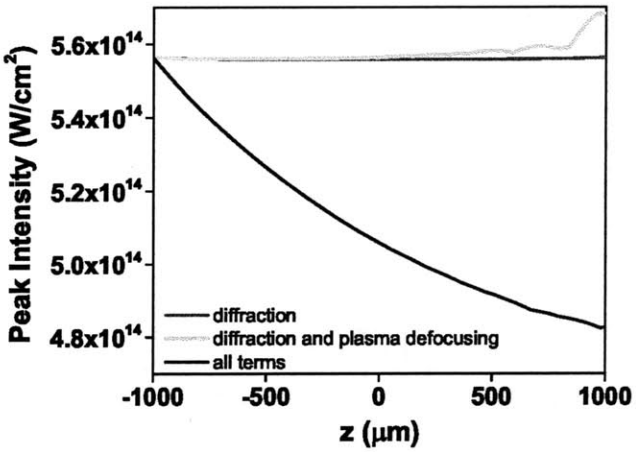

Figure 7-18: Peak intensity at $t = 0$ and $r = 0$ versus propagation z when a 10 mJ, 35 fsec, 2 μm drive wavelength and 177 μm beam waist Gaussian pulse ($n = 10$) propagates through a Helium jet when only diffraction is included (red), diffraction and plasma defocusing are included (green) and the electron-neutral bremsstrahlung cross section is taken into account (blue).

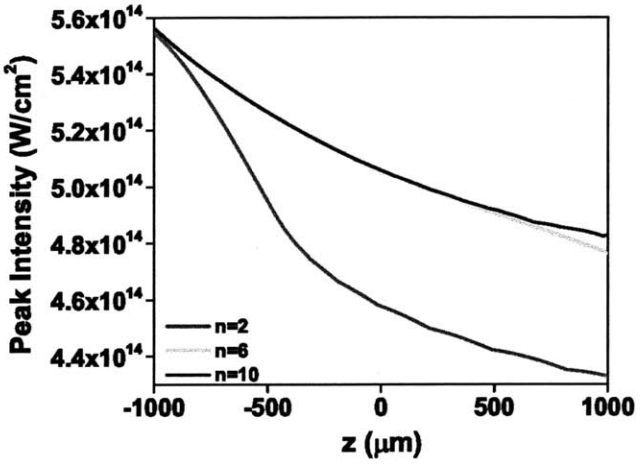

Figure 7-19: Peak intensity at $t = 0$ versus radial coordinate r and propagation z when a 10 mJ, 35 fsec, 2 μm drive wavelength and 177 μm beam waist laser pulse propagates through a Helium jet for $n = 2$ (red), $n = 6$ (green) and $n = 10$ (blue) Supergaussian beam shape.

($n = 6$) beam shape and a smaller one between $n = 6$ and $n = 10$. Moving from $n = 2$ to $n = 6$ we have advantage one (right intensity for a wide range of r) and a little bit of 2 (diffraction is slower), but already at $n = 6$ advantage two is mitigated by the losses. Moving from $n = 6$ to $n = 10$ we have just advantage one.

The efficiency gets higher for higher Supergaussian order n, since as we go to higher n there is a wider region over radius r, where there is the proper ionization probability to achieve phase matching (Figure 7-21). This proper ionization probability is depicted in white color and we can see that the higher the n the longer is the region over r that this ionization level is achieved.

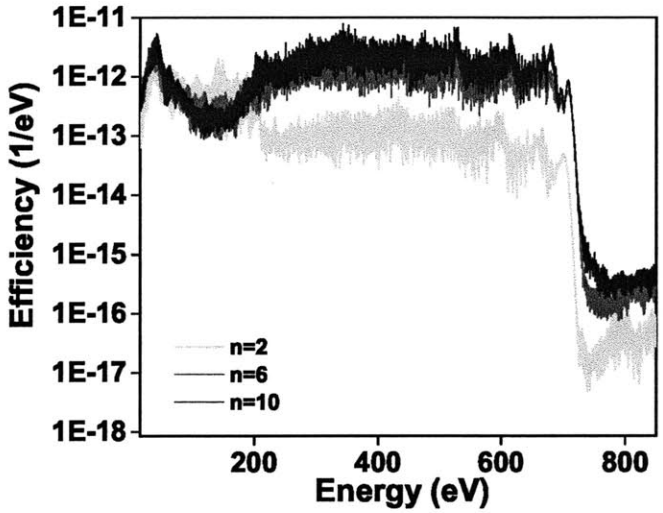

Figure 7-20: HHG efficiency in Helium for a 10 mJ, 35 fsec, 2 μm drive wavelength and 177 μm beam waist laser pulse for $n = 2$ (red), $n = 6$ (green) and $n = 10$ (blue) Supergaussian beam shape.

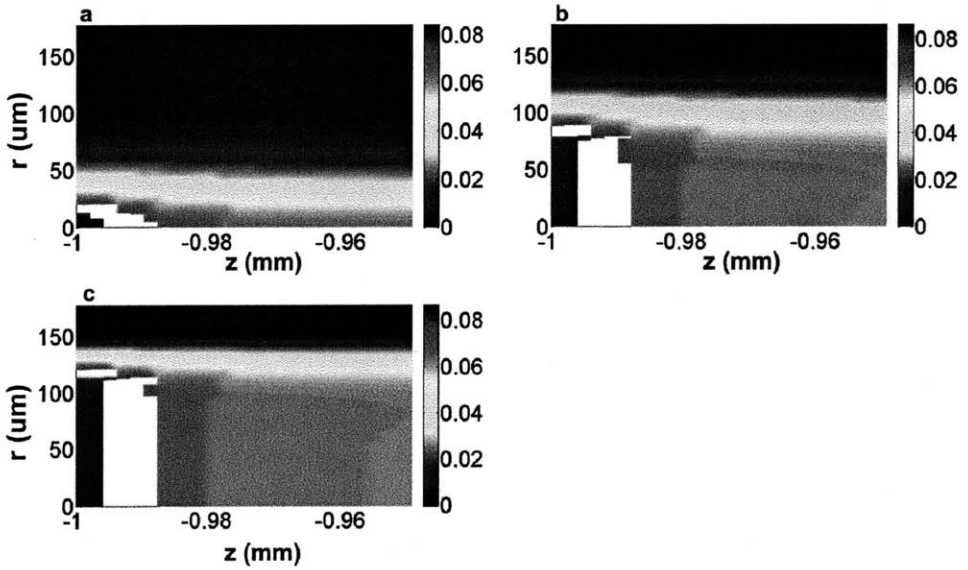

Figure 7-21: Ionization probability at $t = 0$ versus radial coordinate r and propagation z when a 10 mJ, 35 fsec, 2 μm drive wavelength and 177 μm beam waist laser pulse propagates through a 2 mm Helium jet for a) $n = 2$, b) $n = 6$ and c) $n = 10$ Supergaussian beam shape. The white region in each place shows the region over which ionization level for $\Delta k = 0$ is achieved. The colorbar is in %

7.4.2 Gaussian Pulse with Larger Beam Waist

Another way to reduce the effect of diffraction and consequently of plasma defocusing is by increasing the beam waist of the Gaussian pulse. The larger is the beam waist the smaller is the effect of diffraction.

In Figure 7-22 is shown the peak intensity versus radial coordinate r and propagation z at $t = 0$, when a Gaussian pulse with peak intensity $5.56 \cdot 10^{14}$ W/cm^2, duration 35 fsec, 2 μm drive wavelength propagates through a 2 mm Helium gas jet, when the pulse energy is 1.1 mJ with beam waist 58.73 μm (Figure 7-22.a and 7-22.d), 10 mJ with beam waist 177 μm (Figure 7-22.b and 7-22.e) and 100 mJ with beam waist 559.97 μm (Figure 7-22.c and 7-22.f). In the upper panel (subplots a, b and c) the electron-neutral inverse bremsstrahlung is not taken into account, while in the lower panel (subplots d, e, and f) is taken into account.

For energy 1 mJ the cases with and without inverse bremsstrahlung are identical with strong defocusing. Moving to energy 10 mJ the plot of peak intensity with and without inverse bremsstrahlung are not quite identical but still not very different, with the intensity dropping faster at the begin of the medium when the inverse bremsstrahlung is included. Moving to 100 mJ, plasma defocusing is gone away and intensity is maintained for longer distance. Diffraction hurts less, but the role of inverse bremsstrahlung is more significant, with the drop of intensity at the begin of the medium being significant, when inverse bremsstrahlung is taken into account (compare the drop of intensity at the begin of the medium for Figures 7-22.c and 7-22.f) and thus we cannot do better as we move to higher energies. As soon as defocusing is limited, the role of the electron-neutral inverse bremsstrahlung becomes crucial.

In Figure 7-23 are shown the efficiencies for the three different energies. The higher is the energy and consequently the beam waist, the higher is the efficiency.

As we go to higher energy and larger beam waist the effect of diffraction is mitigated and thus a longer coherence length is maintained. However, as soon as the plasma defocusing starts to decrease, the electron-neutral inverse bremsstrahlung starts to increase and begins limiting how long the coherence length is maintained.

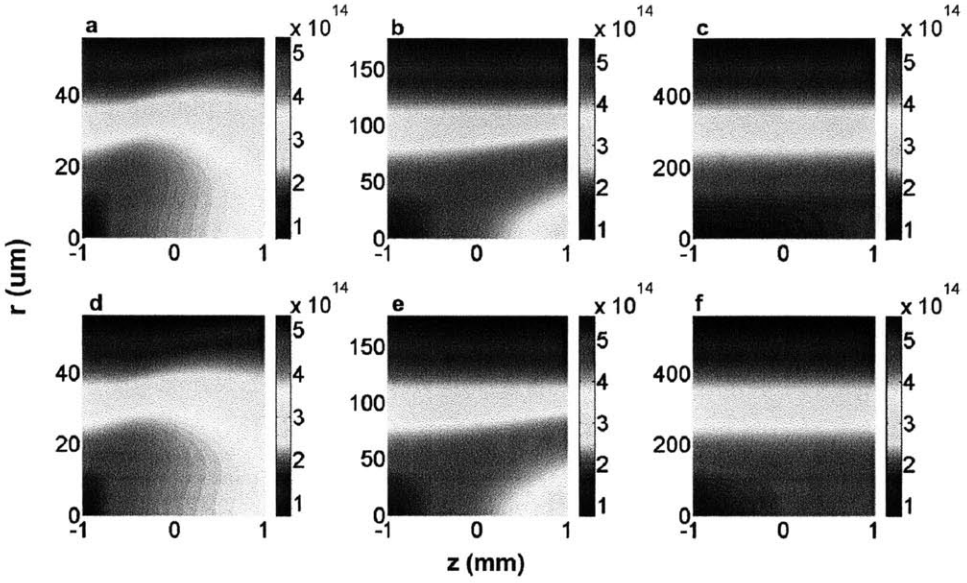

Figure 7-22: Peak intensity versus radial coordinate r and propagation z at $t = 0$, when a Gaussian pulse with peak intensity $5.56 \cdot 10^{14}$ W/cm^2, duration 35 fsec, 2 μm drive wavelength propagates through a 2 mm Helium gas jet for a) energy 1.1 mJ and beam waist 58.73 μm without inverse bremsstrahlung, b) energy 10 mJ and beam waist 177 μm without inverse bremsstrahlung, c) energy 100 mJ and beam waist 559.97 μm without inverse bremsstrahlung, d) energy 1.1 mJ and beam waist 58.73 μm with inverse bremsstrahlung, e) energy 10 mJ and beam waist 177 μm with inverse bremsstrahlung, f) energy 100 mJ and beam waist 559.97 μm with inverse bremsstrahlung.

Comparing the approach of using Supergaussian pulses with the one of using Gaussian pulses with larger beam waists, we see that in the latter approach we do not have the advantage of the Supergaussian where more points in the radial coordinate are contributing. When we go to a larger beam waist we only have the benefit of having a longer diffraction length, but as soon as the plasma defocusing becomes less significant, the electron-neutral inverse bremsstrahlung becomes important.

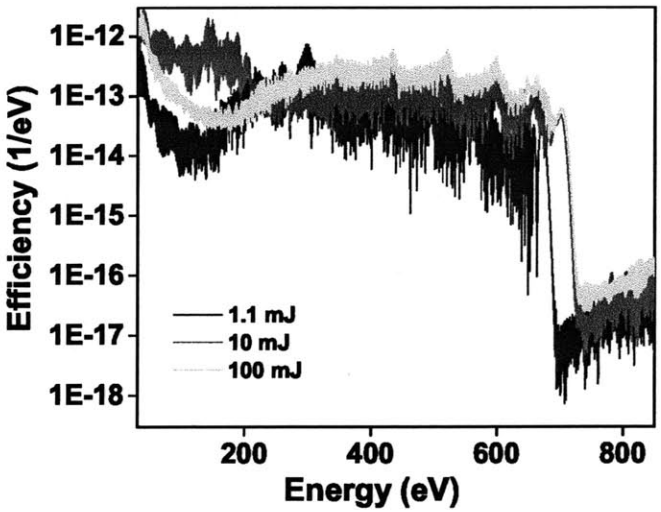

Figure 7-23: HHG efficiency for Gaussian pulse with peak intensity $5.56{\cdot}10^{14}$ W/cm^2, duration 35 fsec, 2 μm drive wavelength propagates through a 2 mm Helium gas jet for a) energy 1.1 mJ with beam waist 58.73 μm (blue), b) energy 10 mJ with beam waist 177 μm (red), c) energy 100 mJ with beam waist 559.97 μm (green).

Chapter 8

Conclusions and Future Directions

In this thesis we did a study for the theoretical optimization of HHG efficiency. This study can be summarized in three parts:

- Derivation of a semi-analytical formula for the computation of the conversion efficiency into a single harmonic, using an 1-D model, and comparison of the theoretical results with experimental ones
- Extension of the model to three dimensions and study of the influence of spatial effects, like plasma defocusing and electron-neutral inverse bremsstrahlung to the driving and harmonic fields
- Investigation of ways to mitigate the effect of plasma defocusing by using Supergaussian beam shapes and using Gaussian pulses with larger beam waists

We developed a semi-analytical model for the computation of the conversion efficiency into a single harmonic for the plateau and cutoff regions. This model is one dimensional, uses the Three Step Model for the calculation of the single atom response in the single active electron approximation and takes laser and material parameters and phase matching effects into account. The analytical formula shows that the efficiency per harmonic scales with ω_0^6 at the plateau and ω_0^5 at the cutoff region of the spectrum. We compared the results from our theory with experimental results at 400 and 800 nm showing excellent agreement. The efficiencies at 400 nm were 1-2 orders of magnitude higher than the ones at 800 nm verifying

the formula prediction. In addition, we investigated the effect of the interference between short and long trajectories on the spectra. We also studied two different ionization models, the ADK and the Yudin-Ivanov and we showed that the Yudin-Ivanov model, which includes both tunneling and multiphoton ionization, gives more accurate results especially for short drive wavelengths.

We extended the 1-D model to 3-D and we studied in detail the effect of plasma defocusing and electron-neutral inverse bremsstrahlung. We did this study in order to generate radiation in the water window region of the spectrum by using driver pulses with 2 μm drive wavelength. We showed that within the range of pressures one might choose for performing the experiment, at low pressures (0.1-1 bar) diffraction enhanced by plasma defocusing is the dominant limitation, at high pressures (>20 bar) loss due to electron-neutral inverse bremsstrahlung is the main limitation and there is an intermediate regime of medium pressures (1-20 bar) where both diffraction effects and loss due to electron-neutral inverse bremsstrahlung have an effect. These two effects do not allow phase matching to be maintained for long distance, as the driver pulse propagates through the medium, resulting in short coherence length and consequently to low efficiencies.

Finally, we explored ways to mitigate the effect of plasma defocusing by using Supergaussian pulses and Gaussian pulses with large beam waists. Moving from Gaussian to Supergaussian pulses has the advantage of having the right intensity to achieve phasematching for a wide range of r and also of experiencing less diffraction. Using Gaussian pulses with larger beam waists has the advantage of mitigating the effect of diffraction and maintaining a longer coherence length. Both approaches to mitigate plasma defocusing showed increase in efficiency.

As directions for future research, it would be important to understand better the effect of dipole phase on phase mismatch and how it could be used for our advantage in order to counteract with the Gouy phase shift. This would result in concentrating only on neutral and plasma terms of plasma defocusing which can be treated easier. In addition, it would be very useful to quantify how the ratio of medium length to diffraction length scales with

pressure. This would help us understand how long the phase matching can be maintained. Finally, a study on the spatiotemporal effects and on the quality of the generated attosecond pulses would be crucial.

The contribution of the work presented in this thesis is twofold. It reduces the computational complexity of calculating HHG efficiencies and helps us appreciate the various spacial effects. We strongly believe that this work can help the research community to develop tools for an optimization study of HHG efficiency for making useful EUV sources.

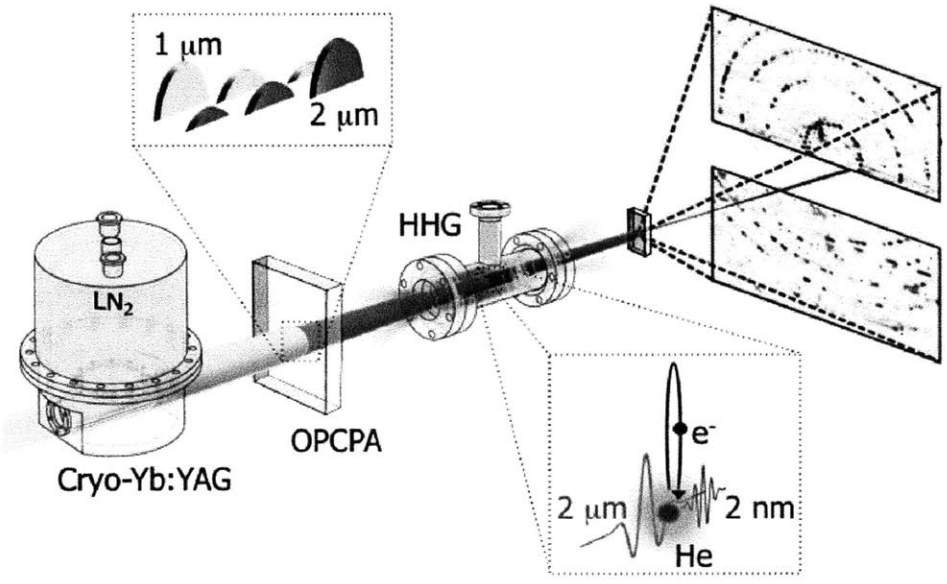

Appendix A

Dynamics of Actively Mode-locked Quantum Cascade Lasers

Quantum Cascade Lasers (QCLs) are semiconductor lasers that emit in the mid- to far-infrared region of the electromagnetic spectrum. QCLs were first demonstrated by Federico Capasso and his group at Bell Laboratories in 1994 [59] and they have become the most prominent and compact coherent light source in the mid-infrared. While conventional semiconductor lasers are bipolar devices and have an upper state lifetime ranging from hundreds of psec up to nsec, QCLs are unipolar devices with an upper state lifetime that is in the few psec range. In QCLs, the emission wavelength, the gain spectrum and the carrier transport characteristics can be engineered over a wide range of values.

Figure A-1 depicts an energy diagram showing two stages of a QCL. Each stage consists of an active region and an electron injector. The moduli squared of the relevant wavefunctions are also shown. Electrons are injected from left to right and emit a laser photon at each stage as they cascade down the structure. The electron injectors are composed of quantum wells with very thin barriers. As a result, electronic states extend over many layers and form narrow energy minibands separated by minigaps.

An electric field is applied so that electrons are injected from the minibands ground state g into the upper state of a laser transition level 3 of the active region. The thinnest well in the

active region enhances tunneling of the electron from the injector into the upper state. For laser action to occur, the electron population in state 3 must exceed that of state 2. So the relaxation time for the transition from state 3 to state 2 must exceed the electron lifetime in state 2. The relaxation time between 2 states is largely controlled by the emission of optical phonons. Increasing the state separation, increases the relaxation time. To maximize the population inversion, the energy separating states 2 and 1 is designed to be equal to the phonon energy, so that electrons in states 2 quickly go into level 1. To prevent accumulation of electrons in level 1 the exit barrier of the active region is made thin, which allows rapid tunneling into a miniband in the adjacent injector.

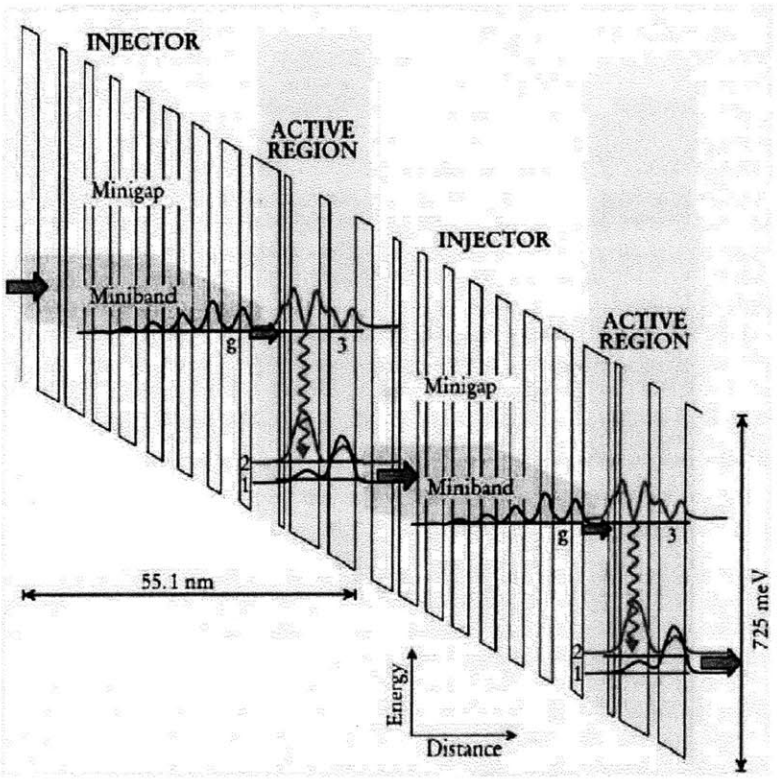

Figure A-1: Energy diagram showing two stages of a QCL.

A.1 Introduction

Short pulse generation from QCLs emitting in the mid-infrared region (3.5-20 μm) could serve many applications ranging from time-resolved spectroscopy [60,61], and nonlinear frequency conversion [8,62,63] to high-speed free space communication [64] and frequency metrology [65].

The gain bandwidth of QCLs is large enough to potentially generate sub-picosecond mid-infrared laser pulses due to the flexibility offered by band structure engineering. The most common technique for ultrashort pulse generation is mode locking, in which the longitudinal modes of the cavity are phaselocked either by an internal mechanism (passive mode locking) or by an external (active mode locking). However, short pulse generation from QCLs by mode locking is difficult due to the fast gain recovery time [66,67]. In intersubband transitions (i.e. transitions between quantized conduction band states in semiconductor quantum wells), the carrier relaxation time is very fast due to optical phonon scattering. As a result, the upper state lifetime in QCLs is typically one order of magnitude smaller than the roundtrip time, 40-60 psec, of typical few mm long laser structures [66,67]. Usually, this situation prevents the occurrence of mode locking, i.e. stable pulse formation. The reason is, that the gain fully recovers before the next pulse arrives or even immediately after the pulse if the gain is fast enough, which leads to less amplification of the peak of the pulse than its wings. Due to this process the pulse lengthens in time and the laser approaches continuous wave (cw) lasing. On the other hand, if the gain recovery time is longer than the cavity roundtrip time, the gain saturates with the average power in the laser cavity and does not shape the pulse significantly (Figure A-2). Therefore, most recently, QCLs with long upper state lifetime have been fabricated by implementing a superdiagonal gain structure. Upper state lifetimes of 50 psec, similar to the cavity roundtrip time, have been achieved. Using such structures, an actively mode-locked QCL [68,69] that produced stable and isolated picoseconds pulses, as confirmed by interferometric autocorrelation measurements, was demonstrated. Stable operation with these devices was obtained by current modulation of only a short section of the waveguide, while the whole waveguide was biased slightly above threshold.

In this work, first the impact of upper state lifetime and pumping level on pulse formation is discussed without taking spatial hole burning into account. Then the role of spatial hole burning (SHB) in pulse shaping, destabilization of mode locking and interaction with fast gain recovery and saturation is clarified, beyond what has been discussed previously in [69,70], by extensive numerical simulations. SHB significantly reduces the pulse duration by supporting broadband multimode operation. However, it leads to pulse instabilities and non stationary pulse generation from the laser.

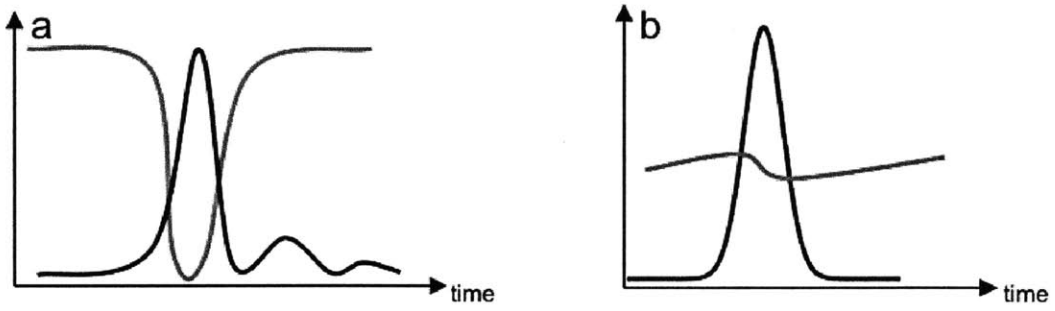

Figure A-2: Intensity (black line) and inversion (red line) for a) fast gain recovery time and b) slow gain recovery time.

A.2 Prior Work on Multimode Regimes in QCLs

There are several previous works in which multimode regimes in QCLs were observed [64,71–73]. In [71] self mode locking of CW pumped QCLs was claimed. The lasers were emitting broadband optical spectra over a wide range of DC pumping levels. In the photocurrent spectrum a strong, stable and narrow (less than 100 kHz) peak was observed, which indicated long term coherence of phase relationships between the longitudinal modes. However, no autocorrelation data were reported from which one could infer the formation of a stable train of ultrashort pulses separated by the cavity roundtrip time.

In [64] active mode locking in QCLs, by modulating the laser current at the cavity roundtrip frequency, was pursued. Again, evidence of mode locking was deduced from the

measured broadband optical spectra, as well as from the power spectra of the photocurrent. When the detuning between the driving frequency and the roundtrip frequency was large, only one mode was lasing. As the detuning was decreased more and more modes were lasing and a narrow beat note at roundtrip cavity frequency appeared. Information about the temporal profile of the generated pulses and proof for true short pulse generation can be obtained with second order autocorrelation measurements. Due to the lack of second order autocorrelators in the mid-infrared at that time, there was no direct evidence that the circulating waveform was consisting of a train of periodic isolated pulses with a stable steady state pulse shape.

Once autocorrelation techniques based on two photon absorption quantum well infrared photodetectors (QWIPs) [74, 75] became available, it was discovered that the wideband multimode operation in QCLs is due to phenomena, such as spatial hole burning and the Risken-Nummedal-Graham-Haken (RNGH) instability [70, 76]. Recently, it was proposed that self-induced transparency (SIT) together with a fast saturable absorber may be used to passively mode lock QCLs [77].

A.3 Device Model and Modulation Scheme

The actively mode locked QCL, which we will study in the following is schematically depicted in Figure A-3.a. A detailed description of a specific device can be found in [69]. The laser cavity is formed by two semiconductor/air interfaces, which shall be located at $z = 0$ and $z = L$, where L is the cavity length. The cavity is divided into a short and a long section (Figure A-3.b). Both sections are assumed to be equally and continuously pumped (DC pumping) with a current density $J = p \times J_{th}$, where J_{th} denotes the threshold current density and the pump parameter p shows how many times the laser is pumped above threshold.

Active mode locking is achieved by sinusoidal modulation of the pump current injected into the short, electrically isolated, waveguide section with the roundtrip frequency of the passive cavity. The modulation is supposed to drive a large number of longitudinal modes

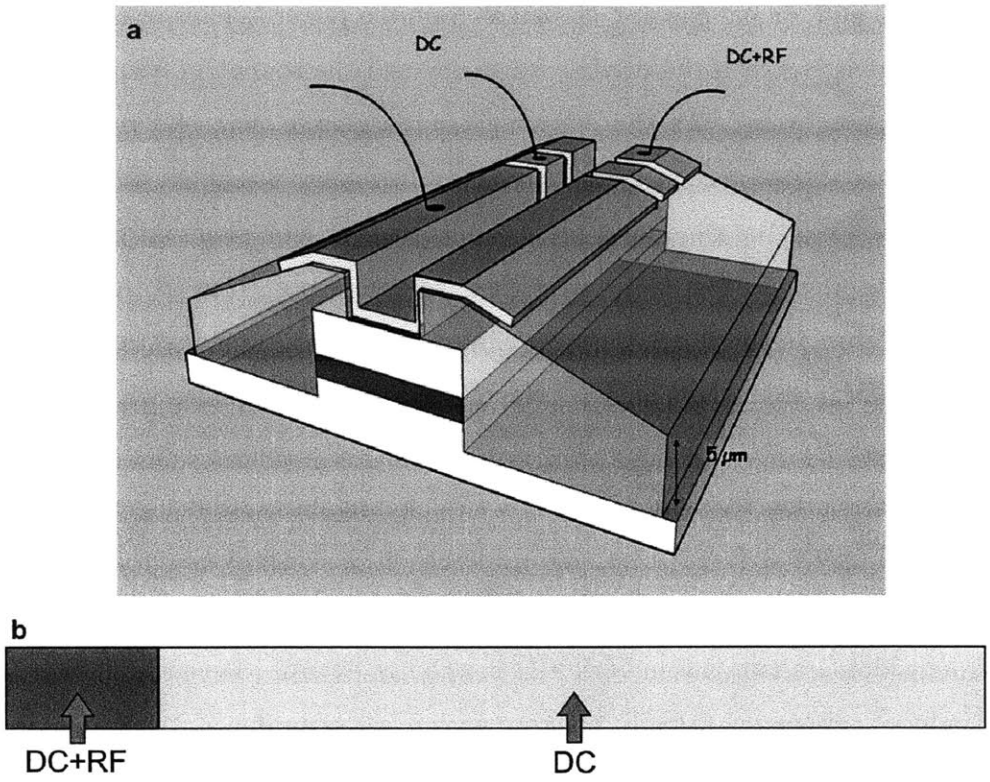

Figure A-3: a) Device used in the experiment, b) Modulation scheme for the actively mode locked QCL. The cavity is in total 2.6 mm long and the short modulator section at the beginning of the cavity is 240 μm long.

above threshold by creating modulation sidebands resonant with neighboring modes. The pump current of the small section is then given by $J = J_{th} \times [p + msin(2\pi f_R t)]$, where m is the modulation amplitude relative to threshold.

The modulation of the injection current into the short section leads to temporal variation of the roundtrip gain that a pulse can experience, favoring pulsed operation. The common approach to achieve active mode locking is by periodic modulation of the intracavity losses. Here, we modulate the gain. The short section of the cavity acts as a gain modulator, and the long section is pumped to transparency or to slight net gain, helping to compensate the other losses in the laser cavity.

A.4 Numerical Model of QCLs

The dynamics of a QCL can be described by a three level model [78] as it is shown in Figure A-4.a. It assumes that all QCL stages are identical and that laser action occurs between levels 2 and 1, the upper and lower states of the laser transition. Level 0 corresponds to the superlattice which connects to the next QCL stage, which is again described by the upper laser level 2. The current density J driven through the device by an external voltage acts as the pump current density from level 0 to level 2. T_{21} is the lifetime of the upper level, T_{10} is the lifetime of the lower laser level, that couples to the superlattice. In reality, there is also a superlattice transport time, T_{SL}, that describes the time it takes for the carriers to travel between different stages, which we neglect here. The rate equations for the 3-level system shown in Figure A-4.a reads

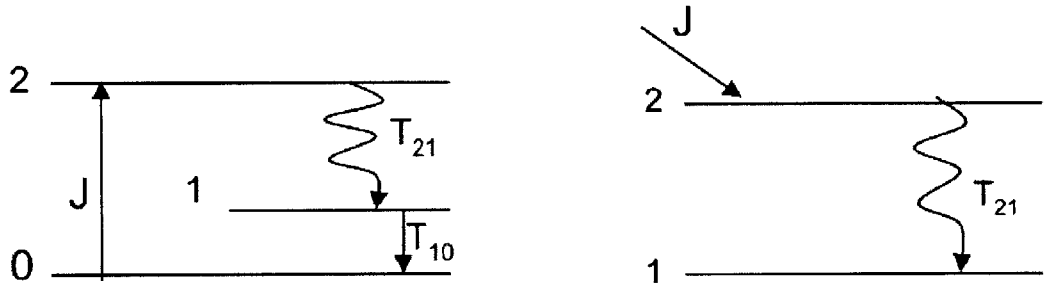

Figure A-4: a) Three-level system which describes QCL dynamics, b) Open two-level model that we use in the simulations.

$$\frac{dN_2}{dt} = J - \sigma I_{ph}(N_2 - N_1) - \frac{1}{T_{21}}N_2 \tag{A.1}$$

$$\frac{dN_1}{dt} = \sigma I_{ph}(N_2 - N_1) + \frac{1}{T_{21}}N_2 - \frac{1}{T_{10}}N_1 \tag{A.2}$$

$$\frac{dN_0}{dt} = -J + \frac{1}{T_{10}}N_1 \tag{A.3}$$

where N_2, N_1 and N_0 are the population sheet densities of levels 2, 1 and 0 respectively, J is the pump current density from level 0 to the upper lasing level 2, σ is the cross section for stimulated emission between levels 2 and 1 and I_{ph} is the photon flux at the transition frequency f_{21}. If the relaxation rate $1/T_{10}$ is very large in comparison with the stimulated and spontaneous transition rate from level 2 to 1, which is $\sigma I_{ph}(1 - N_1/N_2) + 1/T_{21}$, then level 1 will stay empty at all times, i.e. $N_1 = 0$. This is especially the case in the laser here, since it is never pumped far above threshold and the ratio $T_{21}/T_{10} \approx 100$. Thus even for sub-picosecond short pulses the stimulated emission rate would never exceed the decay rate $1/T_{10}$, which would lead to significant build-up of population in the lower laser level.

Assuming that the lower lasing level stays empty, we can describe the QCL dynamics by an open two-level model (Figure A-4.b) for simplicity. The rate equations for the 2-level system shown in Figure A-4.b read

$$\frac{dN_2}{dt} = J - \sigma I_{ph} N_2 - \frac{1}{T_{21}} N_2 \tag{A.4}$$

$$N_1 = 0 \tag{A.5}$$

The population inversion in the open two-level model is effectively the upper state population. The gain recovery time in the two-level model is then equal to the upper state lifetime T_{21} and the pump current density fills the upper laser state 2 at a given rate determined by the injected current density. The two-level model does not include the superlattice transport dynamics since it is derived from the three level model (Eq. A.1-A.3) which also does not involve this transport and this may be one reason for some of the remaining discrepancies between the theoretical and experimental results.

A.5 Maxwell-Bloch Equations

To describe the interaction of the laser field with the gain medium, we expand the two level rate equations to full Maxwell-Bloch Equations [70], that also take the coherent interaction

between the field and the medium into account. The dynamics of polarization and inversion of the gain medium is described by the Bloch equations (Eq. A.6-A.7) and the pulse propagation through the gain medium located in the Fabry Perot cavity is described by the wave equation (Eq. A.8). The electric field propagates in both directions resulting in standing waves.

$$\partial_t \rho_{ab} = i\omega\rho_{ab} + i\frac{dE}{\hbar}\Delta - \frac{\rho_{ab}}{T_2} \tag{A.6}$$

$$\partial_t \Delta = \lambda - 2i\frac{dE}{\hbar}(\rho^*_{ab} - \rho_{ab}) - \frac{\Delta}{T_1} + D\frac{\partial^2 \Delta}{\partial z^2} \tag{A.7}$$

$$\partial_z^2 E - \frac{n^2}{c^2}\partial_t^2 E = \frac{Nd}{\epsilon_0 c^2}\partial_t^2(\rho_{ab} + rho^*_{ab}) \tag{A.8}$$

where ρ_{ab} is the off-diagonal element of the density matrix, $\Delta = \rho_{bb} - \rho_{aa}$ is the population inversion, ω is the resonant frequency of the two-level system, d is the dipole matrix element of the laser transition, D is the diffusion coefficient, E is the electric field, N is the number of two-level systems per unit volume, n is the background refractive index, T_1 is the upper state lifetime, T_2 is the dephasing time and λ is the pumping rate, that is directly proportional to the injection current J in the rate equations. In the model, we modulate the gain in the short section via the pump parameter $\lambda = \lambda_{th} \times [p + msin(2\pi f_R t)]$ and in the long section $\lambda = \lambda_{th} \times p$. The last term in Eq. A.7 accounts for spatial diffusion of the inversion, i.e. of electrons in the upper laser level along the plane of the layers.

The waves traveling in the two directions are coupled as they share the same gain medium. This gives rise to SHB: the standing wave formed by a cavity mode imprints a grating in the gain medium through gain saturation. As a result, other modes may become more favorable for lasing and multimode operation is triggered.

We make the following ansatz for the electric field, the polarization and the inversion:

$$E(z,t) = \frac{1}{2}\left[E^*_+(z,t)e^{-i(\omega t - kz)} + E_+(z,t)e^{i(\omega t - kz)}\right] + \frac{1}{2}\left[E^*_-(z,t)e^{-i(\omega t + kz)} + E_-(z,t)e^{i(\omega t + kz)}\right] \tag{A.9}$$

$$\rho_{ab}(z,t) = \eta_+(z,t)e^{-i(\omega t - kz)} + \eta_-(z,t)e^{i(\omega t + kz)} \tag{A.10}$$

$$\Delta(z,t) = \Delta_0(z,t) + \Delta_2(z,t)e^{2ikz} + \Delta_2^*(z,t)e^{-2ikz} \tag{A.11}$$

where $k \equiv \omega n/c$. The + and - subscripts label the two directions of propagation. E and η are the slowly varying envelopes in time and space of the electric field and the polarization, respectively. The spatially dependent inversion is written as a sum of three terms, where Δ_0 is the average inversion and Δ_2 is the amplitude of the inversion grating. Δ_0 and Δ_2 vary slowly in time and space.

We substitute Eq. A.9-A.11 into Eq. A.6-A.8, and perform the slowly varying envelope approximation obtaining the following set of equations [13]:

$$\frac{n}{c}\partial_t E_\pm = \mp\partial_z E_\pm - i\frac{Ndk}{\epsilon_0 n^2}\eta_\pm - lE_\pm \tag{A.12}$$

$$\partial_t \eta_\pm = \frac{id}{2\hbar}\left(\Delta_0 E_\pm + \Delta_2^\mp E_\mp\right) - \frac{\eta_\pm}{T_2} \tag{A.13}$$

$$\partial_t \Delta_0 = \lambda + \frac{id}{\hbar}\left(E_+^*\eta_+ + E_-^*\eta_- - c.c.\right) - \frac{\Delta_0}{T_1} \tag{A.14}$$

$$\partial_t \Delta_2^\pm = \pm i\frac{d}{\hbar}\left(E_+^*\eta_- - \eta_+^* E_-\right) - \left(\frac{1}{T_1} + 4k^2 D\right)\Delta_2^\pm \tag{A.15}$$

For compact notation we introduced: $\Delta_2^+ \equiv \Delta_2$ and $\Delta_2^- \equiv \Delta_2^*$. $\left(\Delta_2^+\right)^* \equiv \Delta_2^-$. The last term in the equation for the electric field represents the waveguide losses. The model assumes fixed waveguide losses, l. In addition to the waveguide losses there are also losses upon reflection from the waveguide facet, which are in the case considered here 53% on each end of the laser due to the reflection from the semiconductor air interface, which is not contained in the propagation equations (Eq. A.12-A.15), but included in the simulation. In fact the low facet reflectivity is the major source of loss in this laser so that other small loss variations in the device due to changes in the operating conditions are expected to be of minor importance and can be safely neglected. In contrast to [70], we do not include any effective saturable absorber effects due to potential Kerr-Lensing, since we compare the simulations later with experimental results from devices with a wide ridge (8-20 μm), where such effects are greatly reduced as discussed in [70].

For simulation purposes, i.e. elimination of noncritical model parameters, we normalize the field with respect to the dipole matrix element, i.e. Rabi frequency, and correspondingly polarization, inversion, inversion grating and pumping as follows: $\tilde{E} \equiv \frac{Ed}{\hbar}$, $\tilde{\eta} \equiv \frac{Nd^2k}{\hbar\epsilon_0 n^2}$, $\tilde{\Delta}_0 \equiv \frac{Nd^2k}{\hbar\epsilon_0 n^2}\Delta_0$, $\tilde{\Delta}_2 \equiv \frac{Nd^2k}{\hbar\epsilon_0 n^2}\Delta_2$ and $\tilde{\lambda} \equiv \frac{Nd^2k}{\hbar\epsilon_0 n^2}\lambda$. The equations transform to

$$\frac{n}{c}\partial_t \tilde{E}_\pm = \mp\partial_z \tilde{E}_\pm - i\tilde{\eta}_\pm - l\tilde{E}_\pm \tag{A.16}$$

$$\partial_t \tilde{\eta}_\pm = \frac{i}{2}\left(\tilde{\Delta}_0 \tilde{E}_\pm + \tilde{\Delta}_2^\mp \tilde{E}_\mp\right) - \frac{\tilde{\eta}_\pm}{T_2} \tag{A.17}$$

$$\partial_t \tilde{\Delta}_0 = \tilde{\lambda} + i\left(\tilde{E}_+^* \tilde{\eta}_+ + \tilde{E}_-^* \tilde{\eta}_- - c.c.\right) - \frac{\tilde{\Delta}_0}{T_1} \tag{A.18}$$

$$\partial_t \tilde{\Delta}_2^\pm = \pm i\left(\tilde{E}_+^* \tilde{\eta}_- - \tilde{\eta}_+^* \tilde{E}_-\right) - \left(\frac{1}{T_1} + 4k^2 D\right)\tilde{\Delta}_2^\pm \tag{A.19}$$

For ease of interpretation of the simulation results and matching of model parameters to the experimentally realized operating conditions, which are always related to the threshold pump current, we derive the threshold pumping and threshold inversion for cw-lasing. The continuous wave steady state polarization for $\tilde{E}_+ = \tilde{E}_- = \bar{\tilde{E}}$ is

$$\bar{\tilde{\eta}} = i\frac{T_2}{2}\left(\bar{\tilde{\Delta}}_0 + \bar{\tilde{\Delta}}_2\right)\bar{\tilde{E}} \tag{A.20}$$

which can be substituted in Eq. A.16. Thus for the forward propagating field we find

$$\left(\partial_z + \frac{n}{c}\partial_t\right)\bar{\tilde{E}} = \frac{T_2}{2}\left(\bar{\tilde{\Delta}}_0 + \bar{\tilde{\Delta}}_2\right)\bar{\tilde{E}} - l\bar{\tilde{E}} \tag{A.21}$$

Thus the gain is $g = T_2\left(\bar{\tilde{\Delta}}_0 + \bar{\tilde{\Delta}}_2\right)/2$. At threshold the electric field vanishes and we obtain from Eq. A.18 for the inversion $\tilde{\Delta}_0 = \tilde{\lambda}T_1$ and since there is no grating, $\tilde{\Delta}_2 = 0$. We therefore find that the small signal gain is given by $g_0 = \tilde{\lambda}T_1T2/2$. At threshold the gain is equal to the losses, thus the pumping at threshold must be $\tilde{\lambda}_{th} = 2l/T_1T_2$ and the inversion at threshold is $\tilde{\Delta}_{th} = 2l/T_2$. For the following, we normalize the plots for the inversion always with respect to the threshold inversion $\tilde{\Delta}_{th}$ for ease of interpretation.

Spatial hole burning is associated with the amplitude $\tilde{\Delta}_2$ of the inversion grating that couples the electric fields propagating along the two directions in the laser. As can be seen from Eq. A.19 the inverse lifetime of the gain grating is given by $T_g^{-1} = T_1^{-1} + 4k^2D$, i.e. it is the sum of the terms due to diffusion of the carrier density modulation and the inverse carrier lifetime, since the latter is the rate by which carriers are homogeneously injected in each volume element. SHB is strong in mid-IR QCLs since the strength of diffusion, which combats the carrier density modulation, scales with the square of the wave number k [13], which is about an order of magnitude smaller for mid-IR QCLs than for semiconductor lasers in the visible. In steady state, Eq. A.18 shows that the term $i\left(\tilde{E}_+^*\tilde{\eta}_- - \tilde{\eta}_+^*\tilde{E}_-\right)$ that drives the inversion grating in Eq. A.19 scales with $\tilde{\Delta}_0/T_1$. So, in steady state, the strength of the carrier density modulation or gain grating is $\tilde{\Delta}_2 \sim \tilde{\Delta}_0/(1+4k^2DT_1)$. In AlInAs-InGaAs heterostructures, the diffusion coefficient D is 46 cm^2/sec at 77 K and for vacuum wavelength 6.2 μm, we obtain $4k^2D = 0.2$ THz. In regular mid-IR QCLs (T1=5 psec), $4k^2D$ is roughly the same as $1/T_1$ and SHB is strong $\left(\tilde{\Delta}_2 \approx 0.5\tilde{\Delta}_0\right)$. Even for a longer upper state lifetime, such as $T_1 = 50psec$, which is the case for the superdiagonal QCL structures discussed here, the effects of SHB cannot be neglected $\left(\tilde{\Delta}_2 \approx 0.1\tilde{\Delta}_0\right)$. Due to the fast gain recovery time of QCLs, carrier diffusion can not suppress SHB, in contrast to standard semiconductor lasers.

A.6 Parameters

The parameters that stay fixed and are used in all examples in this paper, if not otherwise explicitly noted, are given in Table A.1. It is important to note, that for the QCL with superdiagonal gain structure discussed here, the roundtrip time is almost equal to the gain recovery time, T_1, a fact that enables stable mode locking as explained before.

Table A.1: Parameters used in simulations if not otherwise noted

Quantity	Symbol	Value
Gain recovery time	T_1	50 psec
Dephasing time	T_2	0.05 psec
Linear cavity loss	l	10 cm^{-1}
Roundtrip time	T_R	56 psec
Roundtrip frequency	f_R	17.86 GHz
Cavity length	L	2.6 mm
Modulator section length	L_s	0.24 mm
Facet reflectivity	R	53%

A.7 QCL Dynamics without Spatial Hole Burning

First, the steady state behavior of the laser is investigated when SHB is not included in the Maxwell-Bloch equations (i.e. $\Delta_2^{\pm} = 0$). Initially the continuous wave steady state solution of the model is determined when the current modulation is switched off. Figure A-5 shows the resulting total intracavity intensity and normalized inversion. That means, in each point of the cavity there is a forward and a backward wave and we add the intensities of both waves to the total intensity at each point. The total intensity increases slightly towards the facets of the cavity to compensate for the output coupling losses and as a result the gain is more strongly saturated at the edges than in the center of the cavity.

For completeness, Figure A-6 shows the pumping, the inversion and the intensity versus time for a point inside the short (modulated) section. The inversion does not follow the pumping current instantaneously, because the modulation frequency is close to the inverse gain recovery time (i.e $f_R = 17.86$ GHz and $1/T_1 = 20$ GHz) and as a result the inversion is delayed by almost 90 degrees compared to the pumping. Also, the gain peak does not

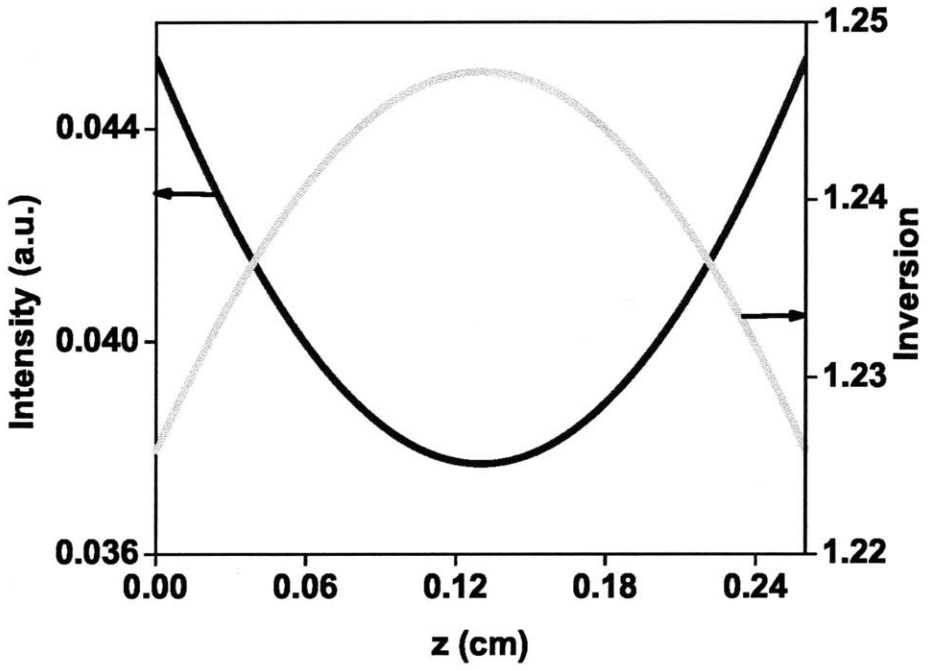

Figure A-5: Steady state intensity (blue line) and inversion (green line) in the cavity without SHB and without modulation for DC pumping p=1.1 after 1785 roundtrips.

coincide with the pulse maximum. The front of the pulse extracts gain so it is more amplified than the back of the pulse experiencing the reduced gain, due to the long gain recovery time compared to the pulse duration. As a result, the group velocity of the pulse is increased.

Second the laser dynamics under current modulation is studied. Figure A-7 shows the intensity of the output pulses from the QCL at the right end of the laser cavity, (i.e. the laser output is monitored as a function of time) for different DC pumping levels and constant modulation amplitude (m=5). As expected, isolated pulses with a steady state pulse shape are formed by the strong gain modulation in the short gain section. For increased DC-pumping levels of the long gain section, the pulse energy or average output power is increasing. The pulse duration depends on the pumping level. This can be understood by the fact that the long section acts as an amplifier with a recovery time on the order of the cavity roundtrip time. Although the gain is slow, with a recovery time equal the cavity

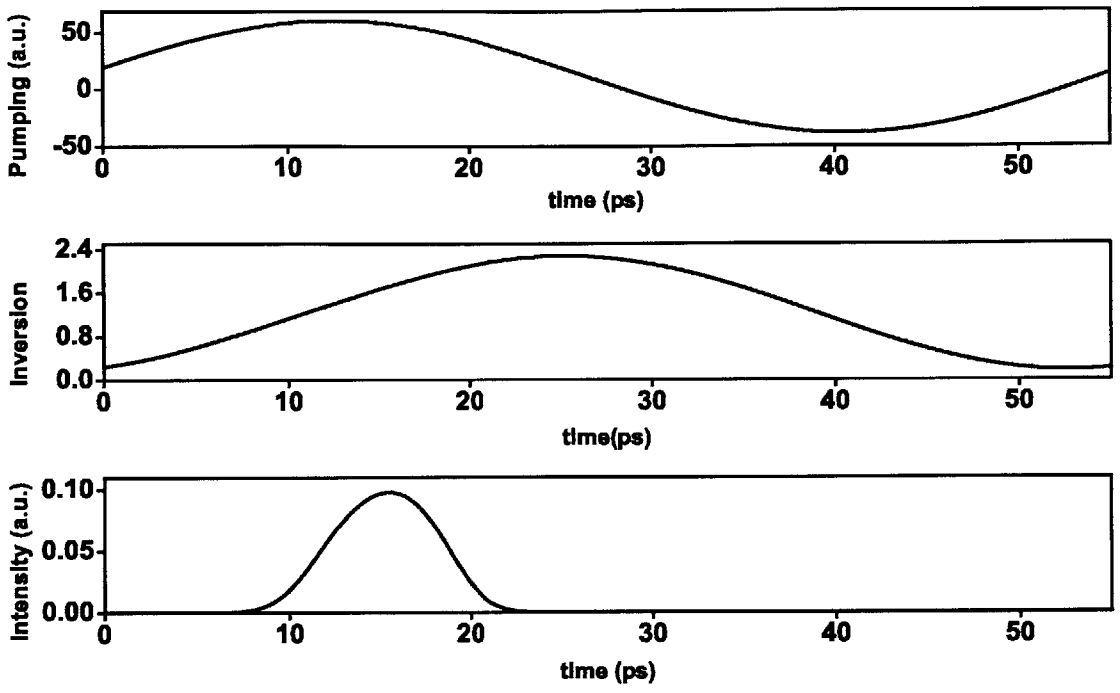

Figure A-6: Pumping, inversion and intensity for a point inside the modulation section for p=1.1 and m=5 without SHB.

roundtrip time, it leads to substantial reshaping of the pulse towards longer pulses, i.e. suppression of multimode operation. When the DC pumping level is close to threshold (p=1.1) the pulse is weak and therefore only weakly saturates the amplifier leading to minimum pulse lengthening during propagation through the long section. The long section mostly helps to compensate for the waveguide and facet losses. With increasing DC pumping (p=1.45 and p=1.61), the pulse energy and with it the gain saturation and pulse lengthening increases, explaining the increase in pulse duration with increased pumping.

For the purpose of comparison with later simulation and experimental results, Figure A-8 shows the normalized spectral intensities and Figure A-9 shows the computed Interferometric Autocorrelation (IAC) traces for the three cases in Figure A-8.a-c. When DC pumping is close to threshold many modes are lasing and locked (Figure A-7.a) and as a result the pulses are fairly short, as we can see in Figure A-7.a. As DC pumping increases we can

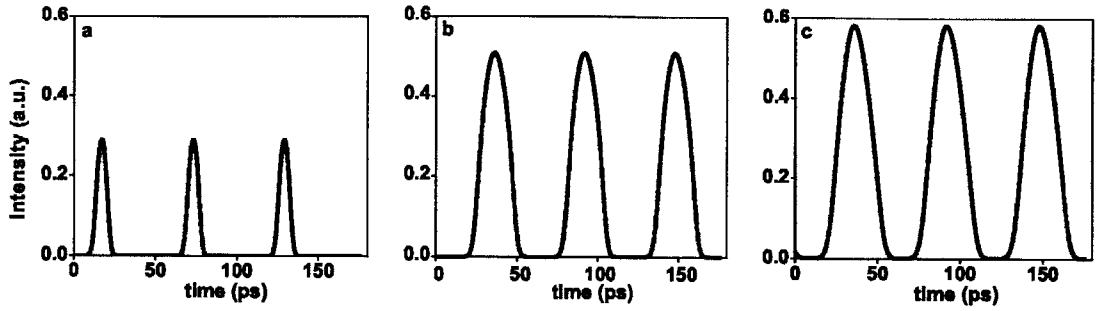

Figure A-7: Intensity profile of output pulse train for modulation with AC-amplitude m=5 for different DC pumping levels without SHB. a) p=1.1 b) p=1.45, and c) p=1.61

see in Figure A-8 that the pulses become longer in time and from the spectra we observe that fewer modes are lasing due to the intensity smoothing effect of a saturating and fast recovering gain in the long section. For low DC pumping level the ratio of peak to background is 8:1 (Figure A-9.a), which verifies that the pulses are isolated. IAC traces for higher DC pumping levels start to overlap. For the case without SHB, the IAC traces and in fact the computed electric fields do not show any chirp i.e. nontrivial phase over the pulse.

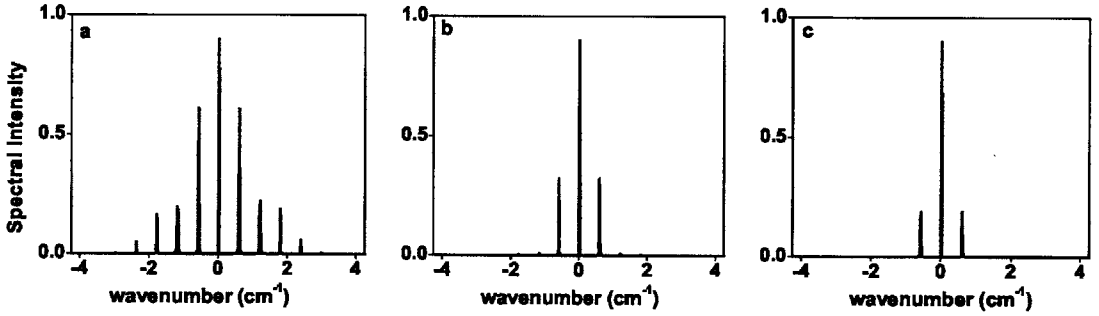

Figure A-8: Spectral intensities for modulation with AC-amplitude m=5 for different DC pumping levels without SHB a) p=1.1 b) p=1.45, and c) p=1.61

As we will see later, these do not fully account for what is found experimentally and inclusion of SHB is necessary to explain the observations.

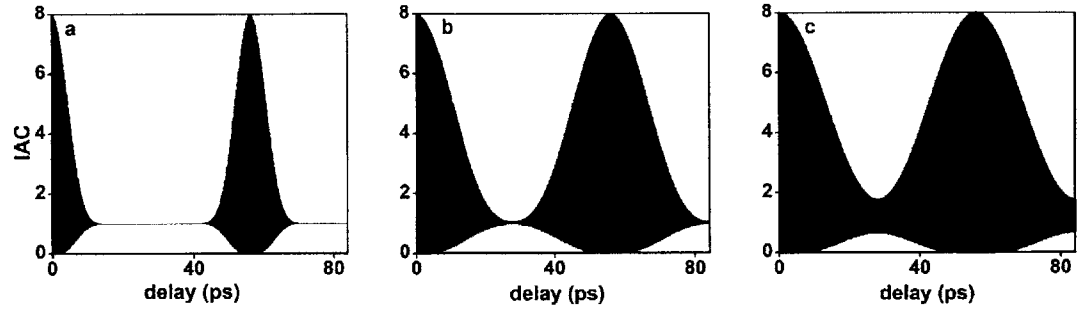

Figure A-9: Interferometric autocorrelation traces (IACs) for modulation with AC amplitude m=5 for different DC pumping levels without SHB a) p=1.1 b) p=1.45, and c) p=1.61

A.8 Experimental Observations

The experiments are described in detail in [69]. The experimental results show the same general trend of pulse lengthening with increased DC pumping, however there is a major difference. The pulses in the simulations are in general longer in time than the pulses observed experimentally. For the case of a DC pumping parameter p=1.1, the pulse in Figure A-7.a is close to a Gaussian with a 7 psec FWHM duration. The measured interferometric autocorrelations for different pumping levels are shown in Figure A-10, and in particular for p=1.1 in Figure A-10.a, assuming a Gaussian pulse shape, a FWHM pulse duration of 3 psec is extracted. The experimentally observed spectra are also much more broadband compared to the theoretical ones from the simulation. This indicates that SHB is important and must be incorporated in the model.

A.9 QCL Dynamics with Spatial Hole Burning

To include SHB in the model we use Eq. A.16-A.19 in the simulations. The total inversion now consists of the average inversion Δ_0 and the inversion grating. The interference of the two counter-propagating waves produces a standing wave pattern in the optical intensity, which in turn varies spatially the saturation of the laser medium. Due to the spatial gain grating more modes start lasing, however as we will show below this grating does not become

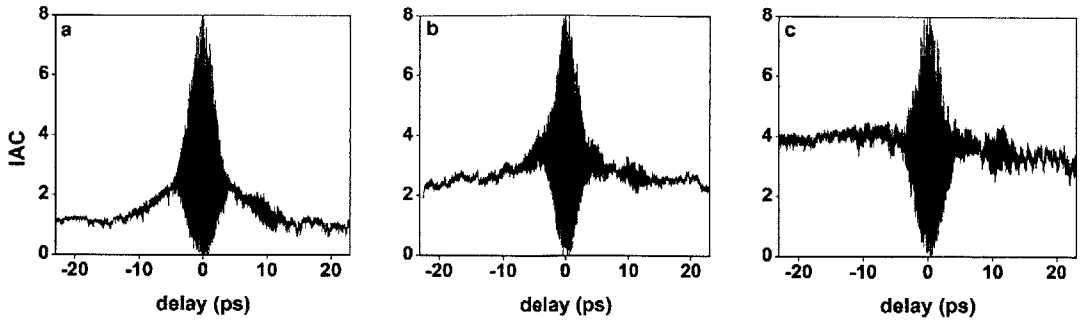

Figure A-10: Measured interferometric autocorrelation traces (IACs) for modulation with AC amplitude m=5 (35 dBm applied RF-power) for different DC pumping levels. a) p=1.1 (340 mA) b) p=1.45 (450 mA), and c) p=1.61 (500 mA). [69]

stationary. The wave, as it propagates, is reflected from the nonstationary grating at some positions (SHB interferes with mode locking) and this leads to differential and time varying phase shifts between the modes. Thus, in the presence of SHB the modes acquire nonlinear phase shifts and with it also the pulse. Like in the case without SHB, the DC pumping level should be close to threshold so that the pulses do not lengthen too much.

To obtain insight into the non-stationary gain grating, the continuous wave solution of the model is determined in the absence of a current modulation. In Figure A-11 we show the inversion along the cavity for DC pumping 1.1 times above threshold at three different times about 5000 roundtrips apart. As the number of roundtrips increases, the average inversion and the inversion grating continue to evolve and never reach a steady state. The inversion profile and inversion grating show a degree of randomness. If there would be a steady state, one would expect that due to the large losses per roundtrip the system would certainly come into steady state within at least a hundred roundtrips. This is not the case.

If we increase the DC pumping to 2 times above threshold, the degree of randomness in the grating is further increased due to the increase in the number of modes that are lasing, see Figure A-12.

In the following, we show the intensity and the inversion profiles in the cavity when the modulation is switched on, for various time instants and different DC pumping levels. In

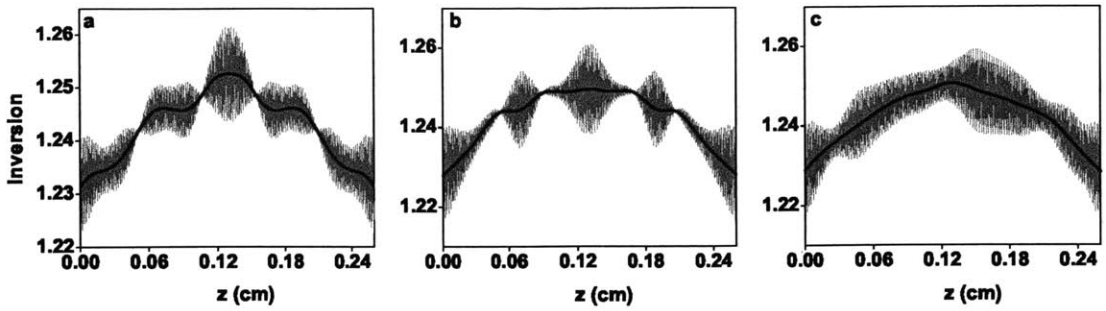

Figure A-11: Average inversion Δ_0 (blue line) and total inversion along the cavity length including the inversion grating (red line) for DC pumping p=1.1 and no modulation after a) 5357 roundtrips, b) 10714 roundtrips c) 17857 roundtrips.

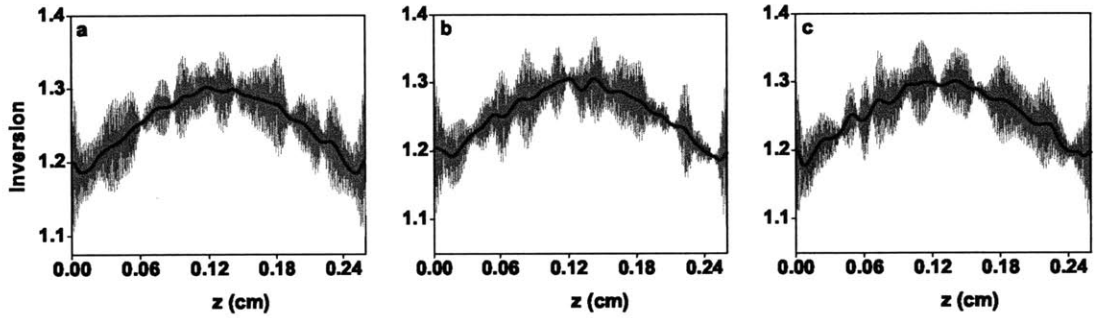

Figure A-12: Average inversion Δ_0 (blue line) and total inversion along the cavity length including the inversion grating (red line) for DC pumping p=2 and no modulation after a) 5357 roundtrips, b) 10714 roundtrips c) 17857 roundtrips.

Figure A-13 the DC pumping is 1.1 times above threshold. When the pulse is reflected from one of the facets, Figure A-13.a and c, a grating is formed due to the presence of forward and backward waves. Since there are isolated pulses produced, there is no grating when the pulse is propagating in the middle of the cavity, Figure A-13.b. However, there is still some gain grating left over at the left end of the waveguide, where the pulse was reflected last and consequently the grating has not yet decayed completely.

If we increase the DC pumping to 2 times above threshold (Figure A-14) there are no longer isolated pulses per roundtrip. The pulse has broken up into multiple beats of the lasing modes, due to the large and too fast recovering gain in the long waveguide section and a gain grating is observable over the full length of the laser cavity.

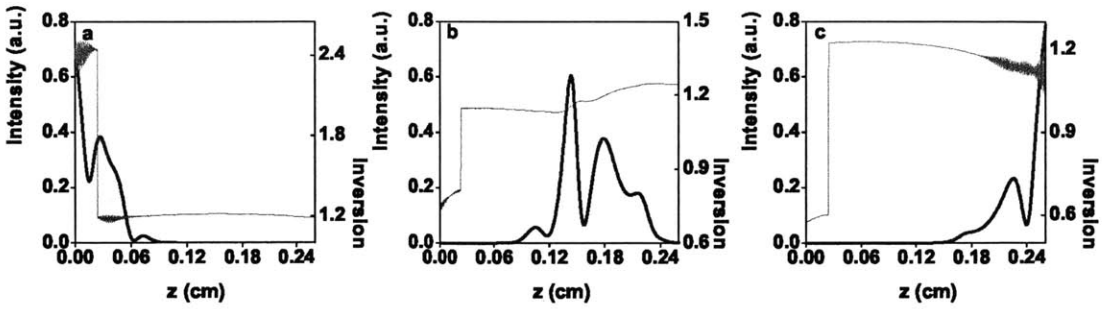

Figure A-13: Intensity profile (blue line) and total inversion (red line) along the cavity for DC pumping p=1.1 and AC amplitude m=5 a) when the pulse is reflected off the left facet and propagates to the right b) when the pulse is in the middle of the cavity and propagates to the right c) when the pulse is reflected off the right facet and propagates to the left.

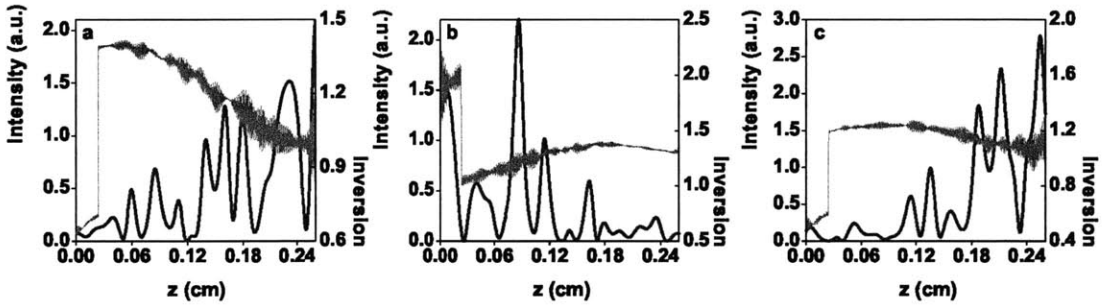

Figure A-14: Intensity profile (blue line) and total inversion (red line) along the cavity for DC pumping p=2 and AC amplitude m=5 a) when the pulse is reflected off the left facet and propagates to the right b) when the pulse is in the middle of the cavity and propagates to the right c) when the pulse is reflected off the right facet and propagates to the left.

Note, in both Figure A-13 and A-14 there is a discontinuity in the inversion at the boundary between the short modulated section and the long, continuously pumped section.

Similar to Figures A-7 up to A-9 we simulate the laser dynamics under current modulation in the presence of SHB. The simulation results shown in the following are snapshots of the laser dynamics after simulating 10,750 roundtrips (0.6 μs). Figure A-15 shows the normalized time averaged spectral intensities that are generated by Fourier-Transformation of a 29 roundtrip long time series, and Figure A-16 shows the intensity of the output pulses at the end of the QCL cavity for different DC pumping levels and constant modulation amplitude (m=5) for a duration of about three cavity roundtrips. As explained above, the generated

pulse trains and spectra do not reach a true steady state, but rather remain dynamic on the few percent level. If we compare the spectral intensities in Figure A-15 with the ones in Figure A-8, where no SHB is included, we see that many more modes are lasing in the presence of SHB in agreement with the experiment. For DC pumping close to threshold (p=1.1) the phases between the modes are locked to the values favoring the formation of an isolated pulse and the main peak of the pulse becomes as short as 2 psec (Figure A-16.a). With increasing DC pumping level, more modes start lasing (Figure A-16.b, c), since the magnitude of the inversion grating becomes stronger. At the same time, the intensity profile of the pulses becomes more structured (Figure A-16.b, c). The reason for the structure is the decorrelation of the phases between the modes due to SHB. Also the speed of the gain modulation, which stays fixed, is no longer capable to lock all modes of the increasingly broadband spectrum. Furthermore, with increased DC-pumping, passive gain modulation in the amplifier section, due to gain saturation by the pulse and partial gain recovery, becomes stronger and again the peak of the pulse experiences less gain than the wings, destabilizing short pulse generation.

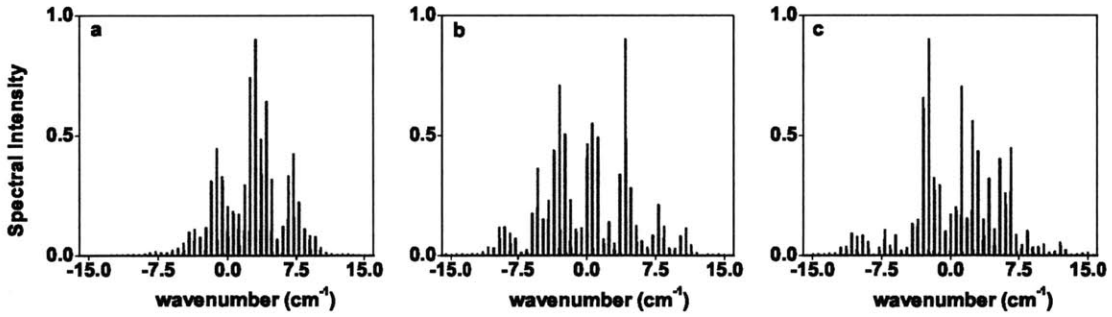

Figure A-15: Spectral intensities for modulation with AC amplitude m=5 for different DC pumping levels including SHB a) p=1.1 b) p=1.45, and c) p=1.61

The computed IAC traces for the three cases in Figure A-16 are shown in Figure A-17 and reflect the structure that is observed in the intensity profiles. As DC pumping increases, we observe in the IAC traces more and more substructure. The simulation traces back this sub-structure to the nonlinear phase introduced by SHB.

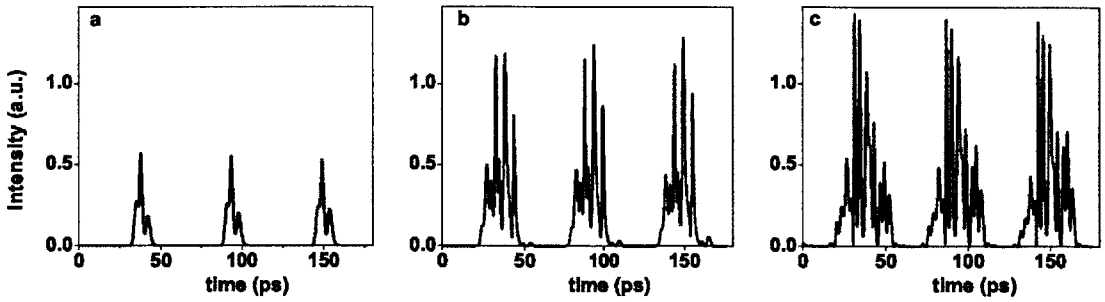

Figure A-16: Intensity profile of output pulse train for modulation with AC amplitude m=5 for different DC pumping levels including SHB a) p=1.1 b) p=1.45, and c) p=1.61

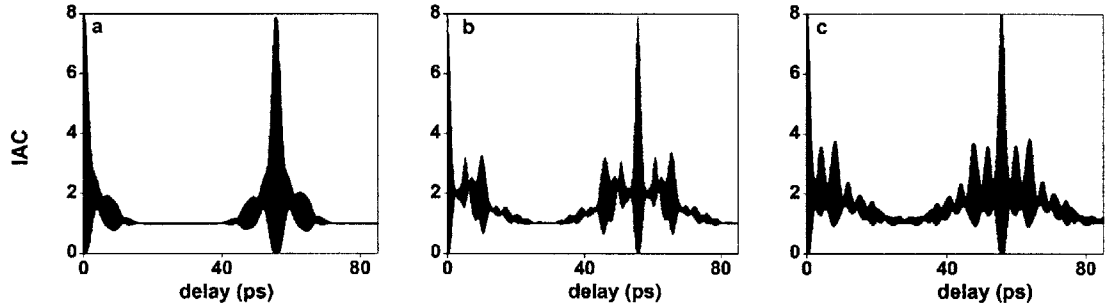

Figure A-17: Interferometric autocorrelation traces (IACs) for modulation with AC amplitude m=5 for different DC pumping levels including SHB. a) p=1.1 b) p=1.45, and c) p=1.61

The grating decay time T_g is always smaller than the upper state lifetime T_1, see Eq. A.19. When the effects of carrier diffusion are negligible, i.e. T_g becomes close to T_1, the strength of SHB increases (the amplitude of the inversion grating relaxes slower) and the side lobes in the IAC become more pronounced. In Figure A-18.a we see the effect on the side lobes when T_g increases from 5 psec (used so far) to 10 psec. The same behavior also occurs when T_1 decreases. As explained before, decrease in T_1 results in increase of the effect of SHB and subsequent deterioration of the pulse quality as it is shown in Figure A-18.b.

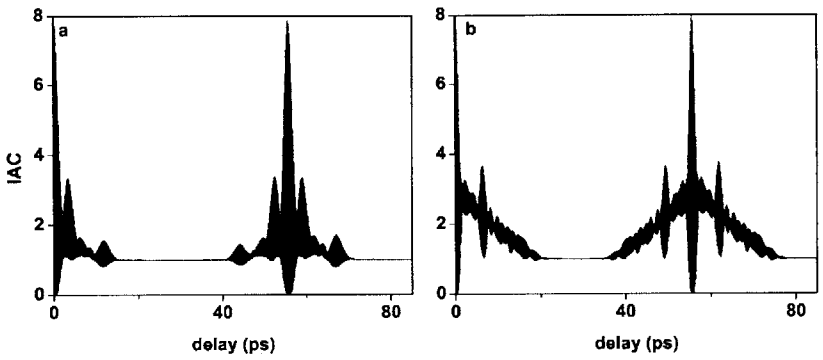

Figure A-18: Interferometric autocorrelation traces (IACs) for modulation with AC amplitude m=5, and DC pumping level p=1.1 a) for $T_1 = 50$ psec and $T_g = 10$ psec b) for $T_1 = 5$ psec and $T_g = 2.5$ psec. Comparing the two figures with Figure A-17.a we see that the structure is more pronounced in these figures due to the stronger SHB.

Appendix B

Derivation of Equation 3.10

In this appendix we derive in detail Eq. 3.10 following the slowly varying envelope approximation in the harmonic field. We can represent the harmonic field and the nonlinear polarization as a sum of their various frequency components [26]

$$E_h(r,z,t) = \sum_q E_{hq}(r,z,t) \tag{B.1}$$

and

$$P^{NL}(r,z,t) = \sum_q P_q^{NL}(r,z,t) \tag{B.2}$$

where q is the order of each harmonic. Each frequency component is presented as:

$$E_{hq}(r,z,t) = E_q(r,z,t)e^{ik_q z} \tag{B.3}$$

and

$$P_q^{NL}(r,z,t) = p_q^{NL}(r,t)e^{iqk_1 z} \tag{B.4}$$

where $E_q(r,z,t)$ and $p_q^{NL}(r,t)$ are the envelopes of the harmonic field and the nonlinear polarization respectively. By substituting them in Eq. 3.4 we obtain

$$\frac{\partial E_{hq}}{\partial z} = \frac{\partial E_q}{\partial z}e^{ik_q z} + ik_q E_q e^{ik_q z} \tag{B.5}$$

$$\frac{\partial^2 E_{hq}}{\partial z^2} = \frac{\partial^2 E_q}{\partial z^2} e^{ik_q z} + 2ik_q \frac{\partial E_q}{\partial z} e^{ik_q z} - k_q^2 E_q e^{ik_q z} \tag{B.6}$$

In the paraxial approximation, we neglect the second derivative of the envelope compared to the wave number of the field. Using in addition the Fourier transforms of the harmonic field and the nonlinear polarization in Eq. 3.7 we get

$$\left(\nabla_\perp^2 \tilde{E}_q(r,z,\omega_q) + 2ik_q \frac{\partial \tilde{E}_q(r,z,\omega_q)}{\partial z} - k_q^2 \tilde{E}_q(r,z,\omega_q) + \frac{n^2}{c^2}(q\omega)^2 \tilde{E}_q(r,z,\omega_q) \right) e^{ik_q z}$$
$$= -\frac{(q\omega)^2}{\epsilon_0 c^2} \tilde{p}_q^{NL}(r,\omega_q) e^{iqk_1 z} \tag{B.7}$$

The refractive index is $n = n_{real} + in_{imag}$ ($n_{real} \gg n_{imag}$ and that $n_{real} \approx 1$) and since $k_q = \omega_q n_{real}/c$ the left hand side of the previous equation becomes

$$\left(\nabla_\perp^2 \tilde{E}_q(r,z,\omega_q) + 2i\frac{\omega_q}{c} \frac{\partial \tilde{E}_q(r,z,\omega_q)}{\partial z} + 2in_{imag} \frac{\omega_q^2}{c^2} \tilde{E}_q(r,z,\omega_q) \right) e^{ik_q z} \tag{B.8}$$

The absorption coefficient at frequency ω_q is $\kappa = \omega_q n_{imag}/c$, which is equal to $\rho\sigma(\omega)/2$ where ρ is the density of atoms and σ is the absorption cross section. Thus

$$\nabla_\perp^2 \tilde{E}_q(r,z,\omega_q) e^{ik_q z} + 2i\frac{\omega_q}{c} \left(\frac{\partial \tilde{E}_q(r,z,\omega_q)}{\partial z} + \frac{\rho\sigma(\omega_q)}{2} \tilde{E}_q(r,z,\omega_q) \right) e^{ik_q z} = -\frac{\omega_q^2}{\epsilon_0 c^2} \tilde{p}_q^{NL}(r,\omega_q) e^{iqk_1 z}$$

$$\Rightarrow \left(\frac{c}{2i\omega_q} \nabla_\perp^2 \tilde{E}_q(r,z,\omega_q) + \frac{\partial \tilde{E}_q(r,z,\omega_q)}{\partial z} + \frac{\rho\sigma(\omega_q)}{2} \tilde{E}_q(r,z,\omega_q) \right) e^{ik_q z} = \frac{1}{2\epsilon_0 c} i\omega_q \tilde{p}_q^{NL}(r,\omega_q) e^{iqk_1 z} \tag{B.9}$$

The nonlinear polarization is equal to $\tilde{p}_q^{NL}(r,\omega_q) = \rho \tilde{d}_q(r,\omega_q)$ with $\tilde{v}_q(r,\omega_q) = -i\omega_q \tilde{d}_q(r,\omega_q)$ we get Eq. 3.10

Appendix C

Derivation of Energy of a Single Harmonic

In this Appendix we will show that the energy in a single harmonic is given by

$$\int_{2m\omega_0}^{2(m+1)\omega_0} d\omega |\tilde{E}_h(\omega)|^2 = \frac{1}{2\pi}\left|1+\beta e^{i\pi\left(1-\frac{\Omega}{\omega_0}\right)}\right|\left(\frac{4\pi\alpha}{\Omega\sigma(\omega)}\right)^2\left|\int_0^{\frac{\pi}{\omega_0}}\ddot{\xi}(t)e^{-i\Omega t}dt\right|^2 2\omega_0\frac{1-(\beta^4)^{N-1}}{1-\beta^4} \tag{C.1}$$

From Eq. 5.8 the Fourier transform of the harmonic field is

$$\tilde{E}_h(\omega) = -\frac{4\pi\alpha}{\sqrt{2\pi}i\omega\sigma(\omega)}\int_0^{\frac{2\pi}{\omega_0}}\ddot{\xi}(t)e^{i\omega t}dt \tag{C.2}$$

assuming perfect phase matching over the whole spectrum and absorption limited conditions. As said before, the Fourier transform is carried out by using the periodicity of driver pulse and trajectories in each half-cycle.

We show that

$$\int_0^{\frac{2\pi}{\omega_0}(N-1)}\ddot{\xi}(t)e^{-i\omega t dt} = \int_0^{\frac{2\pi}{\omega_0}(N-1)}\ddot{\xi}(t)e^{-i\omega t}dt\sum_{n=0}^{N-2}\beta^{2n}e^{-i\omega n\frac{2\pi}{\omega_0}} \tag{C.3}$$

If we split the integral in a sum of integrals over each period Eq. C.3 becomes

$$\int_0^{\frac{2\pi}{\omega_0}(N-1)} e^{-\lambda t}\ddot{\xi}_0(t)e^{-i\omega t}dt = \sum_{n=0}^{N-2}\int_{\frac{2\pi n}{\omega_0}}^{\frac{2\pi(n+1)}{\omega_0}} \ddot{\xi}(t)e^{-i\omega t}dt \tag{C.4}$$

Each term in Eq. C.4 can be written as

$$\int_{\frac{2\pi n}{\omega_0}}^{\frac{2\pi(n+1)}{\omega_0}} \ddot{\xi}(t)e^{-i\omega t}dt = \int_0^{\frac{2\pi}{\omega_0}} \ddot{\xi}(t+n\frac{2\pi}{\omega_0})e^{-i\omega t}e^{-i\omega n\frac{2\pi}{\omega_0}}d\left(t+n\frac{2\pi}{\omega_0}\right) \tag{C.5}$$

and since $\ddot{\xi}(t+n\frac{2\pi}{\omega_0}) = \beta^{2n}\ddot{\xi}(t)$ Eq. C.5 becomes

$$\int_{\frac{2\pi n}{\omega_0}}^{\frac{2\pi(n+1)}{\omega_0}} \ddot{\xi}(t)e^{-i\omega t}dt = \int_0^{\frac{2\pi}{\omega_0}} \beta^{2n}\ddot{\xi}(t)e^{-i\omega t}e^{-i\omega n\frac{2\pi}{\omega_0}}dt \tag{C.6}$$

Thus

$$\int_0^{\frac{2\pi(N-1)}{\omega_0}} \ddot{\xi}(t)e^{-i\omega t}dt = \int_0^{\frac{2\pi}{\omega_0}} \ddot{\xi}(t)e^{-i\omega t}dt\sum_{n=0}^{N-2}\beta^{2n}e^{-i\omega n\frac{2\pi}{\omega_0}} \tag{C.7}$$

The energy in a single harmonic is given from the integral of the square modulus of the harmonic field over a frequency range associated with one (odd) harmonic is

$$\begin{aligned}\int_{2m\omega_0}^{2(m+1)\omega_0} d\omega|\tilde{E}_h(\omega)|^2 &= \frac{1}{2\pi}\left(\frac{4\pi\alpha}{\Omega\sigma(\omega)}\right)^2 \int_{2m\omega_0}^{2(m+1)\omega_0} d\omega \left|\int_0^{\frac{2\pi}{\omega_0}} \ddot{\xi}(t)e^{-i\omega t}dt\right|^2 \left|\sum_{n=0}^{N-2}\beta^{2n}e^{-i\omega n\frac{2\pi}{\omega_0}}\right| \\ &= \frac{1}{2\pi}\left(\frac{4\pi\alpha}{\Omega\sigma(\omega)}\right)^2 \left|\int_0^{\frac{2\pi}{\omega_0}} \ddot{\xi}(t)e^{-i\Omega t}dt\right|^2 \int_{2m\omega_0}^{2(m+1)\omega_0} d\omega \left|\sum_{n=0}^{N-2}\beta^{2n}e^{-i\omega n\frac{2\pi}{\omega_0}}\right|^2 \\ &= \frac{1}{2\pi}\left(\frac{4\pi\alpha}{\Omega\sigma(\omega)}\right)^2 \left|\int_0^{\frac{2\pi}{\omega_0}} \ddot{\xi}(t)e^{-i\Omega t}dt\right|^2 \int_{2m\omega_0}^{2(m+1)\omega_0} d\omega \sum_{k,n=0}^{N-2}\beta^{2(n+k)}e^{-i\omega(n-k)\frac{2\pi}{\omega_0}}\end{aligned} \tag{C.8}$$

The integral over $d\omega$ is non zero only for $n = k$, so we get

$$\int_{2m\omega_0}^{2(m+1)\omega_0} d\omega \sum_{n=0}^{N-2}\beta^{4n} = 2\omega_0\frac{1-\beta^{4(N-1)}}{1-\beta^4} \tag{C.9}$$

Thus, we infer that the energy in a single odd harmonic Ω is

$$\int_{2m\omega_0}^{2(m+1)\omega_0} d\omega|\tilde{E}_h(\omega)|^2 = \frac{1}{2\pi}\left(\frac{4\pi\alpha}{\Omega\sigma(\omega)}\right)^2 \left|\int_0^{\frac{2\pi}{\omega_0}} \ddot{\xi}(t)e^{-i\Omega t}dt\right|^2 2\omega_0\frac{1-\beta^{4(N-1)}}{1-\beta^4} \tag{C.10}$$

In the high harmonic generation process the recombination events happen each half-cycle, and thus

$$\int_0^{\frac{2\pi}{\omega_0}} \ddot{\xi}(t)e^{-i\Omega t}dt = \left(1+\beta e^{i\pi\left(1-\frac{\Omega}{\omega_0}\right)}\right)\int_0^{\frac{\pi}{\omega_0}} \ddot{\xi}(t)e^{-i\Omega t}dt \tag{C.11}$$

where we used

$$\ddot{\xi}(t+\frac{\pi}{\omega_0}) = -\beta\ddot{\xi}(t) = \beta e^{i\pi}\ddot{\xi}(t) \tag{C.12}$$

Thus the energy in a single harmonic is given from

$$\int_{2m\omega_0}^{2(m+1)\omega_0} d\omega |\tilde{E}_h(\omega)|^2 = \frac{1}{2\pi} \left| 1 + \beta e^{i\pi\left(1-\frac{\Omega}{\omega_0}\right)} \right| \left(\frac{4\pi\alpha}{\Omega\sigma(\omega)} \right)^2 \left| \int_0^{\frac{\pi}{\omega_0}} \ddot{\xi}(t) e^{-i\Omega t} dt \right|^2 2\omega_0 \frac{1-(\beta^4)^{N-1}}{1-\beta^4} \tag{C.13}$$

Appendix D

Numerical model in 3-dimensions

In this Appendix we will describe the numerical model for the simulation of the wave equation in 3 dimensions in cylindrical coordinates, assuming that the driving field propagates in free space

$$\nabla^2 E(r_T, z, t) - \frac{n^2}{c^2}\frac{\partial^2}{\partial t^2} E(r_T, z, t) = 0 \tag{D.1}$$

Eq. D.2 can be rewritten as

$$\nabla^2 E(r_T, z, t) + \frac{\partial^2}{\partial z^2} E(r_T, z, t) - \frac{n^2}{c^2}\frac{\partial^2}{\partial t^2} E(r_T, z, t) = 0 \tag{D.2}$$

We introduce the slowly varying envelope function $E(r_T, z, t) = \tilde{E}(r_T, z, t)e^{i(kz-\omega t)}$ and we apply the slowly varying envelope approximation

$$\frac{\partial}{\partial z} E(r_T, z, t) = \frac{\partial}{\partial z}\tilde{E}(r_T, z, t)e^{i(kz-\omega t)} + ik\tilde{E}(r_T, z, t)e^{i(kz-\omega t)} \tag{D.3}$$

$$\frac{\partial^2}{\partial z^2} E(r_T, z, t) = \frac{\partial^2}{\partial z^2}\tilde{E}(r_T, z, t)e^{i(kz-\omega t)} + 2ik\frac{\partial}{\partial z}\tilde{E}(r_T, z, t)e^{i(kz-\omega t)} - k^2\tilde{E}(r_T, z, t)e^{i(kz-\omega t)} \tag{D.4}$$

$$\frac{\partial}{\partial t} E(r_T, z, t) = \frac{\partial}{\partial t}\tilde{E}(r_T, z, t)e^{i(kz-\omega t)} - i\omega\tilde{E}(r_T, z, t)e^{i(kz-\omega t)} \tag{D.5}$$

$$\frac{\partial^2}{\partial t^2}E(r_T,z,t) = \frac{\partial^2}{\partial t^2}\tilde{E}(r_T,z,t)e^{i(kz-\omega t)} - 2i\omega\frac{\partial}{\partial t}\tilde{E}(r_T,z,t)e^{i(kz-\omega t)} - \omega^2\tilde{E}(r_T,z,t)e^{i(kz-\omega t)} \tag{D.6}$$

We consider that the envelope $\tilde{E}(r_T,z,t)$ varies slowly on the scale of an optical wavelength or an optical period, i.e. $\frac{\partial^2}{\partial z^2} \ll k\frac{\partial}{\partial z}$ and $\frac{\partial^2}{\partial t^2} \ll \omega\frac{\partial}{\partial t}$

This results in

$$\nabla^2\tilde{E}(r_T,z,t) + 2ik\frac{\partial}{\partial z}\tilde{E}(r_T,z,t) - k^2\tilde{E}(r_T,z,t) + 2i\omega\frac{n^2}{c^2}\frac{\partial\tilde{E}(r_T,z,t)}{\partial t} + \omega^2\frac{n^2}{c^2}\tilde{E}(r_T,z,t) \tag{D.7}$$

After substituing $k = n\omega/c$ in Eq. D.7 we get

$$\nabla^2\tilde{E}(r_T,z,t) + 2ik\left(\frac{\partial}{\partial z} + \frac{n}{c}\frac{\partial}{\partial t}\right)tildeE(r_T,z,t) \tag{D.8}$$

We introduce the retarded time frame

$$t' = t - \frac{nz}{c} \tag{D.9}$$

$$z' = z \tag{D.10}$$

and Eq.D.8 can be written as

$$\nabla^2 E(r_T,z,t') = 2ik\frac{\partial}{\partial z}E(r_T,z,t') = 0 \tag{D.11}$$

where we dropped the tilde on the pulse envelope. Eq. D.11 is the one we use to simulate the propagation of the driving field in free space.

Assuming cylindrical symmetry ($\partial/\partial\phi = 0$) Eq. D.11 can be written as

$$\frac{\partial^2}{\partial r^2}E(r_T,z,t') + \frac{1}{r}\frac{\partial}{\partial r}E(r_T,z,t') + 2ik\frac{\partial}{\partial z}E(r_T,z,t') = 0 \tag{D.12}$$

The solution of Eq.D.12 at each point in z is

$$E(z+dz) = E(z)exp\left(\frac{i}{2k}\nabla_T^2 dz\right) \tag{D.13}$$

where

$$\nabla_T^2 = \frac{\partial^2}{\partial r^2} + \frac{1}{r}\frac{\partial}{\partial r} \tag{D.14}$$

For $r = 0$, $\frac{\partial E}{\partial r} = 0$ so that the electric field has physical meaning. The term $\frac{1}{e}\frac{\partial E}{\partial r}$ needs special treatment. Taking the Taylor series expansion of the electric field at r=0

$$E(r) = E(0) + r\left.\frac{\partial E}{\partial r}\right|_{r=0} + \frac{r^2}{2}\left.\frac{\partial^2 E}{\partial r^2}\right|_{r=0} = E(0) + \frac{r^2}{2}\left.\frac{\partial^2 E}{\partial r^2}\right|_{r=0} \tag{D.15}$$

Taking the fist derivative on both sides of Eq. D.15 we have

$$\left.\frac{\partial E}{\partial r}\right|_{r=0} = r\left.\frac{\partial^2 E}{\partial r^2}\right|_{r=0} \Rightarrow \frac{1}{r}\left.\frac{\partial E}{\partial r}\right|_{r=0} = \left.\frac{\partial^2 E}{\partial r^2}\right|_{r=0} \tag{D.16}$$

At the end boundary in r we set the electric field equal to 0.

We use the finite difference method to model Eq. D.14. Using the method of undetermined coefficients (centered scheme) we will find the weights δ_j^m that approximate the derivatives

$$\left.\frac{d^m E}{dr^m}\right|_{r=r_i} \approx \sum_{j=l}^{r} \delta_j^m E_j \tag{D.17}$$

Our interpolating polynomial will be of 6th order. For whatever m (in our case $m = 1$ and $m = 2$), $l = i - 3$, $r = i + 3$ (centered scheme) and uniform spacing Δr we have:

$$\left.\frac{d^m E}{dr^m}\right|_{r=r_i} \approx \sum_{j=i-3}^{i+3} \delta_j^m E_j$$

$$= \delta_{i-3}^m E_{i-3} + \delta_{i-2}^m E_{i-2} + \delta_{i-1}^m E_{i-1} + \delta_i^m E_i + \delta_{i+1}^m E_{i+1} + \delta_{i+2}^m E_{i+2} + \delta_{i+3}^m E_{i+3}$$

$$= \delta_{i-3}^m \left(E_0 - 3\Delta r E_0' + \frac{(3\Delta r)^2}{2} E_0'' - \frac{(3\Delta r)^3}{6} E_0^{(3)} + \frac{(3\Delta r)^4}{24} E_0^{(4)} - \frac{(3\Delta r)^5}{120} E_0^{(5)} + \frac{(3\Delta r)^6}{720} E_0^{(6)} \right)$$

$$+ \delta_{i-2}^m \left(E_0 - 2\Delta r E_0' + \frac{(2\Delta r)^2}{2} E_0'' - \frac{(2\Delta r)^3}{6} E_0^{(3)} + \frac{(2\Delta r)^4}{24} E_0^{(4)} - \frac{(2\Delta r)^5}{120} E_0^{(5)} + \frac{(2\Delta r)^6}{720} E_0^{(6)} \right)$$

$$+ \delta_{i-1}^m \left(E_0 - \Delta r E_0' + \frac{(\Delta r)^2}{2} E_0'' - \frac{(\Delta r)^3}{6} E_0^{(3)} + \frac{(\Delta r)^4}{24} E_0^{(4)} - \frac{(\Delta r)^5}{120} E_0^{(5)} + \frac{(\Delta r)^6}{720} E_0^{(6)} \right)$$

$$+ \delta_i^m E_0$$

$$+ \delta_{i+1}^m \left(E_0 + \Delta r E_0' + \frac{(\Delta r)^2}{2} E_0'' + \frac{(\Delta r)^3}{6} E_0^{(3)} + \frac{(\Delta r)^4}{24} E_0^{(4)} + \frac{(\Delta r)^5}{120} E_0^{(5)} + \frac{(\Delta r)^6}{720} E_0^{(6)} \right)$$

$$+ \delta_{i+2}^m \left(E_0 + 2\Delta r E_0' + \frac{(2\Delta r)^2}{2} E_0'' + \frac{(2\Delta r)^3}{6} E_0^{(3)} + \frac{(2\Delta r)^4}{24} E_0^{(4)} + \frac{(2\Delta r)^5}{120} E_0^{(5)} + \frac{(2\Delta r)^6}{720} E_0^{(6)} \right)$$

$$+ \delta_{i+3}^m \left(E_0 + 3\Delta r E_0' + \frac{(3\Delta r)^2}{2} E_0'' + \frac{(3\Delta r)^3}{6} E_0^{(3)} + \frac{(3\Delta r)^4}{24} E_0^{(4)} + \frac{(3\Delta r)^5}{120} E_0^{(5)} + \frac{(3\Delta r)^6}{720} E_0^{(6)} \right) \tag{D.18}$$

Thus the derivatives are approximated by

$$\frac{1}{r} \left.\frac{\partial E}{\partial r}\right|_{r=r_i} = \frac{1}{(i-1)\Delta r} \frac{-\frac{1}{60} E_{i-3} + \frac{3}{20} E_{i-2} - \frac{3}{4} E_{i-1} + \frac{3}{4} E_{i+1} - \frac{3}{20} E_{i+2} + \frac{1}{60} E_{i+3}}{\Delta r} \tag{D.19}$$

$$\left.\frac{\partial^2 E}{\partial r^2}\right|_{r=r_i} = \frac{\frac{1}{90} E_{i-3} - \frac{3}{20} E_{i-2} + \frac{3}{2} E_{i-1} - \frac{49}{18} E_i + \frac{3}{2} E_{i+1} - \frac{3}{20} E_{i+2} + \frac{1}{90} E_{i+3}}{\Delta r^2} \tag{D.20}$$

Bibliography

[1] Lawrence Berkeley National Laboratory webpage, http://www.lbl.gov/MicroWorlds/ALSTool/EMSpec/EMSpec2.html

[2] K. C. Kulander, K. J. Schafer and J. L. Krause, *Super-Intense Laser-Atom Physics NATO ASI Series B*, 316, p. 95 (1993)

[3] P. B. Corkum, Plasma perspective on strong field multiphoton ionization, *Physical Review Letters*, 71 (13), pp. 1994-1997 (1993)

[4] H. Kapteyn, O. Cohen, I. Christov, M. Murnane, Harnessing Attosecond Science in the Quest for Coherent X-rays, *Science*, 317 (5839), pp. 775-778 (2007)

[5] Y. H. Wang, D. Hsieh, E. J. Sie, H. Steinberg, D. R. Gardner, Y. S. Lee, P. Jarillo-Herrero, and N. Gedik, Measurement of intrinsic Dirac fermion cooling on the surface of a topological insulator Bi2Se3using time- and angle-resolved photoemission spectroscopy, *Physical Review Letters*, 109, 127401 (2012)

[6] Fribourg Center for Nanomaterials webpage, http://frimat.unifr.ch/frimat/en/page/487/

[7] J.-F. Adam, J.-P. Moy, J. Susini, Table-top water window transmission x-ray microscopy: Review of the key issues, and conceptual design of an instrument for biology, *Review of Scientific Instruments*, 76, 091301 (2005)

[8] E. Gibson, A. Paul, N. Wagner, R. Tobey, D. Gaudiosi, S. Backus, I. P. Christov, A. Aquila, E. M. Gullikson, D. T. Attwood, M. Murnane, H. C. Kapteyn, Coherent soft x-ray generation in the water window with quasi-phase matching, *Science*, 302, 5642, p. 95 (2003)

[9] S. Wurm, Lithography development and research challenges for the less than 22 nm

half-pitch, *Proceedings of SPIE*, 7470, 747002 (2009)

[10] G. Tallents, E. Wagenaars, G. Pert, Optical lithography: Lithography at EUV wavelengths, *Nature Photonics*, 4, pp. 809-811 (2010)

[11] M. Hentschel, R. Kienberger, C. Spielmann, G. Reider, N. Milosevic, T. Brabec, P. Corkum, U. Heinzmann, M. Drescher, F. Krausz, Attosecond metrology. *Nature*, 414 pp. 50913 (2001)

[12] E. Goulielmakis, M. Schultze, M. Hofstetter, V. S. Yakovlev, J. Gagnon, M. Uiberacker, A. L. Aquila, E. M. Gullikson, D. Attwood, R. Kienberger, F. Krausz, U. Kleineberg, Single-cycle nonlinear optics. *Science*, 320, pp. 161417 (2008)

[13] P.B. Corkum, F. Krausz, Attosecond Science. *Nature Physics*, 3, 381 (2007)

[14] J. Seres, E. Seres, A. J. Verhoef, G. Tempea, C. Streli, P. Wobrauschek, V. Yakovlev, A. Scrinzi, C. Spielmann, F. Krausz, Source of coherent kiloelectronvolt X-rays. *Nature* 433, 596 (2005)

[15] E. J. Takahashi, Y. Nabekawa, H. Mashiko, H. Hasegawa, A. Suda, K. Midorikawa, Generation of Strong Optical Field in Soft X-Ray Region by Using High-Order Harmonics, *IEEE Journal of Selected Topics in Quantum Electronics*, 10 (6), pp. 1315-1328 (2004)

[16] J. Kim, C. M. Kim, H. T. Kim, G. H. Lee, Y. S. Lee, J. Y. Park, D. J. Cho, C. H. Nam, Highly Efficient High-Harmonic Generation in an Orthogonally Polarized Two-Color Laser Field, *Physical Review Letters*, 94, 243901 (2005)

[17] J. Kim, G. H. Lee, S. B. Park, Y. S. Lee, T. K. Kim, C. H. Nam, Generation of submicrojoule high harmonics using a long gas jet in a two-color laser field, *Applied Physics Letters*, 92, 021125 (2008)

[18] M. Lewenstein, P. Balcou, M. Ivanov, A. LHuillier, P. Corkum, Theory of high-harmonic generation by low-frequency laser fields. *Physical Review A*, 49 (3), pp. 2117-2132 (1994)

[19] M. Ivanov, M. Spanner, O. Smirnova, Anatomy of strong field ionization, *Journal of Modern Optics*, 52 (3), pp. 165-184 (2005)

[20] G. L. Yudin, M. Y. Ivanov, Nonadiabatic tunnel ionization: Looking inside a laser cycle,

Physical Review A 64 (1), p. 013409 (2001)

[21] M. V. Ammosov, N. B. Delone, V. P. Krainov, Tunnel ionization of complex atoms and atomic ions in a varying electromagnetic field, *Soviet Physics JETP* 64 (6), pp. 1191-1194 (1986)

[22] A. Scrinzi, M. Geissler, and T. Brabec, Ionization above the Coulomb barrier, *Physical Review Letters*, 83 (4), pp. 706-709 (1999)

[23] X. M. Tong, Z. X. Zhao, C. D. Lin, Theory of molecular tunneling ionization, *Physical Review A*, 66 (3), p. 033402 (2002)

[24] J. Itatani, J. Levesque, D. Zeidler, Hiromichi Niikura, H. Pépin, J. C. Kieffer, P. B. Corkum, D. M. Villeneuve, Tomographic imaging of molecular orbitals, *Nature*, 432, 7019, pp. 867-871 (2004)

[25] S. Bhardwaj, S.-K. Son, K.-H. Hong, C.-J. Lai, F. X. Kärtner, R. Santra, Recombination Amplitude Calculations of Noble Gases, in Length and Acceleration Forms, beyond Strong Field Approximation, *under preparation*

[26] R. W. Boyd, Nonlinear Optics, *San Diego:Academic* (2003)

[27] A. E. Siegman, Lasers, *University Science Books* (1986)

[28] E. L. Falcão-Filho, V.-M. Gkortsas, A. Gordon, F. X. Kärtner, Analytic scaling analysis of high harmonic generation conversion efficiency, *Optics Express*, 17, pp. 11217-29 (2009)

[29] E. Constant, D. Garzella, P. Breger, E. Mével, C. Dorrer, C. Le Blanc, F. Salin, P. Agostini, Optimizing high harmonic generation in absorbing gases: model and experiment, *Physical Review Letters*, 82 (8), pp. 1668-1671 (1999)

[30] C. Durfee, A. Rundquist, S. Backus, C. Herne, M. Murnane, H. Kapteyn, Phase matching of high-order harmonics in hollow waveguides *Physical Review Letters*, 83 (11), pp. 218790 (1999)

[31] C.-J. Lai, F. X. Kärtner, The influence of plasma defocusing in high harmonic generation, *Optics Express*, 19 (23), pp. 22377-22387 (2011)

[32] A. L' Huillier, P. Balcou, S. Candel, K. J. Schafer, K. C. Kulander, Calculations of

high-order harmonic-generation processes in xenon at 1064 nm, *Physical Review A* 46, 2778 (1992)

[33] P. Balcou, P. Salières P, A. L' Huillier, M. Lewenstein, Generalized phase-matching conditions for high harmonics: the role of field-gradient forces, *Physical Review A*, 55 (4), pp. 3204-3210 (1997)

[34] P. Salières, P. Antoine, A. de Bohan, M. Lewenstein, Temporal and spectral tailoring of high-order harmonics, *Physical Review Letters*, 81, pp. 55447 (1998)

[35] M. B. Gaarde, J. L. Tate, K. J. Schafer, Macroscopic aspects of attosecond pulse generation, *Journal of Physics B: Atomic, Molecular and Optical Physics* 41, 132001 (2008)

[36] C. Altucci, T. Starczewski, E. Mevel, C.-G. Wahlstrom, B. Carre, A. L' Huillier, Influence of atomic density in high-order harmonic generation, *Journal of Optical Society of America B*, 13(1), pp. 148156 (1996)

[37] Q. Feng, J. V. Moloney, A. C. Newell, E. M. Wright, K. Cook, P. K. Kennedy, D. X. Hammer, B. A. Rockwell, C. R. Thompson, Theory and simulation on the threshold of water breakdown induced by focused ultrashort laser pulses, *IEEE Journal of Quantum Electronics*, 33 (2), pp. 127-137 (1997)

[38] A. Gordon, F. X. Kärtner, Quantitative Modeling of Single Atom High Harmonic Generation, *Physical Review Letters*, 95, 223901 (2005)

[39] D. I. Bondar, Instantaneous multiphoton ionization rate and initial distribution of electron momentum, *Physical Review A*, 78, 015405 (2008)

[40] M. Ivanov, M. Spanner, O. Smirnova, Anatomy of strong field ionization, *Journal of Modern Optics*, 52 (3), pp. 16584 (2005)

[41] G. Tempea, M. Geissler, T. Brabec, Phase sensitivity of high-order harmonic generation with few-cycle laser pulses, *Journal of the Optical Society of America B*, 16 (4), pp. 669-673 (1999)

[42] A. Gordon, F. X. Kärtner, N. Rohringer, R. Santra, Role of many-electron dynamics in high harmonic generation, *Physical Review Letters*, 96 (22), p. 223902 (2006)

[43] V.-M. Gkortsas, S. Bhardwaj, E. L. Falcão-Filho, K.-H. Hong, A. Gordon, and F. X.

Kärtner, Scaling of high harmonic generation conversion efficiency, *Journal of Physics B: Atomic, Molecular and Optical Physics*, 44 (4), p. 045601 (2011)

[44] E. L. Falcão-Filho, C.-J. Lai, K.-H. Hong, V.-M. Gkortsas, S-W. Huang, L.J. Chen, F. X. Kärtner, Scaling of high harmonic generation efficiencies with 400-nm and 800-nm driver pulses, *Applied Physics Letters*, 97, 61107 (2010)

[45] G. Sansone, C. Vozzi, S. Stagira, and M. Nisoli, Nonadiabatic quantum path analysis of high-order harmonic generation: Role of the carrier-envelope phase on short and long paths, *Physical Review A*, 70 (1), p. 013411 (2004)

[46] A.M. Dykhne, Adiabatic perturbation of discrete spectrum states, *Soviet Physics JETP*, 14 (4), pp. 941-943 (1962)

[47] A.V. Chaplik, *Soviet Physics JETP*, 18 (1046) (1963)

[48] J. Davis, P. Pechukas, Nonadiabatic transitions induced by a time dependent Hamiltonian in the semiclassical/adiabatic limit: The two state case, *The Journal of Chemical Physics*, 64, p. 3129 (1976)

[49] E. J. Takahashi, T. Kanai, K. L. Ishikawa, Y. Nabekawa, K. Midorikawa, Coherent water window X-ray by phase-matched high-order harmonic generation in neutral media, *Physical Review Letters*, 101, 253901 (2008)

[50] B. Shan, Z. Chang, Dramatic extension of the high-order harmonic cutoff by using a long-wavelength driving field, *Physical Review A*, 65 (1), p. 011804 (2001)

[51] A. Gordon, F. X. Kärtner, Scaling of keV HHG photon yield with drive wavelength, *Optics Express*, 13 (8), pp. 2941-2947 (2005)

[52] V. Yakovlev, M. Ivanov, F. Krausz, Enhanced phase-matching for generation of soft X-ray harmonics and attosecond pulses in atomic gases, *Optics Express*, 15 (23), pp. 15351-15364 (2007)

[53] E. Takahashi, Y. Nabekawa, K. Midorikawa, Low-divergence coherent soft x-ray source at 13 nm by high-order harmonics, *Applied Physics Letters*, 84 (1), p. 4, (2004)

[54] H. Xiong, H. Xu, Y. Fu, J. Yao, B. Zeng, W. Chu, Y. Cheng, Z. Xu, E. J. Takahashi, K. Midorikawa, X. Liu, J. Chen, Generation of a coherent x ray in the water window

region at 1 kHz repetition rate using a mid-infrared pump source, *Optics Letters*, 34 (11), pp. 1747-1749 (2009)

[55] T. Popmintchev, M.-C. Chen, A. Bahabada, M. Gerritya, P. Sidorenkob, O. Cohenb, I. P. Christovc, M. Murnanea, H. C. Kapteyn, Phase matching of high harmonic generation in the soft and hard X-ray regions of the spectrum, *Proceedings of the National Academy of Sciences*, 106 (26), pp. 10516 -10521 (2009)

[56] M.-C. Chen, P. Arpin, T. Popmintchev, M. Gerrity, B. Zhang, M. Seaberg, D. Popmintchev, M. Murnane, H. C. Kapteyn, Bright, Coherent, Ultrafast Soft X-Ray Harmonics Spanning the Water Window from a Tabletop Light Source, *Physical Review Letters*, 105 (17), p. 173901 (2010)

[57] W. F. Chan, G. Cooper, X. Guo, G. R. Burton, C. E. Brion, Absolute optical oscillator strengths for the electronic excitation of atoms at high resolution: Experimental methods and measurements for helium, *Physical Review A*, 44 (1), pp. 186-204 (1991)

[58] W. F. Chan, G. Cooper, X. Guo, G. R. Burton, C. E. Brion, Absolute optical oscillator strengths for the electronic excitation of atoms at high resolution. III. The photoabsorption of argon, krypton, and xenon, *Physical Review A*, 46 (1), pp. 149171 (1992)

[59] J. Faist, F. Capasso, D. L. Sivco, C. Sirtori, A. L. Hutchinson, A. Y. Cho, Quantum Cascade Laser, *Science*, 264 (5158) pp. 553556 (1994)

[60] R. Huber, F. Tauser, A. Brodschelm., M. Bichler, G. Abstreiter, A. Leitenstorfer, How many-particle interactions develop after ultrafast excitation of an electron-hole plasma, *Nature*, 414, pp. 286-289 (2001)

[61] R. Torre, P. Bartolini, R. Righini, Structural relaxation in supercooled water by time-resolved spectroscopy, *Nature*, 428, pp. 296-299 (2004)

[62] J. M. Dudley, G. Genty, S. Coen, Supercontinuum generation in photonic crystal fiber, *Reviews of Modern Physics*, 78, pp. 1135-1184 (2006)

[63] J.J. Macklin, J.D. Kmetec, C.L. Gordon, High-Order Harmonic-Generation Using Intense Femtosecond Pulses, *Physical Review Letters*, 70, pp. 766-769 (1993)

[64] R. Paiella, F. Capasso, C. Gmachl, H. Hwang, D.Sivco, A. Hutchinson and A. Y. Cho,

Monolithic active mode locking of quantum cascade lasers, *Applied Physics Letters*, 77, pp. 169-171 (2000)

[65] T. Udem, R. Holzwarth,T.W. Hansch, Optical frequency metrology, *Nature*, 416, pp. 233-237 (2002)

[66] H. Choi, T. B. Norris, T. Gresch, M. Giovannini, J. Faist, L. Diehl, F. Capasso, Femtosecond dynamics of resonant tunneling and superlattice relaxation in quantum cascade lasers, *Applied Physics Letters*, 92, pp. 122114 -122117 (2008)

[67] H. Choi, L. Diehl, Z.-K. Wu, M. Giovannini, J. Faist, F. Capasso, T.B. Norris, Gain recovery dynamics and photon-driven transport in quantum cascade lasers, *Physical Review Letters*, 100, 167401 (2008)

[68] C. Wang, L. Kuznetsova, L. Diehl, F. Kaertner, M. Belkin, H. Schneider, H. C. Liu, F. Capasso, Stable Mode-locked pulses from Mid-Infrared Quantum Cascade Lasers, Postdeadline paper, *Conference of Lasers and Electro optics*, San Jose, CA, USA (2008)

[69] C. Y. Wang, L. Kuznetsova, V.M. Gkortsas, L. Diehl, F. X. Kaertner, M. A. Belkin, A. Belyanin, X. Li, D. Ham, H. Schneider, P. Grant, C. Y. Song, S. Haffouz, Z. R. Wasilewski, H. C. Liu, F. Capasso, Mode-locked pulses from mid-infrared Quantum Cascade Lasers, *Optics Express*, 17 (15), pp. 12929-12943 (2009)

[70] A. Gordon, C. Wang, L. Diehl, F. Kaertner, A. Belyanin, D. Bour, S. Corzine, G. Hoefler, H. C. Liu, H. Schneider, T. Maier, M. Trocolli, J. Faist, F. Capasso, Multimode regimes in quantum cascade lasers: From coherent instabilities to spatial hole burning, *Physical Review A*, 77, 053804 (2008)

[71] R. Paiella, F. Capasso, C. Gmachl, D. Sivco, J. Baillargeon, A. Hutchinson, A. Y. Cho and H. C. Liu, Self-mode-locking of quantum cascade lasers with giant ultrafast optical nonlinearities, *Science*, 290, pp. 1739-1742 (2000)

[72] A. Soibel, F. Capasso, C. Gmachl, M. Peabody, A. M. Sergent, R. Paiella, D. Sivco, A. Y. Cho, H. C. Liu, Stability of Pulse Emission and Enhancement of Intracavity Second-Harmonic Generation in Self-Mode-Locked Quantum Cascade Lasers, *IEEE Journal of Quantum Electronics*, 40, pp. 197-204 (2004)

[73] A. Soibel, F. Capasso, C. Gmachl, M. Peabody, A. M. Sergent, R. Paiella, H. Hwang, D. Sivco, A. Y. Cho, H. C. Liu, C. Jirauschek, F.X. Kärtner, Active Mode locking of Broadband quantum Cascade Lasers, *IEEE Journal of Quantum Electronics*, 40, pp. 844-851 (2004)

[74] H. C. Liu, E. Dupont, Nonlinear quantum well infrared photodetector, *Journal of Nonlinear Optical Physics & Materials*, 11, pp. 433-443 (2002)

[75] T. Maier, H. Schneider, H. C. Liu, M. Walther, P. Koidl, Two-photon QWIPs for quadratic detection of weak mid-infrared laser pulses, *Infrared Physics & Technology*, 47, 182-187 (2005)

[76] C.Y. Wang, L. Diehl, A. Gordon, C. Jirauschek, F. X. Kaertner, A. Belyanin, D. Bour, S. Corzine, G. Hoefler, M. Troccoli, J. Faist, F. Capasso, Coherent instabilities in a semiconductor laser with fast gain recovery, *Physical Review A*, 75, 031802 (2007)

[77] C. Menyuk, M.A. Talukder, Self-induced transparency modelocking of quantum cascade lasers, *Physical Review Letters*, 102, 023903 (2009)

[78] J. Faist, D. Hofstetter, M. Beck, T. Aellen, M. Rochat, S. Blaser, Bound-to-continuum and tow-phonon resonance quantum cascade lasers for high duty cycle, high temperature operation, *IEEE Journal of Quantum Electronics* 38, 533-546 (2002)